Detection of individual spin transitions of a single proton confined in a cryogenic Penning trap

Dissertation
zur Erlangung des Grades
Doktor der Naturwissenschaften
am Fachbereich 08, Physik, Mathematik und Informatik
der Johannes–Gutenberg Universität in Mainz

Holger Kracke

geboren in Köln

Mainz, 11. Dezember 2012

Datum der mündlichen Prüfung: 27.02.2013

Zusammenfassung: Das in dieser Arbeit vorgestellte Experiment zur Messung des magnetischen Moments des Protons basiert auf der Messung des Verhältnisses von Zyklotronfrequenz und Larmorfrequenz eines einzelnen, in einer kryogenen Doppel-Penning Falle gespeicherten Protons. In dieser Arbeit konnten erstmalig zwei der drei Bewegungsfrequenzen des Protons gleichzeitig im thermischen Gleichgewicht mit entsprechenden hochsensitiven Nachweissystemen nicht-destruktiv detektiert werden, wodurch die Messzeit zur Bestimmung der Zyklotronfrequenz halbiert werden konnte. Ferner wurden im Rahmen dieser Arbeit erstmalig einzelne Spin-Übergänge eines einzelnen Protons detektiert, wodurch die Bestimmung der Larmorfrequenz ermöglicht wird. Mithilfe des kontinuierlichen Stern-Gerlach Effekts wird durch eine sogenannte magnetische Flasche das magnetische Moment an die axiale Bewegungsmode des Protons gekoppelt. Eine Änderung des Spinzustands verursacht folglich einen Frequenzsprung der axialen Bewegungsfrequenz, welche nicht-destruktiv gemessen werden kann. Erschwert wird die Detektion des Spinzustands dadurch, dass die axiale Frequenz nicht nur vom Spinmoment, sondern auch vom Bahnmoment abhängt. Die große experimentelle Herausforderung besteht also in der Verhinderung von Energieschwankungen in den radialen Bewegungsmoden, um die Detektierbarkeit von Spin-Übergängen zu gewährleisten. Durch systematische Studien zur Stabilität der axialen Frequenz sowie einer kompletten Überarbeitung des experimentellen Aufbaus, konnte dieses Ziel erreicht werden. Erstmalig kann der Spinzustand eines einzelnen Protons mit hoher Zuverlässigkeit bestimmt werden. Somit stellt diese Arbeit einen entscheidenden Schritt auf dem Weg zu einer hochpräzisen Messung des magnetischen Moments des Protons dar.

Summary: The presented experiment for the determination of the magnetic moment of the proton is based on the measurement of the ratio of cyclotron frequency and Larmor frequency of a single proton confined in a cryogenic double-Penning trap. In the course of this thesis, the simultaneous non-destructive measurement of two of the three eigenfrequencies of the proton in thermal equilibrium with corresponding detection systems was demonstrated, which reduces the measurement time of the cyclotron frequency by a factor of two. Furthermore, this thesis presents the first detection of individual spin transitions of a single proton, which allows for the determination of the Larmor frequency. The continuous Stern-Gerlach effect is utilized to couple the magnetic moment to the axial mode of the trapped proton by means of a magnetic bottle. Thus, a spin flip causes a jump of the axial frequency, which can be measured non-destructively with highly-sensitive detection systems. However, not only the spin momentum is coupled to the axial motion but also the angular momentum. Thus, the main experimental challenge is the elimination of energy fluctuations in the radial modes in order to maintain spin flip resolution. Due to systematic studies on the stability of the axial frequency and a complete revision of the experimental setup, this goal was achieved. The spin state of the proton can be determined with very high fidelity for the very first time. Thus, this thesis represents an important step towards a high-precision determination of the magnetic moment of the proton.

Für meine Eltern

Contents

List of Figures

List of Tables

Chapter 1

Introduction

The Standard Model of elementary particle physics describes many aspects observed in nature, and two of the four known interactions, electromagnetism and weak interaction, were unified in its framework [1]. However, not all experimental observations in nature can be explained by the Standard Model, such as dark matter, gravitation, neutrino oscillations and the matter-antimatter asymmetry. Moreover, some aspects of the theory itself lack of a deeper understanding, such as for example the 18 free parameters for particle masses, CKM mixing angles and coupling constants. Thus, physicists all around the world conduct various experiments to search for new physics beyond the Standard Model which could settle these questions and perhaps guide the way towards a grand unified theory [2].
At high energy, the search for new physics is carried out at particle colliders to produce and detect exotic particles or to observe unexpected processes. Complementary, low energy precision studies of quantities that can be described by the Standard Model can give a hint to new phyiscs, which would manifest as difference between the predicted and experimental values.
The potential of Penning traps as a tool for a high-precision determination of fundamental properties of particles was demonstrated by Dehmelt and coworkers in 1987 with the measurement of the magnetic moment of the electron with a relative uncertainty of 4 ppt [3]. The impressive achieved precision mainly arose from two aspects:

1. Single particle storage at cryogenic temperatures, which enables infinite storage times and eliminates possible corrections due to thermal line-broadening and interaction with other particles and the environment.

2. Outstanding experimental and theoretical control of the oscillatory motion of the single electron, which in turn can be measured non-destructively to determine the magnetic moment.

The single trapped electron was called *geonium atom*, as an anologon to that bound to a nucleus [4]. The realization of the *geonium atom* was honored with the 1989 Nobel Prize. It was the starting point for a long success story of high-precision experiments performed in Penning traps [5]. Any charged particle with sufficient lifetime can be investigated which

indicates the variety of possible experiments to determine for example masses, decay energies and magnetic moments. In particular, high-precision measurements of magnetic moments proved as sensitive probe for fundamental theories. A new measurement of g-2 yields the most precise test of quantum electrodynamics (QED) [6, 7]. Comparison of the measured electron g-factor with QED calculations up to the tenth order led to the hitherto most precise determination of the fine structure constant [8]. The predictions of QED in extreme situations can be tested by a measurement of the magnetic moment of the electron in the strong binding field of hydrogenlike ions [9, 10, 11, 12].
Furthermore, high-precision experiments in Penning traps can be used to obtain tight bounds for potential CPT-violation [13]. The CPT-transformation is formed by three discrete symmetries: charge conjugation (C), parity transformation (P) and time reversal (T). A violation of CPT-symmetry would imply a breaking of Lorentz symmetry [14]. The Standard Model is a locally Lorentz-invariant quantum field theory. Thus, an observation of CPT-violation would guide the development of new physics beyond the Standard Model. The asymmetry between matter and antimatter in the universe, also known as baryogenesis, could be explained by CPT-violation [15]. CPT-symmetry implies that certain properties as mass and the magnetic moment of a particle and its antiparticle must have identical values. Low energy Penning trap experiments are well-suited to test these quantities at highest precision. The comparison of the magnetic moments of electron and positron in a Penning trap is considered the most precise test of the matter-antimatter symmetry for leptons [3]. However, stringent CPT tests have to be carried out with different systems since it is unknown which physical system is the most sensitive for CPT-violating effects.
Therefore another approach to test CPT-symmetry is the measurement of the magnetic moment of the proton and the antiproton, which in combination would yield a stringent test of CPT-symmetry in the baryon sector [13].
A series of experiments were conducted to measure the magnetic moment of the proton $\mu_p = (g_p/2)\mu_N = (g_p/2)(e\hbar)/(2m_p)$, where g_p is the Landé g-factor of the proton, μ_N is the nuclear magneton and e/m_p the charge-to-mass-ratio of the proton. Starting in 1933, Stern and Gerlach observed the deflection of a molecular hydrogen beam in a homogeneous magnetic field, yielding a value for the magnetic moment of the proton of $\mu_p = 2.5(3)\mu_N$ [16, 17]. The deviation of more than a factor of two compared to the value, which is predicted by Dirac-theory [18] was the first indication of the substructure of the proton which we nowadays identify as a composition of quarks and gluons. This remarkable observation was awarded with the 1943 Nobel Prize. Later experiments determined the proton magnetic moment using molecular beam methods [19], nuclear magnetic resonance in water [20] and the omegatron method [21, 22], which continuously improved the relative precision to 14 ppm.
The currently most precise value for the g-factor of the proton is determined from a measurement of the splitting of the hyperfine sublevels in atomic hydrogen [23], where the magnetic moment ratio of the proton and the electron $\mu_p(H)/\mu_e(H)$ was measured. The

free proton g-factor is obtained using

$$g_p = g_e \frac{\mu_p(H)}{\mu_e(H)} \frac{g_e(H)}{g_e} \frac{g_p}{g_p(H)} \frac{m_p}{m_e} \quad . \tag{1.1}$$

The two correction terms $g_e(H)/g_e$ and $g_p(H)/g_p$ give the ratio of bound to free g-factors, which have been calculated in [24] with a relative uncertainty of less than $< 1\,\text{ppb}$. The relative uncertainties of the experimental values for the electron g-factor g_e and the proton-to-electron mass ratio m_p/m_e are less than 0.001 ppb [6] and 1 ppb [25], respectively. The overall uncertainty is dominated by the precision of the ratio $\mu_p(H)/\mu_e(H)$, which was determined to 10 ppb, yielding a value for the proton g-factor of $g_p = 5.585694713(46)$.

The experiment which is presented in this thesis, aims for the determination of the magnetic moment of a single proton stored in a cryogenic Penning trap [26, 27, 28]. Thus, no binding-correction terms and particle interactions have to be considered. In the course of this thesis it will be shown, that an improvement of the accuracy of the proton g-factor by at least one order of magnitude compared to the most precise value obtained in [23, 24] is feasible. Capture [29] and storage of a single antiproton in a Penning trap for months [30] has already been demonstrated. Moreover, all techniques and methods which are developed for the determination of the proton g-factor are directly applicable for the antiproton, which proves the feasibility of a stringent CPT-test with baryons. A competing experiment at the Harvard-University also aims for the determination of the g-factor of the (anti)proton [31, 32].
The determination of the g-factor in a Penning trap can be realized by the measurement of two frequencies, the cyclotron frequency and the Larmor frequency. The first frequency results from the circular motion of a charged particle in a magnetic field. The possibility to determine the cyclotron frequency of a single trapped proton with a relative precision of the order of 1 ppb is demonstrated in this thesis. The measurement of the Larmor frequency is carried out by probing spin transitions as a function of the frequency of an external driving field. The so-called Continuous Stern-Gerlach effect [33] is utilized to non-destructively detect spin transitions as a jump of the axial eigenfrequency of the trapped proton. This technique was already succesfully applied in case of the experiments to determine the magnetic moment of the electron. However, the size of this frequency jump is proportional to the ratio of magnetic moment over mass of the trapped particle. Thus, the signature of spin transitions is by about six orders of magnitude smaller compared to the free electron, which illustrates the experimental challenge. This thesis presents the first detection of individual single proton spin transitions which is an important step towards a high-precision determination of the g-factor of the proton and the antiproton.
The most accurate value for the g-factor of the antiproton was determined from spectroscopy experiments of exotic antiprotonic atoms in [34, 35]. However, the relative precision of these measurements is of the order of 10^{-3}, only. Thus, a millionfold improved value for the antiproton g-factor is feasible. Very recently, a new collaboration named BASE (Baryon Antibaryon Symmetry Experiment) has started to set up an experiment

at CERN to determine the magnetic moment of the antiproton [36]. Thus, a stringent test of the CPT-symmetry in the baryon sector is in reach.

This thesis is organized as follows:

- Chapter 2 describes the principles of charged particle storage in a Penning trap.
- Chapter 3 describes the continuous Stern-Gerlach effect, the motion of a proton in a magnetic bottle field and the double-trap technique to determine the g-factor.
- Chapter 4 describes the non-destructive detection of the eigenmotions of the trapped proton.
- Chapter 5 describes the experimental setup.
- Chapter 6 describes the production of a single proton.
- Chapter 7 reports on the high-precision determination of the free cyclotron frequency of a single proton in the precision trap. The realization of the first detection of a single proton cyclotron noise-dip is discussed.
- Chapter 8 reports on the first detection of individual spin transitions of a single proton. This was realized by systematic studies on the stability of the axial eigenfrequency of the proton in the analysis trap.
- Chapter 9 summarizes the experimental status and gives an outlook on future perspectives.

Chapter 2

Penning trap

A Penning trap confines charged particles by a superposition of static magnetic and electric fields [37, 38]. A homogeneous magnetic field restricts the motion of the ion in the radial plane. The strength of the magnetic field B_0 defines the free cyclotron frequency

$$\omega_c = \frac{q}{m} B_0 \quad , \tag{2.1}$$

where q/m is the charge-to-mass ratio of the ion, which is in case of the proton e/m_p. The confinement along the axis $\vec{e}_z$ of the magnetic field is achieved by a quadrupole electrostatic potential. A possible realization by a set of hyperbolic electrodes is shown in Fig. 2.1. A

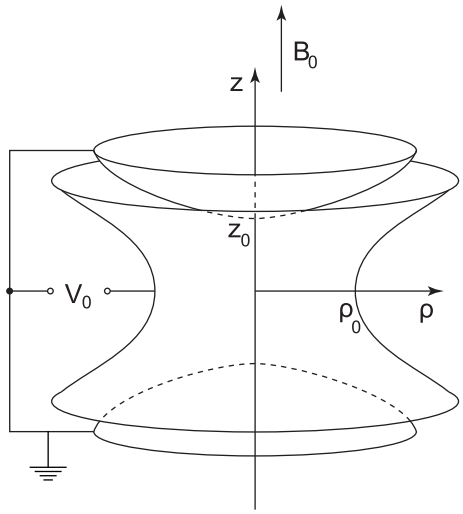

Figure 2.1: A hyperbolical Penning trap which consists of a ring electrode with radius ρ_0 and two endcaps at distance $2z_0$. The electrostatic quadrupole potential is realized by applying a voltage V_0 to the ring electrode. The magnetic field B_0 in z-direction confines the particle in the radial plane. The electric field confines the particle in the axial direction.

voltage V_0 is applied to the ring electrode and the endcaps are kept on ground potential. Infinitely extended electrodes of hyperbolic shape produce a purely quadrupolar potential

$$\Phi(z, \rho) = V_0 \frac{z^2 - \rho^2/2}{2d^2} \text{ with } d^2 = \frac{1}{2}\left(z_0^2 + \frac{\rho_0^2}{2}\right) \quad . \tag{2.2}$$

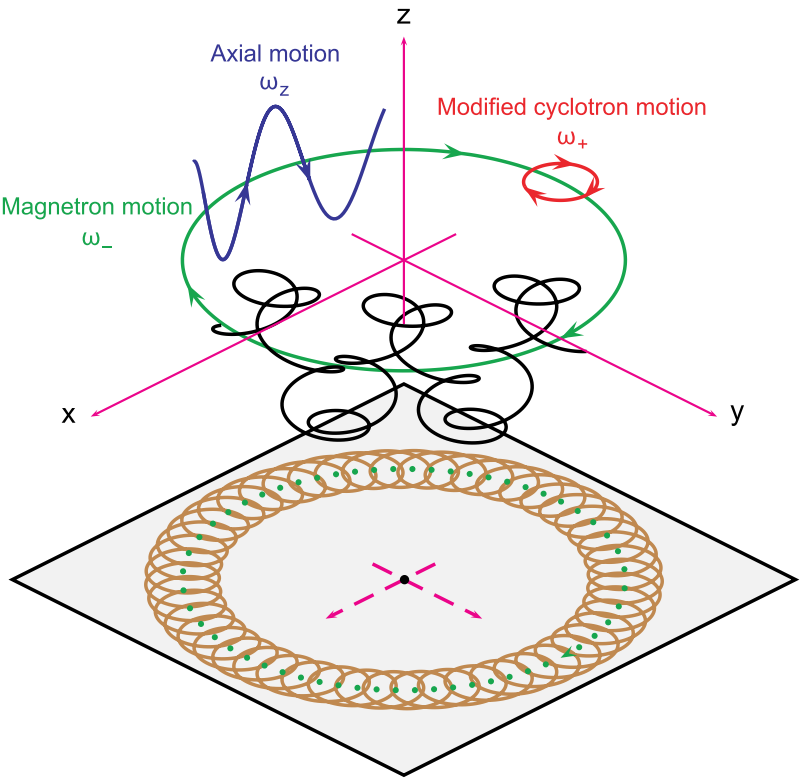

Figure 2.2: The motion of a charged particle inside a Penning trap is a superposition of three eigenmotions [40]: The magnetron motion around the trap center in the radial plane at frequency ω_-, the circular motion at the modified cyclotron frequency ω_+ and the axial motion along the magnetic field lines at frequency ω_z.

Here z_0 and ρ_0 are the distances from the center of the trap to the endcaps and the ring electrode, respectively, which define the characteristic trap parameter d.

2.1 Particle motion I: The three eigenmotions

The motion of the ion is described by three independent eigenmodes as shown in Fig. 2.2: The axial oscillation along the magnetic field lines and the two radial modes called magnetron motion and modified cyclotron motion. The frequencies of these modes can be obtained by solving the equations of motion [39]:

$$\omega_z = \sqrt{\frac{qV_0}{md^2}} \quad , \tag{2.3}$$

$$\omega_- = \frac{\omega_c}{2} - \sqrt{\left(\frac{\omega_c}{2}\right)^2 - \frac{\omega_z^2}{2}} \quad , \tag{2.4}$$

$$\omega_+ = \frac{\omega_c}{2} + \sqrt{\left(\frac{\omega_c}{2}\right)^2 - \frac{\omega_z^2}{2}} \quad . \tag{2.5}$$

The axial frequency ω_z is independent of the magnetic field. The electric field shifts the free cyclotron frequency to ω_+. The magnetron frequency ω_- is defined by the balance of

the Lorentz force and the attractive force of the electric field in radial direction. Stable storage is only realized if the radicand in Eq. (2.4) and Eq. (2.5) is positive.
For our experiment[1]*, a magnetic field of* $B_0 = 1.899\ T$ *and a trapping voltage of* $V_0 = 3.1\ V$ *is used to trap a single proton. With* $d = 5.7\ mm$ *the three eigenfrequencies are given by*

$$\omega_z = 2\pi \cdot 674\,\text{kHz},\ \omega_- = 2\pi \cdot 8.4\,\text{kHz} \text{ and } \omega_+ = 2\pi \cdot 28.97\,\text{MHz}\ .$$

The axial frequency is related to the radial frequencies by

$$\omega_+\omega_- = \frac{\omega_z^2}{2} \quad . \tag{2.6}$$

The frequency of interest, the free cyclotron frequency, is related to the eigenfrequencies by the following equations:

$$\omega_c = \omega_+ + \omega_- \quad , \tag{2.7}$$
$$\omega_c^2 = \omega_+^2 + \omega_z^2 + \omega_-^2 \quad . \tag{2.8}$$

The later equation, the so-called Invariance Theorem [41], does not only hold for ideal traps as described above but also in case of a misalignment between the magnetic field and the symmetry axis of the electrostatic trapping potential and in case of an ellipticity of the trapping potential. This allows to determine the free cyclotron frequency to high accuracy even in the presence of alignment errors or an ellipticity. Thus, Eq. (2.8) is used to determine the free cyclotron frequency. Due to the hierarchy of the eigenfrequencies

$$\omega_+ \gg \omega_z \gg \omega_- \quad , \tag{2.9}$$

the resulting precision of the free cyclotron frequency is mainly limited by the uncertainty of the measurement of the modified cyclotron frequency. Thus, for the determination of the free cyclotron frequency, the experimental focus is set on a fast and accurate measurement of the modified cyclotron frequency.
In the magnetic field the spin may orientate parallel or antiparallel to the magnetic field lines. The two spin states called *up* and *down* are separated by the energy $\hbar\omega_L$, where the spin precession frequency, also referred to as Larmor frequency, ω_L is given by

$$\omega_L = g\frac{q}{2m}B_0 \quad . \tag{2.10}$$

The total energy of the system can be written as a sum of the spin precession with quantum number $m_L = \left(-\frac{1}{2}, +\frac{1}{2}\right)$ and the three independent harmonic oscillators [42]

$$\begin{aligned} E &= E_L + E_+ + E_z + E_- \\ &= \hbar m_L\omega_L + \hbar\omega_+\left(n_+ + \frac{1}{2}\right) + \hbar\omega_z\left(n_z + \frac{1}{2}\right) - \hbar\omega_-\left(n_- + \frac{1}{2}\right) \quad , \end{aligned} \tag{2.11}$$

[1] Numerical examples of physical quantities for typical parameters in our experiment are highlighted in *italics*.

where n_i are the quantum numbers of the eigenmotions. The negative sign of the magnetron motion arises from the metastable character of this oscillation. The energy in the magnetron mode is given by

$$E_- = \frac{1}{2}m\left(\omega_-^2 - \frac{\omega_z^2}{2}\right)\rho_-^2 \approx -\frac{1}{4}m\omega_z^2\rho_-^2 \quad , \tag{2.12}$$

where in the last step the kinetic term $\frac{1}{2}m\omega_-^2\rho_-^2$ has been neglected since $\omega_-^2/\omega_z^2 \ll 1$. Thus, reducing the magnetron energy E_- actually increases the magnetron radius ρ_- since it is primarily potential energy. However, the magnetron mode is effectively stable since in case of the proton the radiation rate is negligible [39].
The energy of the axial motion and the modified cyclotron motion are given by

$$E_z = \frac{1}{2}m\omega_z^2 z^2 \quad , \tag{2.13}$$

$$E_+ = \frac{1}{2}m\omega_+^2\rho_+^2 \quad . \tag{2.14}$$

2.2 Particle motion II: Energy dependence

The trapping potentials in an actual Penning trap experiment are not uniform and homogeneous [39]. The purely quadratic electrostatic potential of Eq. (2.2) cannot be achieved in a real experiment due to imperfections in machining and alignment of the electrodes and patch effects which disturb the potentials on the electrodes. In addition, the homogeneity of the magnetic field is limited due to the finite length of the generating coils and due to the presence of the apparatus in the bore of the solenoid. The interesting question is how these disturbances affect the mode frequencies and whether these shifts can be compensated.
In case of the electrostatic potential this can be investigated by a Taylor expansion around the center of the trap. For a small magnetron radius $\rho_- \ll \rho_0$, this can be reduced to an expansion in the axial direction

$$\Phi(z,\rho) \approx \Phi(z) = \sum_{k=0}^{\infty} C_k z^k \text{ with } C_k = \frac{1}{k!}\frac{\partial^k \Phi}{\partial z^k}\bigg|_{(0)} = c_k V_0 \quad . \tag{2.15}$$

Due to the mirror symmetry of the trap all odd terms can be neglected. The lowest even order $k = 2$ describes the harmonic oscillation at frequency

$$\omega_z = \sqrt{\frac{2qV_0c_2}{m}} \quad . \tag{2.16}$$

The particle amplitudes are in the range of several μm which is orders of magnitude smaller than the trap size. Thus, only orders up to $k = 6$ have to be taken into account. For the axial mode these higher order terms change the equation of motion to

$$\ddot{z} = -\frac{q}{m}\nabla\sum_{k=0}^{6} V_0 c_k z^k = -\frac{2q}{m}V_0\left(c_2 z + 2c_4 z^3 + 3c_6 z^5\right) \quad . \tag{2.17}$$

Neglecting the quintic term z^5 one obtains an equation of a cubic Duffing Oscillator of the form

$$\ddot{z} = \omega_0^2 z + \beta z^3 \quad . \tag{2.18}$$

The effect of the so-called Duffing term βz^3 on the oscillation is discussed in many course books [43]. The solution of Eq. 2.18 can be expressed as

$$\omega_1^2 = \omega_0^2 + f(\beta) z^2 \quad , \tag{2.19}$$

where the parameter $f(\beta)$ is given by the strength of the anharmonicities. Thus, the frequency is shifted by a part which depends on the motional amplitude, which causes line broadening and systematic shifts - a highly undesired feature. Solving Eq. (2.17), the axial frequency shift $\Delta\omega_z$ can be expressed as a function of the axial energy E_z as

$$\Delta\omega_z = \frac{3}{4}\omega_z \left(\frac{c_4}{c_2^2} + \frac{5}{6}\frac{c_6}{c_2^3}\left(\frac{E_z}{qV_0}\right)\right)\frac{E_z}{qV_0} \quad . \tag{2.20}$$

For a proton at cryogenic axial temperatures $T_z = 4.2\,K$ ($E_z = 0.36\,meV$) and $c_4/c_2^2 = 10^{-4}$ the relative shift of the axial frequency amounts to $\Delta\omega_z/\omega_z = 9 \cdot 10^{-9}$. The contribution of the higher order term $c_6/c_2^3 = 10^{-4}$ causes a shift of $\Delta\omega_z/\omega_z = 9 \cdot 10^{-13}$ only. However, considering an excited ion with an energy of $E_z = 100\,meV$, the same anharmonicities cause shifts of the order of $\Delta\omega_z/\omega_z(c_4) = 2 \cdot 10^{-6}$ and $\Delta\omega_z/\omega_z(c_6) = 6 \cdot 10^{-8}$, respectively. Thus for higher particle energies, higher order corrections become more significant.

A systematic shift of the axial frequency due to a certain energy E_z could be compensated. However, this requires precise knowledge of E_z and that E_z is stable during the measurement of the frequency.

But as we will see in Chapter 4 the axial mode energy is thermally distributed. This means that for non-vanishing c_4 and c_6 the axial frequency will be smeared out which makes a high-precision measurement very difficult.

A non-harmonic potential ($c_4 \neq 0$) does not only affect the axial mode but results in a coupling of all eigenmodes and thus in a dependence on the mode energies E_i [42]. The frequency shift for the axial frequency is given by

$$\frac{\Delta\omega_z}{\omega_z} = \frac{3}{qV_0}\frac{c_4}{c_2^2}\left(-\frac{1}{2}\left(\frac{\omega_z}{\omega_+}\right)^2 E_+ + \frac{1}{4}E_z + |E_-| \right) \quad , \tag{2.21}$$

the modified cyclotron frequency is shifted by

$$\frac{\Delta\omega_+}{\omega_+} = \frac{3}{qV_0}\frac{c_4}{c_2^2}\left(\frac{1}{4}\left(\frac{\omega_z}{\omega_+}\right)^4 E_+ - \frac{1}{2}\left(\frac{\omega_z}{\omega_+}\right)^2 E_z - \left(\frac{\omega_z}{\omega_+}\right)^2 |E_-| \right) \tag{2.22}$$

and for the magnetron frequency one obtains

$$\frac{\Delta\omega_-}{\omega_-} = \frac{3}{qV_0}\frac{c_4}{c_2^2}\left(-\left(\frac{\omega_z}{\omega_+}\right)^2 E_+ + E_z + |E_-| \right) \quad . \tag{2.23}$$

The effect of an inhomogeneous magnetic field on the eigenfrequencies is described in chapter 3.

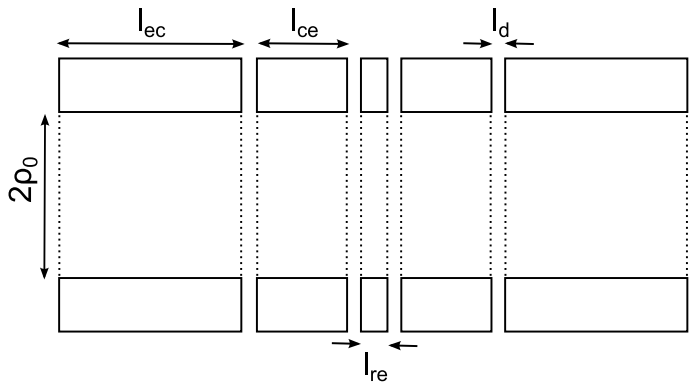

Figure 2.3: A 5-electrode cylindrical Penning trap with inner radius ρ_0 providing open access on the symmetry axis is shown. The voltage V_c applied to the correction electrodes with length l_{ce} is used to achieve a quadrupole potential in the center of the trap. The length of the ring electrode and the endcaps are denoted by l_{re} and l_{ec}, respectively. The electrodes are spaced by the length l_d.

2.3 Cylindrical Penning trap design

In our experiment cylindrical Penning traps [44] are utilized since they have several advantages:

1. Cylindrical electrodes are easier to machine than hyperbolical shaped electrodes.
2. The trap can be easily extended by additional electrodes or even by extra traps.
3. Due to the open access on the symmetry axis the ions can easily be exchanged between these traps.
4. The potential is analytically calculable which simplifies the design of the trap.

The electrostatic design of a Penning trap focuses on two aspects, the *orthogonality* and the *compensation*.
The cylindrical Penning trap shown in Fig. 2.3 has additional correction electrodes in-between the ring electrode and the endcaps. These correction electrodes are biased to tune out some of the anharmonicities (c_4, c_6). The relation between the voltages of correction V_c and ring electrode V_0 is called tuning-ratio

$$T_R = \frac{V_c}{V_0} \quad . \tag{2.24}$$

The coefficients c_4 and c_6 are minimized for the tuning-ratios $T_R^{c_4}$ and $T_R^{c_6}$, respectively. The difference between the two tuning-ratios $\Delta T_R = T_R^{c_4} - T_R^{c_6}$ should be small in order to eliminate higher order contributions simultaneously. The feature to achieve $c_4 = c_6 = 0$ for a specific tuning-ratio $\Delta T_R = 0$ is called *compensation*.
A modification of the tuning-ratio will influence the potential and thus change the axial frequency by

$$d_2 = \partial\omega_z / \partial T_R \quad . \tag{2.25}$$

	AT	PT
Inner radius of ring electrode ρ_0 (mm)	1.8	3.5
Length of ring electrode l_{re} (mm)	0.39	0.92
Length of correction electrode l_{ce} (mm)	1.36	2.85
Length of endcap l_{ec} (mm)	8.65	6.91
Distance between electrodes l_d (mm)	0.14	0.14
Quadrupolar contribution c_2 $(\mathrm{m})^{-2}$	$115 \cdot 10^3$	$30.5 \cdot 10^3$
Orthogonality d_2 (Hz/mUnit)	0.065	3.3
compensation ΔT_R (mUnit)	-0.037	-24.3
$d_4 = \partial c_4/\partial T_R$ (mm^{-4}/mUnit)	$48 \cdot 10^{-3}$	$3.4 \cdot 10^{-3}$
$d_6 = \partial c_6/\partial T_R$ (mm^{-6}/mUnit)	$-14 \cdot 10^{-3}$	$0.7 \cdot 10^{-3}$
Magnetic field B_0 (T)	1.167	1.9
Ring voltage V_0 (V)	-1.02	-4.32
Axial frequency ν_z (kHz)	742.1	785.1
Magnetron frequency ν_- (kHz)	16.3	10.6
Modified cyclotron frequency ν_+ (MHz)	17.78	28.97

Table 2.1: The geometric and potential parameters of the analysis trap (AT) and the precision trap (PT) and the motional frequencies of a trapped proton.

This behavior is no limit for the achievable experimental accuracy. However, the axial frequency can only be measured in a narrow range as will be explained in chapter 4. Thus, optimizing the tuning-ratio requires tedious additional adjustment of the ring voltage. This can be overcome by a vanishing d_2, which is called *orthogonality*.
The design of an *orthogonal* and *compensated* trap can be achieved by an appropriate geometry of the trap. For a given inner radius of the electrodes, the length of the ring and the correction electrodes as well as the tuning-ratio are the three required degrees of freedom. In [45] an expression for the coefficients of Eq. (2.15) in terms of the trap dimensions is given. This allows for the design of an *orthogonal* and *compensated* trap.
Our experiment utilizes two Penning traps, the so-called precision trap (PT) and the so-called analysis trap (AT), which will be motivated in chapter 3. However, the parameters for both Penning traps are already summarized in table 2.1, giving an overview of the dimensions and the electrostatic coefficients. The parameters $d_4 = \partial c_4/\partial T_R$ and $d_6 = \partial c_6/\partial T_R$ are extracted from a potential-calculation with COMSOL [46]. The details of the design of the analysis trap can be found in [46] and [47].

Chapter 3

The magnetic bottle

The determination of the g-factor can be reduced to the measurement of the free cyclotron frequency ω_c and the Larmor frequency ω_L

$$g = 2\frac{\omega_L}{\omega_c} \quad . \tag{3.1}$$

The free cyclotron frequency is deduced from the three eigenfrequencies of the trapped proton by application of the Invariance Theorem (Eq. (2.8)). The non-destructive determination of the eigenfrequencies is based on the detection of the movement of the proton in the trap (see chapter 4). Since the precession of the spin is not a movement of a charge, this detection scheme is not applicable for the determination of the Larmor frequency. However, the energy splitting ΔE_L between the two spin states in a magnetic field

$$\Delta E_L = \vec{\mu} \cdot \vec{B} = g\frac{e\hbar}{2m_p}B_0 = \hbar\omega_L \tag{3.2}$$

can be utilized to probe spin transitions. The spin flip probability is scanned as a function of the frequency of an external driving field. From the resulting Larmor resonance curve ω_L can be extracted. A fundamental requirement for this measurement scheme is the ability to observe spin transitions. This is accomplished by a coupling between the magnetic moment of the proton in the trap and its axial oscillation frequency in the presence of an inhomogeneous magnetic field, the so-called continuous Stern-Gerlach effect [33]. A ring electrode made of ferromagnetic material produces a quadratic magnetic field component B_2 symmetric around the z-axis in addition to the homogeneous part B_0, which results in a magnetic field of

$$\vec{B} = B_0\vec{e}_z + B_2\left[\left(z^2 - \frac{\rho^2}{2}\right)\vec{e}_z - z\vec{\rho}\right] \quad . \tag{3.3}$$

Due to the interaction of the μ_z-component of the magnetic moment with this so-called magnetic bottle, the effective axial potential is given by the sum of the electrostatic potential Φ_z^{el} and the magnetic potential Φ_z^{mag}

$$\Phi_z = \Phi_z^{\mathrm{el}} + \Phi_z^{\mathrm{mag}} = c_2V_0z^2 + \mu_zB_2\left(z^2 - \rho^2/2\right) \quad . \tag{3.4}$$

This modifies the axial equation of motion

$$\ddot{z} = -\left(\frac{2qc_2V_0}{m_p} + \frac{2\mu_z B_2}{m_p}\right) z \quad , \tag{3.5}$$

which alters the axial frequency

$$\omega_z^2 = \omega_{z,0}^2 \left(1 + \frac{2\mu_z B_2}{m_p \omega_{z,0}^2}\right) \quad , \tag{3.6}$$

with $\omega_{z,0}$ being the unperturbed axial frequency in a homogeneous magnetic field. Since the second term in the brackets is typically small compared to 1 and consequently $\omega_z \approx \omega_{z,0}$ the axial frequency shift can be expressed as

$$\Delta\omega_z = \frac{2\mu_z B_2}{m_p \omega_z} \quad . \tag{3.7}$$

A spin transition of $\Delta m_L = \pm 1$ leads to a frequency shift of

$$\Delta\omega_{z,\mathrm{SF}} = \mp g \frac{\mu_N B_2}{m_p \omega_z} \quad . \tag{3.8}$$

By measuring ω_z before and after irradiation of an external driving field, the success of the attempt to induce a spin transition can be detected. Accordingly, the spin flip probability P_{SF} for a given driving frequency ω_{RF} can be obtained in a series of spin flip attempts. Finally, by scanning the external driving frequency ω_{RF} the Larmor resonance curve $P_{\mathrm{SF}}(\omega_{\mathrm{RF}})$ is obtained from which the Larmor frequency can be deduced.
The realization of the magnetic bottle is discussed in the following section 3.1. As in case of the electrostatic anharmonicities discussed in the previous chapter, a quadratic component of the magnetic field shifts the eigenmotions depending on their motional amplitudes. This causes a broadening (see section 3.2) and a shift (see section 3.3) of the resonance curves, which precludes a high-precision measurement of the g-factor in the magnetic bottle. This can be overcome by the introduction of a double-trap setup (see section 3.4), which means that the trap with the magnetic inhomogeneity is only used for the spin state analysis.
However, inside a magnetic bottle, the axial frequency does not only depend on the spin magnetic momentum but also on the orbital magnetic momentum. Accordingly, the axial frequency fluctuates due to energy changes in the radial modes. Two detection schemes for ω_L and ω_c for a fluctuating axial frequency are discussed in section 3.5.

3.1 Magnetic bottle design - the analysis trap

A Penning trap with a very strong superimposed magnetic bottle of $B_2 = 300\,\mathrm{mT/mm^2}$ (see Fig. 3.1) had been designed in the Ph.D.-thesis of Cricia de Carvalho Rodegheri [46]. A spin flip in this magnetic bottle causes an axial frequency jump of $\Delta\omega_{\mathrm{z,SF}} = 2\pi \cdot 171\,\mathrm{mHz}$ at an absolute axial frequency of $\omega_z = 2\pi \cdot 742\,\mathrm{kHz}$.
In principle, the magnetic bottle can be increased by the reduction of the inner diameter of the trap. However, a smaller trap diameter has several experimental drawbacks. First,

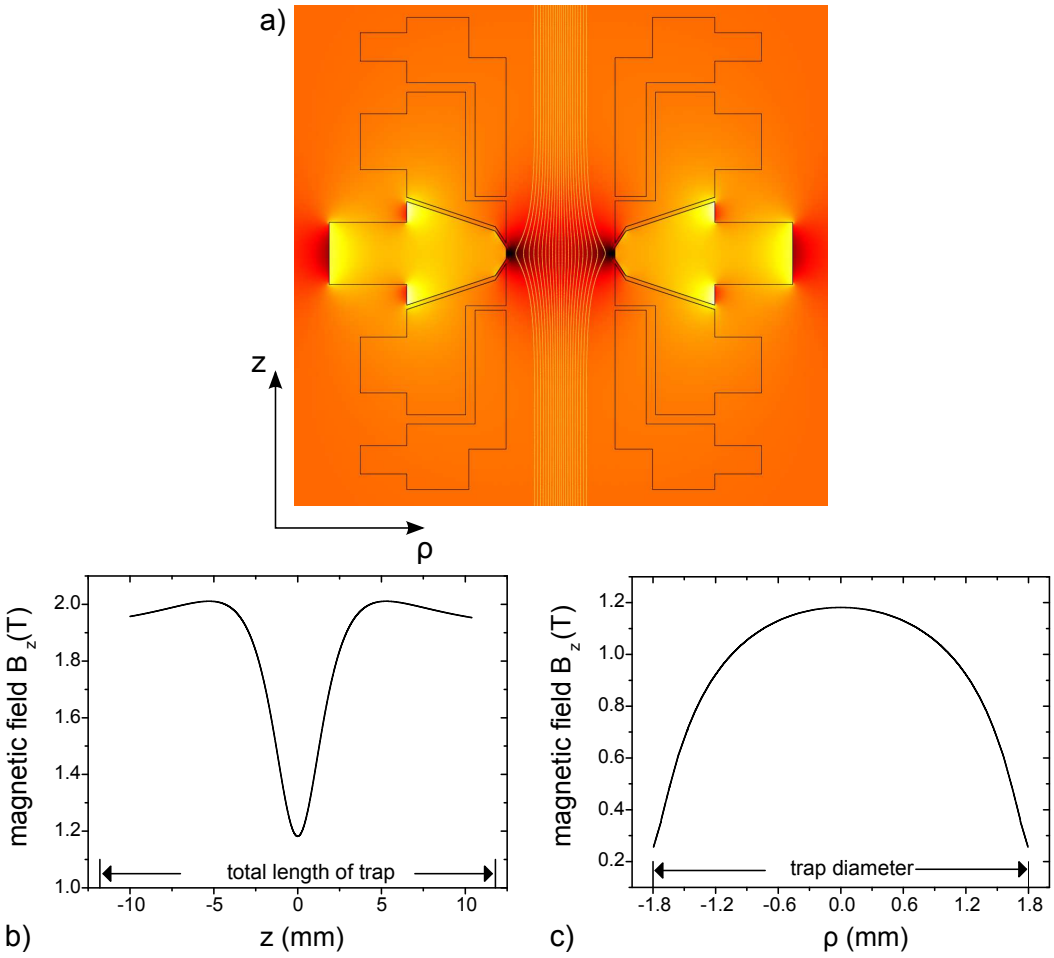

Figure 3.1: In a) a sketch of the analysis trap with the ferromagnetic ring electrode is shown. The magnetic field lines are calculated by an FEM-calculation done with *COMSOL*. The resulting z-component of the magnetic field B_z as a function of the cylindrical coordinates z and ρ is shown b) and c), respectively. The center of the analysis trap is given by $z = \rho = 0$. The magnetic field increases as a function of z and decreases as a function of ρ.

the electrostatic potential is much more sensitive on patch potentials on the electrodes which complicates the trap optimization (see chapter 8). Second, great care has to be taken when manufacturing and assembling the trap to avoid impurities on the surfaces of the electrodes (see chapter 5). In order to obtain the maximum possible bottle B_2 for a given inner radius the ring electrode is made of cobalt-iron (Co/Fe), which saturates in the strong magnetic field. On the other hand, a special geometry was chosen in order to increase the magnetic inhomogeneity for a given inner trap radius. Thus, the radius of the trap had to be decreased to $\rho_0 = 1.8\,\mathrm{mm}$, only. The parameters of the so-called analysis trap are summarized in Tab. 2.1 in the previous chapter.

3.2 Magnetic bottle lineshape

The determination of the Larmor frequency is based on the measurement of the spin transition rate as a function of an external driving frequency. In this section the thermal broadening of the resonance line in the presence of a magnetic inhomogeneity shall be discussed. The corresponding systematic shifts are discussed in section 3.3. In section 3.5.1 we will see that also the determination of the modified cyclotron frequency in the magnetic bottle is based on the observation of quantum jumps as a function of an external driving frequency. Thus, the discussion of the line shape covers both the Larmor resonance as well as the modified cyclotron resonance.
The average magnetic field sampled by the axial motion of the proton is given by

$$B(z_0) = B_0 + B_2 \left\langle z_0^2 \right\rangle \quad . \tag{3.9}$$

Thus, both the modified cyclotron frequency ω_+ and the Larmor frequency ω_L, which are both denoted by ω depend on the axial amplitude

$$\omega = \omega_0 \left(1 + \frac{B_2}{B_0} \left\langle z_0^2 \right\rangle\right) = \omega_0 + \delta\omega \quad , \tag{3.10}$$

where ω_0 is the frequency in the minimum of the magnetic bottle and $\delta\omega$ defines the linewidth of the resonance curve. The goal is to extract ω_0 from the lineshapes giving the modified cyclotron frequency and the Larmor frequency for vanishing axial amplitude $z_0 = 0$. Since the axial motion is in thermal equilibrium with its detection system the thermal energy is related to the kinetic energy by the equipartition theorem $E_z = \frac{1}{2} m\omega_z^2 \left\langle z_0^2 \right\rangle = \frac{1}{2} k_B T_z$. Thus, $\delta\omega$ can be expressed in terms of the axial temperature T_z

$$\delta\omega = \omega_0 \frac{B_2}{B_0} \frac{k_B T_z}{m\omega_z^2} \quad . \tag{3.11}$$

For $T_z = 10\,K$, $\omega_z = 740\,kHz$ and $\omega_0 = 50\,MHz$, a linewidth of $\delta\omega = 2\pi \cdot 49\,kHz$ is obtained.
The following discussion is based on a semiclassical theory presented by Brown [48]. The parameter which defines the line shape is $\gamma_z/\delta\omega$ where γ_z is the coupling constant of the

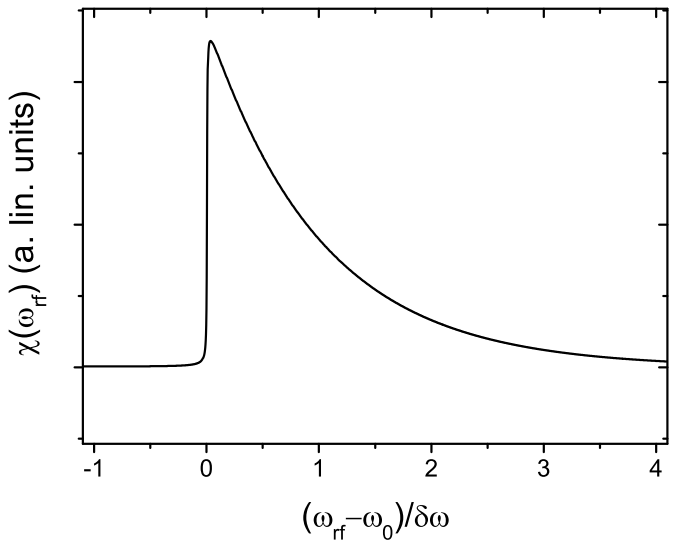

Figure 3.2: The lineshape in the magnetic bottle reflects the thermal distribution of the axial states. The Larmor resonance and the modified cyclotron resonance are given by this lineshape. The abrupt rising at ω_0 gives the respective frequencies in the center of the magnetic bottle. $\delta\omega$ defines the width of the curve and $\delta\omega/\omega_0$ is about one percent for our experimental conditions.

axial detection system (see chapter 4). Since $\gamma_z \ll \delta\omega$ for our experimental conditions, the lineshape is given by

$$\begin{aligned}\chi(\omega_{\rm rf},\delta\omega,\gamma_z) &= \frac{1}{\pi\delta\omega}\left[\arctan\left(\frac{\gamma_z\left(\omega_{\rm rf}-\left(\omega_0+\frac{\gamma_z}{2{\rm Re}\tilde{\gamma}}\delta\omega\right)\right)}{2{\rm Re}\tilde{\gamma}}\right)+\frac{\pi}{2}\right] \\ &\quad\cdot\exp\left(-\frac{\omega_{\rm rf}-\left(\omega_0+\frac{\gamma_z}{2{\rm Re}\tilde{\gamma}}\delta\omega\right)}{\delta\omega}\right) \quad , \end{aligned} \tag{3.12}$$

with $\tilde{\gamma}=\sqrt{\gamma_z^2+4i\gamma_z\delta\omega}$. This line reflects the Boltzmann distribution of the axial states with a sharp edge at ω_0 as shown in Fig. 3.2. Thus, the Larmor frequency and the modified cyclotron frequency can be extracted from this abrupt rising in the resonance line.

3.2.1 Transition rate for the Larmor resonance

In order to drive spin transitions an external magnetic field with amplitude $\vec{b}_{\rm rf}$ is irradiated to the trap. The vector $\vec{b}_{\rm rf}$ is orientated perpendicular to the magnetic field B_0 rotating at the frequency $\nu_{\rm rf}$. On resonance $\nu_{\rm rf}=\nu_L$ the particle sees a constant magnetic field in the ρ-direction and the spin will start to precess around this field component with the

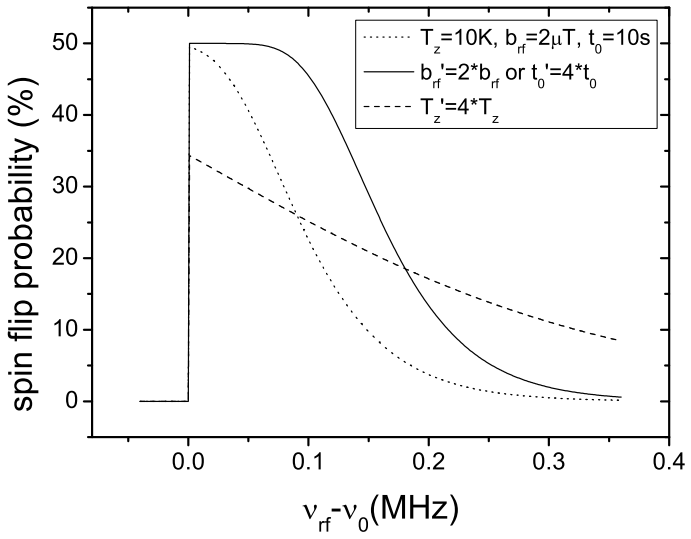

Figure 3.3: The dotted line shows the spin transition rate for an axial temperature of $T_z = 10\,\mathrm{K}$, an external rf-field of $b_{rf} = 2\,\mu\mathrm{T}$ and an irradiation time of $t_0 = 10\,\mathrm{s}$. Since $P_{\mathrm{SF}}(\omega_0) = 50\,\%$ a further increase of the Rabi frequency Ω_R leads to saturation (solid line). A doubling of the external field amplitude b_{rf} has the same effect as an increase of the irradiation time by a factor of four. A higher axial temperature T_z leads to a broadening and a reduction of the maximal spin flip probability P_{SF} (dashed line).

Rabi frequency $\Omega_R = 2\pi\nu_L b_{\mathrm{rf}}/B_0$ [49]. Inside the magnetic bottle the spin-flip probability is given by [48]

$$P_{\mathrm{SF}} = \frac{1}{2}\left(1 - \exp\left(-\frac{1}{2}\Omega_R^2 t_0 \chi(2\pi\nu_{\mathrm{rf}}, B_2, T_z)\right)\right) \quad , \tag{3.13}$$

where t_0 is the irradiation time. A driving field below the resonance frequency ν_L has no effect. P_{SF} increases abruptly to its maximum at the resonance frequency. Increasing b_{rf} or t_0 leads to an increase of the spin flip probability. However, the maximum probability is limited to $P_{\mathrm{SF}} = 50\,\%$. This means that for $P_{\mathrm{SF}}(\nu_L) = 50\,\%$ a further increase of b_{rf} or t_0 saturates the resonance curve, leading to a line broadening. Moreover, the linewidth of the resonance curve broadens by an increase of the axial temperature T_z. This increases the magnetic field region which is sampled by the motion of the proton. Thus, in order to determine ν_L as precisely as possible the Larmor resonance curve should be measured for the lowest achievable temperature T_z. Calculated resonance curves for varying values of T_z and Ω_R are shown in Fig. 3.3.

3.3 Limits for the determination of g in the magnetic bottle

In this section the limitations of a g-factor measurement in the magnetic bottle due to the systematic shifts of the Larmor frequency $\Delta\nu_L$, the modified cyclotron frequency $\Delta\nu_+$

and the axial frequency $\Delta\nu_z$ shall be discussed.
The relative error in the g-factor is given by

$$\frac{\Delta g}{g} = 2\frac{1}{\nu_c}\Delta\nu_L + 2\frac{\nu_L}{\nu_c^2}\Delta\nu_c \quad . \tag{3.14}$$

The dependency of the Larmor frequency on the axial energy has already been discussed in the previous section giving rise to the broad lineshape with a sharp threshold at $\nu_L(E_z = 0)$. However, this frequency is shifted systematically due to the energy in the two remaining eigenmodes E_+ and E_- by

$$\Delta\nu_L = \frac{\nu_L}{4\pi^2 m_p \nu_z^2}\frac{B_2}{B_0}\left(-\frac{\nu_z^2}{\nu_+^2}E_+ - 2|E_-|\right) \quad . \tag{3.15}$$

For a magnetic bottle of $B_2 = 300\,mT/mm^2$ this corresponds to a shift of $\Delta\nu_L/T_+ = -8.4\,Hz/K$ and $\Delta\nu_L/T_- = -9733\,Hz/K$.
The free cyclotron frequency is deduced by the application of the invariance theorem. The contribution of the the magnetron frequency shift can be neglected due to the hierarchy of the three eigenfrequencies leading to the systematic shift

$$\Delta\nu_c = \frac{\nu_+}{\nu_c}\Delta\nu_+ + \frac{\nu_z}{\nu_c}\Delta\nu_z \quad . \tag{3.16}$$

For the energy dependence of ν_+ on the axial energy the same argumentation holds as for the Larmor frequency. Since a measurement of ν_+ reflects the thermal distribution of the axial mode, the frequency $\nu_+(E_z = 0)$ can be identified as the sharp edge in the resonance curve. The systematic shift due to E_+ and E_- is given by

$$\Delta\nu_+ = \frac{\nu_+}{4\pi^2 m_p \nu_z^2}\frac{B_2}{B_0}\left(-\frac{\nu_z^2}{\nu_+^2}E_+ - 2|E_-|\right) \quad . \tag{3.17}$$

For a magnetic bottle of $B_2 = 300\,mT/mm^2$ this corresponds to a shift of $\Delta\nu_+/T_+ = -3\,Hz/K$ and $\Delta\nu_+/T_- = -3481\,Hz/K$.
The axial frequency inside a magnetic bottle is independent of the axial oscillation amplitude since no magnetic moment is generated by this movement. However, the axial frequency strongly depends on the radial momentum. The experimental challenges connected to this scaling are discussed in section 3.5. The systematic shift due to E_+ and E_- is given by

$$\Delta\nu_z = \frac{\nu_z}{4\pi^2 m_p \nu_z^2}\frac{B_2}{B_0}\left(E_+ + |E_-|\right) \quad . \tag{3.18}$$

For a magnetic bottle of $B_2 = 300\,mT/mm^2$ this corresponds to a shift of $\Delta\nu_z = 72\,Hz/K$ for both radial modes.
Combining Eq. (3.14) to (3.18) gives the relative shift of the g-factor

$$\frac{\Delta g}{g} = \frac{2}{4\pi^2 m_p \nu_z^2}\frac{B_2}{B_0}\left(-\frac{\nu_z^2\nu_L}{\nu_+^2\nu_c}E_+ + \left(-2\frac{\nu_L}{\nu_c} + 2\frac{\nu_L\nu_+^2}{\nu_c^3} - \frac{\nu_L\nu_z^2}{\nu_c^3}\right)|E_-|\right) \quad . \tag{3.19}$$

For a magnetic bottle of $B_2 = 300\,mT/mm^2$ *this corresponds to a relative shift of* $\Delta g/gT_+ = -9 \cdot 10^{-7}\,/K$ *and* $\Delta g/gT_- = -2.8 \cdot 10^{-6}\,/K$.
Summarizing, a determination of the g-factor with a relative precision of less than 10^{-9} would require the knowledge of the absolute energy of the radial modes at a precision of about $0.1\,\mu$eV. In addition, this energy has to be stable at a level of $0.1\,\mu$eV during the whole measurement. This is far from experimental feasibility.

3.4 The double-trap setup

In order to overcome the limitations of a g-factor determination in the magnetic bottle, a setup with two separate traps is used. This gives the opportunity to separate the accurate measurement of the eigenfrequencies from the determination of the spin state. The precision trap is located 44 mm from the magnetic bottle of the analysis trap which reduces the magnetic inhomogeneity by a about a factor of 100000 compared to the analysis trap. A magnetic bottle strength of $B_2(PT) \approx 4.7\,\mu\mathrm{T{\cdot}mm^{-2}}$ at the position of the precision trap was extracted from a calculation of the axial magnetic-field component done with COMSOL. This B_2 keeps the bottle-broadening effect to a few ppb. The spin state analysis takes place in the analysis trap (AT) with the strong superimposed magnetic inhomogeneity. The idea of this double trap method was introduced by Häffner and Herrmanspahn [50]. It was successfully applied for the determination of magnetic moments of a single electron bound to a hydrogen-like ion for different ion species [51, 9, 10, 11]. The main challenge of transferring the measurement of the magnetic moment of the bound electron to the proton is the smaller magnetic moment and larger mass of the proton. Accordingly a stronger inhomogeneity is needed (see section 3.1).
The two traps are connected by a transport section, consisting of six electrodes. A schematic of the whole trap stack is shown in Fig. 3.4. The geometric properties of the two traps are listed in Tab. 2.1.
The proposed measurement scheme for the g-factor depicted in Fig. 3.4 is the following:

1. The spin orientation is detected in the analysis trap by driving a spin flip. From the direction of the frequency change the initial and the final spin state can be determined.

2. The proton is transported adiabatically to the precision trap.

3. In the precision trap a spin-flip transition is driven near the expected Larmor frequency. Simultaneously the free cyclotron frequency is measured.

4. The proton is transported adiabatically to the analysis trap.

5. The spin orientation is detected in the analysis trap by driving a spin flip. From the direction of the frequency change the initial and the final spin state can be determined. By comparison of the initial state with the final spin state of step 1

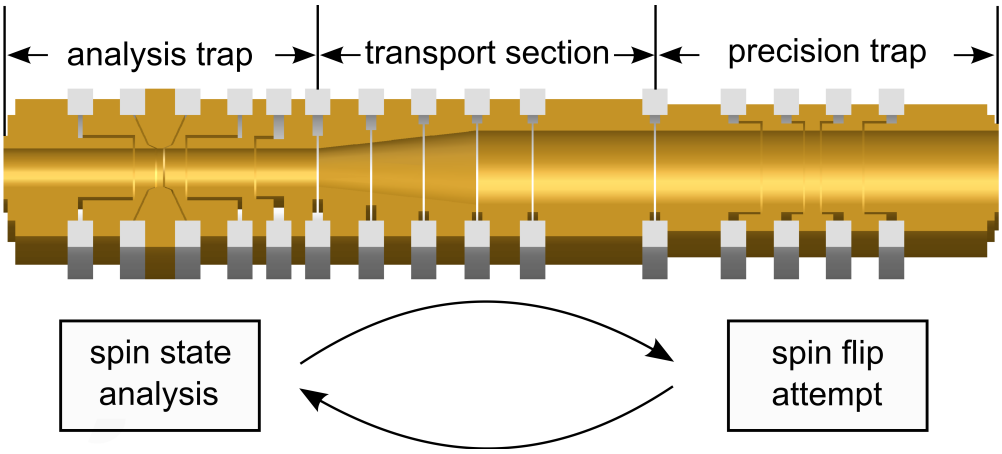

Figure 3.4: The double-Penning trap setup consists of the analysis trap on the left and the precision trap on the right side. Transport electrodes between both traps are used for the transport of the proton.

(i. e. the spin state of the proton before the transport to the precision trap and after the return from the precision trap) the success of the spin flip attempt in the precision trap can be judged.

This cycle is repeated several hundred times for different driving frequencies ν_{rf} in the precision trap. Thus, the measurement of ν_L takes place in the homogeneous magnetic field of the precision trap. Since the free cyclotron frequency is determined simultaneously to the spin transition, the measurement is not sensitive to magnetic field drifts or fluctuations.

3.5 The magnetic bottle - a challenging experimental environment

The main experimental challenge for the determination of the g-factor of the proton is the ability to resolve spin transitions. In the presence of a magnetic inhomogeneity not only the spin magnetic momentum but also the orbital magnetic momentum changes the axial frequency. Thus, the axial frequency shift in terms of the quantum numbers is given by

$$\Delta\nu_z(n_+, n_-, m_s) = \frac{h\nu_+}{4\pi^2 m_p \nu_z^2}\frac{B_2}{B_0}\left(n_- + \frac{1}{2} + \frac{\nu_-}{\nu_+}\left(n_+ + \frac{1}{2}\right) + \frac{g}{2}m_L\right) \quad . \tag{3.20}$$

The axial frequency shift due to a quantum jump of the modified cyclotron motion is $\Delta\nu_z(\Delta n_+ = \pm 1) = 61\,mHz$. *A change of the magnetron quantum number causes a frequency jump of* $\Delta\nu_z(\Delta n_- = \pm 1) = 49\,\mu Hz$. *A spin flip leads to* $\Delta\nu_{z,SF} = 171\,mHz$.
The remarkable property of Eq. (3.20) is

$$\frac{\Delta\nu_z(\Delta m_L = 1)}{\Delta\nu_z(\Delta n_+ = 1)} = \frac{g}{2} \quad . \tag{3.21}$$

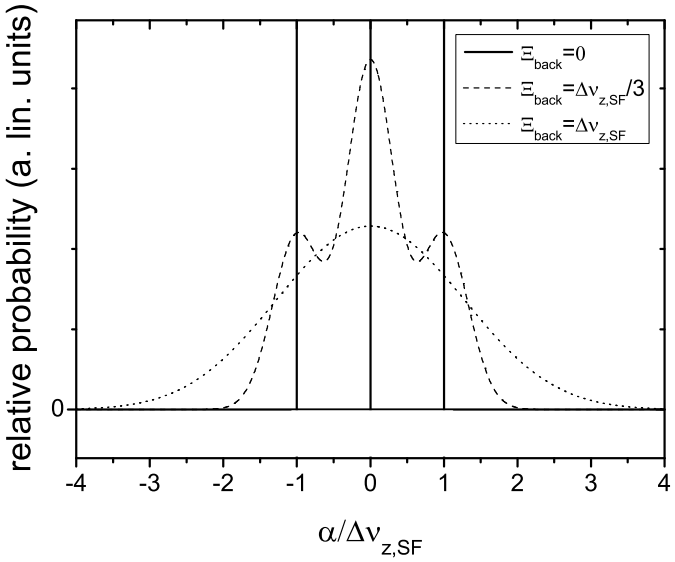

Figure 3.5: Histogram of the axial frequency differences α_{SF} for three different magnitudes of the background fluctuation Ξ_{back}. For a stable axial frequency three sharp peaks are obtained as shown by the solid lines. For an axial frequency fluctuation of $\Xi_{\mathrm{back}} = \Delta\nu_{z,\mathrm{SF}}/3$ the three peaks broaden (dashed curve). For the dotted curve where $\Xi_{\mathrm{back}} = \Delta\nu_{z,\mathrm{SF}}$ the three distributions cannot be distinguished anymore.

Already three quantum jumps of the modified cyclotron mode cause a larger shift of the axial frequency than a spin transition. This ratio cannot be modified by the size of the magnetic bottle or any adjustable parameter.
The energy of the modified cyclotron motion E_+ is defined by the interaction with a dedicated detection system connected to the precision trap. Thus, the mean energy of a proton transported to the analysis trap is given by $E_+ \approx 0.3\,meV$ ($T_+ \approx 4\,K$). Consequently, for a successful detection of a spin transition the radial energy has to be stable at $\Delta E_+/E_+ \approx 10^{-4}$.
However, changes in the radial quantum numbers cannot be avoided completely. But due to different optimization steps we were able to suppress these fluctuations more and more. In this section two different detection schemes for the g-factor will be discussed. The feasibility of these methods depends on the achievable axial frequency stability.

We define α as the frequency difference between to consecutive axial frequency measurements separated by the time t and $t + T$

$$\Delta\nu_z = \nu_z(t) - \nu_z(t+T) = \alpha \quad . \tag{3.22}$$

The frequency difference between two axial frequency measurements separated by a spin flip drive is defined as α_{SF}. The three possible values for α_{SF} are

$$\alpha_{\mathrm{SF}} = -\Delta\nu_{z,\mathrm{SF}} \quad \vee \quad \alpha_{\mathrm{SF}} = 0 \quad \vee \quad \alpha_{\mathrm{SF}} = +\Delta\nu_{z,\mathrm{SF}} \quad . \tag{3.23}$$

The solid line in Fig. 3.5 shows the corresponding three sharp peaks in a histogram for α for a series of trials. The instability of the axial frequency leads to a broadening of these peaks. We quantify this instability by the standard deviation Ξ of the axial frequency differences α_i

$$\Xi = \sqrt{\frac{1}{N-1}\sum_{i=1}^{N}\left(\alpha_i - \bar{\alpha}\right)^2} \quad , \tag{3.24}$$

which we call the axial frequency fluctuation. We define α_{back} as the difference between two axial frequency measurements without an external driving field. Consequently, the three peaks will be broadened by Ξ_{back} as shown by the dashed curve in Fig. 3.5 or by the dotted curve for even larger Ξ_{back}.

3.5.1 Determination of the *g*-factor via a statistical detection scheme

We will first discuss the case where $\Xi_{\mathrm{back}} \approx \Delta\nu_{z,\mathrm{SF}}$. The triple signature is smeared out but still α_{SF} will be larger than α_{back} on average. This means that M spin flips in N cycles will lead to a broadening of the frequency fluctuations Ξ_{SF} compared to the case where no spin flips are induced by

$$\begin{aligned}\Xi_{\mathrm{SF}} &= \sqrt{\sum_{i}^{M}\frac{\left(\alpha_i \pm \Delta\nu_{z,\mathrm{SF}} - \bar{\alpha}\right)^2}{N-1}\sum_{i=M}^{N}\frac{\left(\alpha_i - \bar{\alpha}\right)^2}{N-1}} \\ &\approx \sqrt{\Xi_{\mathrm{back}}^2 + P_{\mathrm{SF}}\Delta\nu_{z,\mathrm{SF}}^2} \quad .\end{aligned} \tag{3.25}$$

Turning it around, the spin flip probability for a given driving frequency can be determined by comparing Ξ_{SF} and Ξ_{back}

$$P_{\mathrm{SF}} \approx \frac{\Xi_{\mathrm{SF}}^2 - \Xi_{\mathrm{back}}^2}{\Delta\nu_{z,\mathrm{SF}}^2} \quad . \tag{3.26}$$

By scanning the external driving frequency, the Larmor resonance curve can be detected. We call this a statistical detection of the Larmor frequency since spin flips can only be observed for an ensemble of attempts [52].

To obtain a value for g, the modified cyclotron frequency has to be measured in the magnetic bottle. Here, we want to discuss the statistical detection of ν_+ which is carried out in the same way as for the Larmor frequency (a less precise but much faster method is described in chapter 8).
Quantum transitions Δn_+ are induced between two axial frequency measurements $\alpha_{\Delta n+}$ by an external driving field. An explicit relation like Eq. (3.26) for the transition probability in terms of the frequency fluctuations $\Xi_{\Delta n+}$ and Ξ_{back} cannot be given. Since the modified cyclotron mode is not a two-level-system the number of quantum transitions for each $\alpha_{\Delta n+}$ can be more than just one. Nevertheless, an increase of $\Xi_{\Delta n+}$ can still be observed for a resonant driving field. Thus, the axial frequency fluctuation $\Xi_{\Delta n+}$ as a function of the

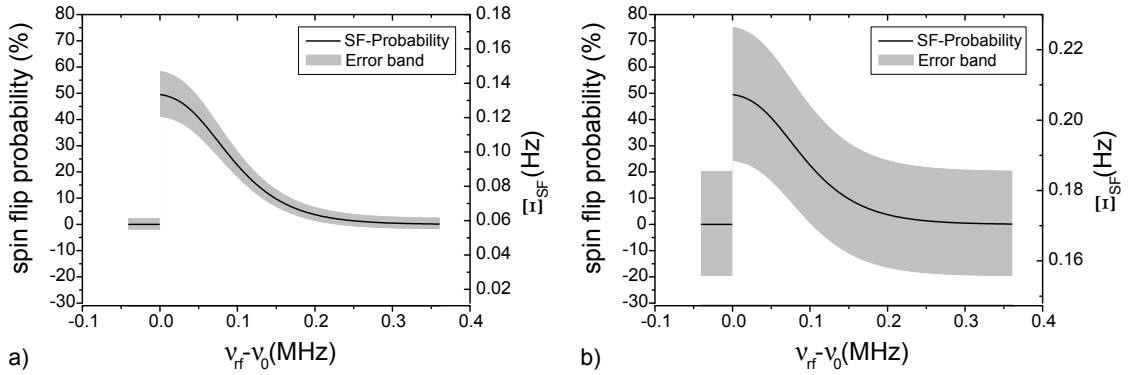

Figure 3.6: Theoretical Larmor resonance curves obtained for the statistical method. The frequency fluctuation Ξ_{SF} The grey band indicates the error for $N = 100$ cycles for each datapoint. In a) a background fluctuation of $\Xi_{\mathrm{back}} = \Delta\nu_{z,\mathrm{SF}}/3$ was assumed. For a higher background fluctuation $\Xi_{\mathrm{back}} = \Delta\nu_{z,\mathrm{SF}}$ as shown in b) the resolution limit is reached.

external driving frequency reassembles the lineshape χ of Eq. (3.12) from which $\nu_+(E_z = 0)$ can be extracted [47].

In order to avoid systematic errors in the measurement of ν_+ the amplitude of the driving field is kept very weak. Thus, approximately the same quantum state n_+ is maintained over the whole measurement process.

In pinciple, the statistical method is applicable for any magnitude of the background fluctuations Ξ_{back}. However, the error of Ξ for N sequences is given by

$$\sigma_\Xi = \frac{\Xi}{\sqrt{2N-2}} \quad . \tag{3.27}$$

Thus the resolution limit is reached if the error

$$\Delta P_{\mathrm{SF}} \quad = \quad \frac{2}{\Delta\nu_{z,\mathrm{SF}}^2\sqrt{2N-2}}\sqrt{\Xi_{\mathrm{back}}^4 + \Xi_{\mathrm{SF}}^4} \tag{3.28}$$

is larger than the difference between the maximum and the minimum of the resonance curve which we define as $\beta = P_{\mathrm{SF,max}} - P_{\mathrm{SF,min}}$. To illustrate this limit, resonance curves for different magnitudes of Ξ_{back} are shown in Fig. 3.6.

3.5.2 Analysing individual spin flip drives to determine the *g*-factor

The statistical method is a very effective scheme to extract the Larmor frequency in the analysis trap for a comparably large instability of the axial frequency. However, this scheme is not suited for the double-trap technique presented in section 3.4. Here, the proton arrives with an unknown spin state in the analysis trap. But the knowledge of this initial spin state is required for the determination of the success of the spin flip attempt in the precision trap. Thus, spin transitions are induced until a frequency jump of $+\Delta\nu_{z,\mathrm{SF}}$ or $-\Delta\nu_{z,\mathrm{SF}}$ is detected, giving the desired spin state information. Comparing this to the statistical method means that every single α has to be assigned to

$$\text{Spin state changed} \quad \vee \quad \text{Spin state remained unchanged} \quad . \tag{3.29}$$

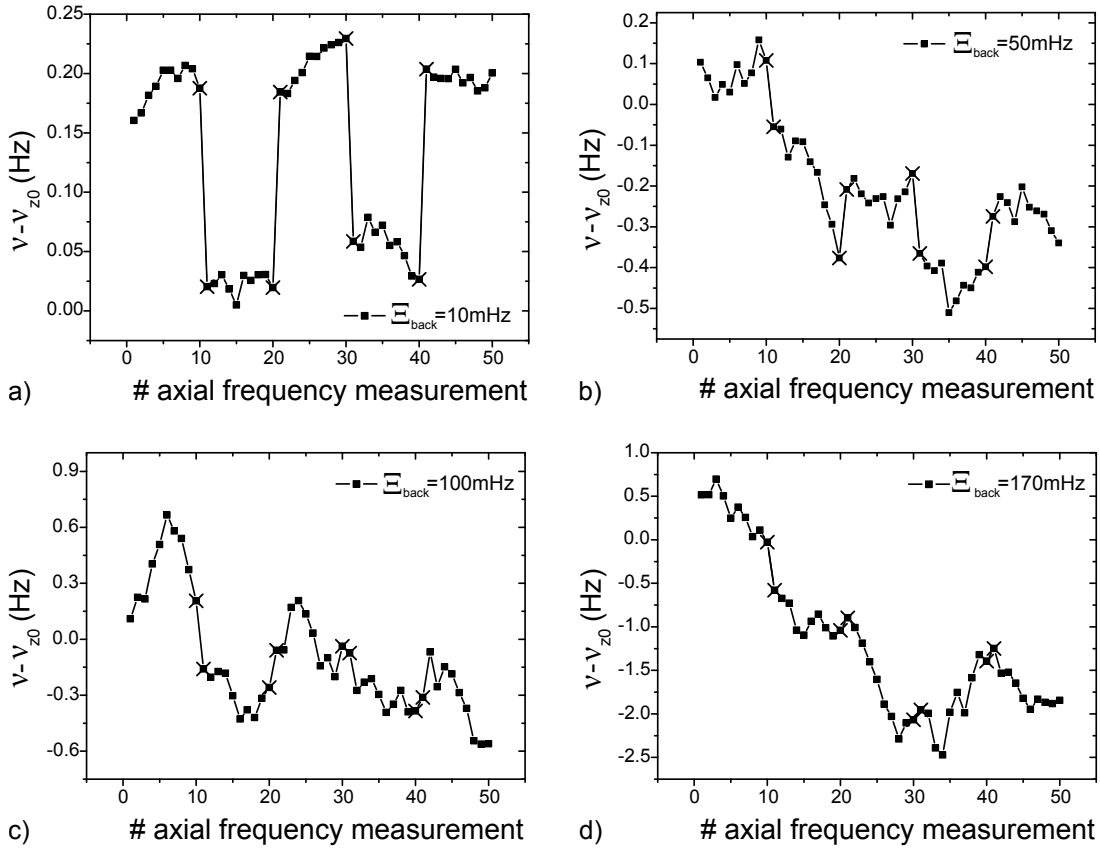

Figure 3.7: Simulated successive measurements of the axial frequency are plotted for various background fluctuations Ξ_{back} to illustrate the challenge of identifying spin transitions. Between the crossed data points a spin flip is induced. In a) all spin transitions are clearly visible. In b) the fluctuations complicate the identification. Even higher background fluctuations are shown in c) and d).

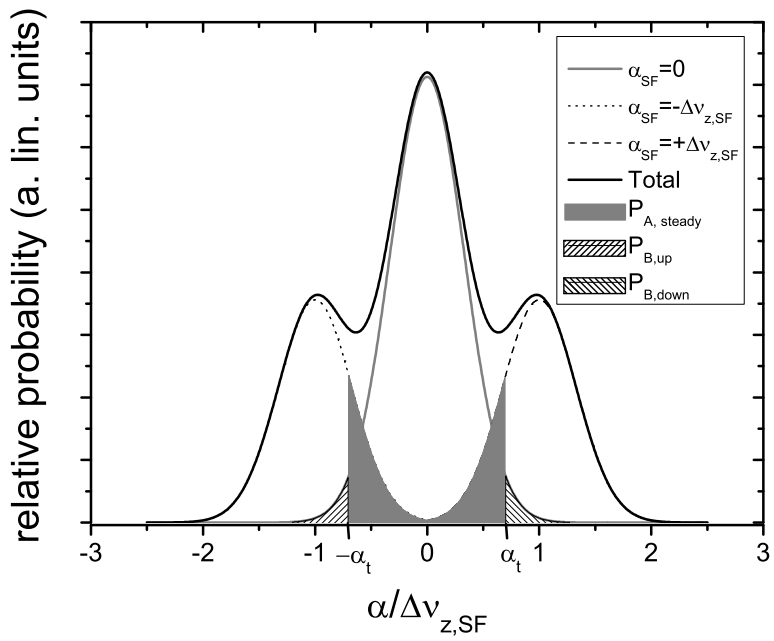

Figure 3.8: In order to obtain the error probabilites for the spin state analysis for a certain threshold α_t, the particular areas of the frequency fluctuation distributions are calculated. The grey area gives the probability that a spin flip is not detected. The dashed areas give the probability that a spin flip has been detected although the spin state remained unchanged. for more details see text.

For an unstable axial frequency the distributions of spin flip attempts overlap as already shown in Fig. 3.5 in the previous section. Accordingly, the same axial frequency difference α can either correspond to a spin transition or not. In Fig. 3.7 sequences for axial frequency measurements for various background fluctuations are shown, indicating that the correct assignment of spin transitions gets more difficult for increasing Ξ_{back}. False classifications of α will decrease the resolution β of the resonance curve. The Rabi frequency is adjusted to obtain $\beta \approx 50\%$ without saturation. Two cases have to be considered:

- **A**: a spin flip has been assigned although the spin state was not changed. Thus, the baseline of the resonance rises by the corresponding probability P_A.
- **B**: no spin flip has been assigned although the spin state changed. This decreases the measured probability by P_B.

Whether the resonance curve can be resolved strongly depends on the magnitude of the axial frequency fluctuations in the analysis trap. The following discussion focuses on the measurement of a Larmor resonance curve in the analysis trap.
The attainable resolution in terms of Ξ_{back} can be calculated if we choose a decision rule

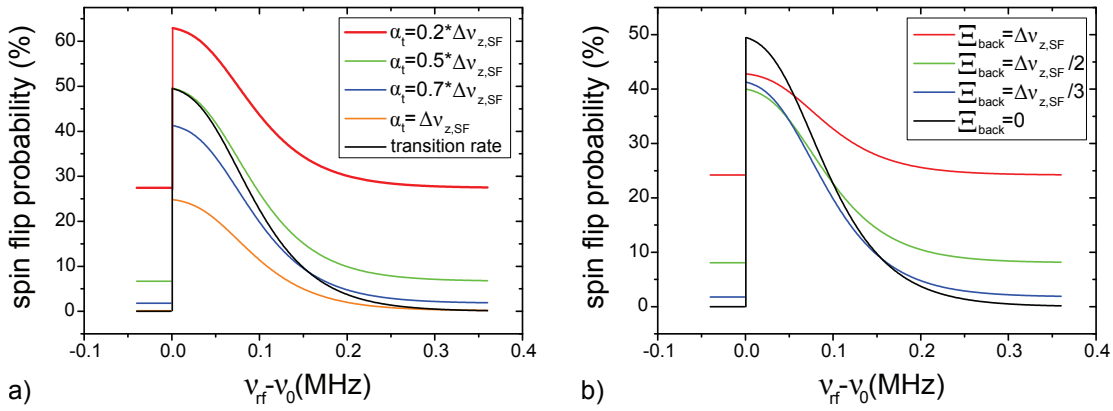

Figure 3.9: Theoretical Larmor resonance curves for the direct detection scheme. In a) the effect of a varying threshold α_t is shown for a background fluctuation of $\Xi_{\mathrm{back}} = \Delta\nu_{z,\mathrm{SF}}/3$. In b) the effect of a varying background fluctuation for a threshold of $\alpha_t = 0.7 \cdot \Delta\nu_{z,\mathrm{SF}}$ is shown.

for α as shown in Fig. 3.8. All $\alpha > \alpha_t$ are assigned to a spin flip and all $\alpha < \alpha_t$ are related to an unchanged spin state. The error probabilities P_A and P_B are given by

$$P_A = \left[\int_{\alpha_t}^{\infty} g(\Xi_{\mathrm{back}}, 0)\mathrm{d}\alpha + \int_{-\infty}^{-\alpha_t} g(\Xi_{\mathrm{back}}, 0)\mathrm{d}\alpha\right](1 - P_{\mathrm{SF}}) \tag{3.30}$$

$$P_B = \left[\int_{-\alpha_t}^{\infty} g(\Xi_{\mathrm{back}}, -\Delta\nu_{\mathrm{SF}})\mathrm{d}\alpha + \int_{-\infty}^{\alpha_t} g(\Xi_{\mathrm{back}}, +\Delta\nu_{\mathrm{SF}})\mathrm{d}\alpha\right] P_{\mathrm{SF}}/2 \quad , \tag{3.31}$$

where $g(\sigma, x)$ is the Gauss-function with standard deviation σ centered around x. The effect of α_t on the Larmor resonance is shown in Fig. 3.9a). The resolution of the resonance curve decreases with increasing Ξ_{back} as shown in Fig. 3.9b). Again, the resolution limit is reached if the error ΔP_{SF} is larger than the resolution β. The error ΔP_{SF} in terms of the number of measurements N is described by the standard deviation of the corresponding binomial distribution

$$\Delta P_{\mathrm{SF}} = \left(P_{\mathrm{SF}} N + \sqrt{N P_{\mathrm{SF}}(1 - P_{\mathrm{SF}})}\right)/N \quad . \tag{3.32}$$

In Fig. 3.10 the direct method and the statistical method are compared for $\Xi_{\mathrm{back}} = \Delta\nu_{z,\mathrm{SF}}/3$ and $\alpha_t = 0.5 \cdot \Delta\nu_{z,\mathrm{SF}}$. An obvious drawback of the direct detection scheme is the decreased resolution of the Larmor resonance due to the overlap of the distributions for α. Thus, for a measurement of the Larmor frequency in the magnetic bottle, the statistical method should be applied.

However, even in the presence of background fluctuations of $\Xi_{\mathrm{back}} = \Delta\nu_{z,\mathrm{SF}}/3$, the Larmor resonance curve can be resolved utilizing the direct detection scheme as shown in Fig. 3.10. This means that the success of each individual spin flip drive in the analysis trap can be determined with low uncertainty. This is exactly the purpose of the analysis trap in the double-trap technique, where the spin state of the proton arriving in the analysis trap has to be determined. Thus, the double-trap technique is feasible despite low background

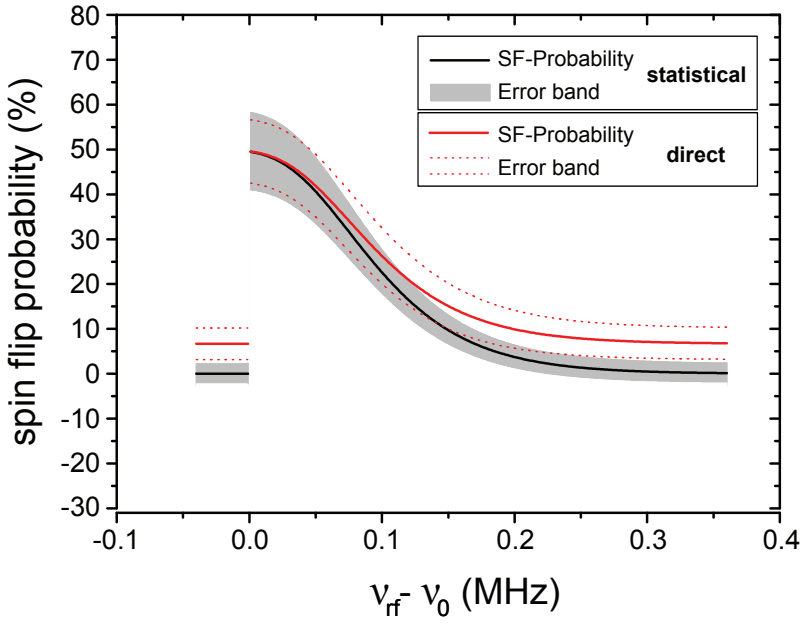

Figure 3.10: Theoretical Larmor resonance curves for background fluctuations of $\Xi_{\mathrm{back}} = \Delta\nu_{z,\mathrm{SF}}/3$. The statistical detection scheme is shown in black. The threshold for the direct detection scheme shown in red is given by $\alpha_t = 0.5 \cdot \Delta\nu_{z,\mathrm{SF}}$. For the direct detection scheme, the baseline is slightly raised by 7 % due to the overlap of the three distributions of α. The error bands for both techniques are comparable.

fluctuations Ξ_{back}. The reduction of Ξ_{back}, which would render possible the application of the double-trap technique, was one of the main tasks of this thesis. In chapter 8 resonance curves for both detection schemes will be presented indicating that the double-trap technique can be applied.

Chapter 4

Detection of eigenmotions

A significant benefit of Penning traps is the weak coupling of the trapped particle to the outer environment which makes it an ideal system for high-precision measurements. However, to determine the g-factor of the proton the motional frequencies have to be measured. The difficulty is to build a detector which is sensitive to the motion of a single particle. Thus, the design and optimization of the detection systems is one of the key issues for a successful high-precision Penning trap experiment.
In principle the interaction of the ion inside the trap with a resistor attached to one of the electrodes has to be investigated [53, 54]. Two different cases have to be discussed: In the first case, the ion acts as a current source leading to a voltage drop across the resistor. This voltage is amplified by a cryogenic amplifier to become the detected signal. In the second case, the ion acts as a perfect conductor at its resonance frequency, thus shortening the thermal noise of the resistor. The resulting signal also passes the cryogenic amplifier and is monitored in frequency domain. In both cases, the frequency can be determined by a fit to the resulting lineshape in the frequency spectrum. For a fast and precise determination of the particles frequency, a high signal-to-noise-ratio SNR is required. As will be explained in this chapter this requires a high resistance for both detection schemes. The realization of the detection system is explained in the first section. The two detection schemes are discussed in section 4.2 and section 4.3. In principle, only one detection system for one motional mode is needed to measure all eigenfrequencies of the ion. The frequency information of the two remaining modes can be obtained by a sideband-coupling to the detectable mode as explained in section 4.4. The possibility to manipulate the detector and the energy of the particle by active electronic feedback is the topic of section 4.5. In section 4.6 the so-called transient recorder is described - a tool for the continuous monitoring of a motional frequency.
The last part summarizes the main parameters of our detection systems.

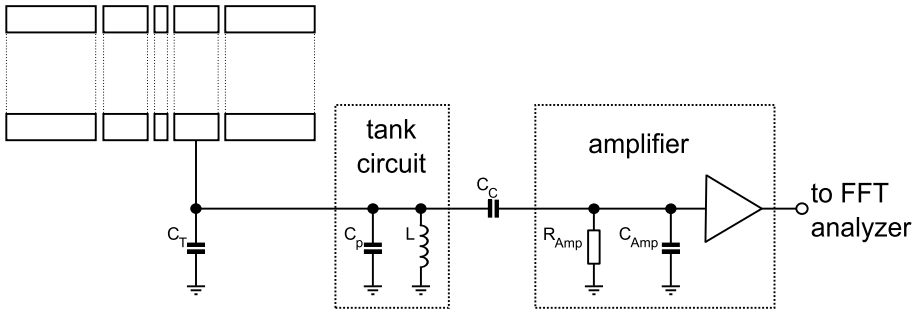

Figure 4.1: Sketch of the detection system. A coil with inductance L and parasitic capacitance C_p is attached to one electrode with parasitic capacitance C_T. The amplifier with input impedance R_{Amp} and parasitic capacitance C_{Amp} is connected to the tank circuit by the coupling capacitance C_c. The signal is monitored with an FFT-analyser

4.1 The detection system

The realization of a high resistance in parallel to the trap is hindered by the parasitic capacitances of the trap electrodes. This can be overcome by connection of an inductance to the electrode, which forms a parallel circuit with a high resistance at its resonance frequency. The properties of the tank circuit are discussed in this section.
The whole detection system consists of an inductor L attached to one electrode followed by a low-noise amplifier as shown in Fig. 4.1. The inductor forms together with the trap capacitance C_T, its own parasitic capacitance C_P and the amplifier capacitance C_{Amp} a resonant circuit. In order to calculate the resonance frequency

$$\omega_{LC} = 1/\sqrt{LC_{\text{sys}}} \quad , \tag{4.1}$$

the system capacitance C_{sys} has to be determined. Taking into account the coupling capacitance C_C between tank circuit and amplifier, the system capacitance is given by

$$C_{\text{sys}} = C_T + C_P + \frac{C_{\text{Amp}}}{\kappa} \quad , \tag{4.2}$$

where the coupling constant κ is defined by

$$\kappa = \frac{C_C + C_{\text{Amp}}}{C_C} \quad . \tag{4.3}$$

The impedance of a parallel LC-circuit is given by

$$Z(\omega) = \frac{1}{\frac{1}{R_p} + i\left(\omega C_{\text{sys}} - \frac{1}{\omega L}\right)} \quad , \tag{4.4}$$

where R_p is the effective resistance on resonance

$$Z(\omega_{\text{LC}}) = R_p = Q\omega_{LC}L \quad , \tag{4.5}$$

which is proportional to the Q-value of the tank circuit, a measure of the energy loss per oscillation cycle. As we will see in section 4.2 and 4.3 a high resonance resistance is

mandatory for the detection of the oscillation of a single ion. The first task in order to obtain a high resonance resistance R_p is the design of a high-Q resonant circuit. Detailed descriptions of the optimization process to obtain tank circuits with high quality factors can be found in [45, 55, 56, 57].
In the following, the influence of the amplifier on the parallel resistance is investigated. The input resistance R_{Amp} of the amplifier modifies the total system resistance

$$R_{\mathrm{sys}} = \frac{1}{\kappa^2}\frac{R_p R_{\mathrm{Amp}}}{R_p + R_{\mathrm{Amp}}/\kappa^2} \tag{4.6}$$

$$= \frac{R_p}{1 + \kappa^2 R_p/R_{\mathrm{Amp}}} \quad . \tag{4.7}$$

In order to avoid a decrease of R_p by connecting the amplifier to the tank circuit, a high input resistance of the amplifier is needed. A weaker coupling of amplifier and tank circuit by reducing C_C would have the same effect but also affects the signal strength which will be discussed in the next section when the signature of the ion's motion is introduced. Thus, the design of a cryogenic amplifier with high input resistances is the second crucial task for a high resonance resistance which is presented in [45, 57, 58].
For the discussion of the SNR, the noise properties of the detection system are investigated. The noise e_n of the whole system at the input of the amplifier is given by the thermal noise of the tank circuit e_{th}, the input voltage noise e_{Amp} and the current noise i_{Amp} of the amplifier by

$$e_n^2 = e_{\mathrm{th}}^2 + e_{\mathrm{Amp}}^2 + i_{\mathrm{Amp}}^2 R_{\mathrm{sys}}^2 \kappa^2 \quad . \tag{4.8}$$

The thermal noise is given by the Johnson-Noise [59]

$$e_{th} = \sqrt{4 k_B T R_{\mathrm{sys}} \kappa^2} \tag{4.9}$$

of the tank circuit. It is reduced by κ^2 due to the coupling capacitance C_C. Since the contribution of the thermal noise is much higher than that by the current noise Eq. (4.8) can be simplified to

$$e_n^2 = e_{\mathrm{th}}^2 + e_{\mathrm{Amp}}^2 \quad . \tag{4.10}$$

4.2 Peak detection - signature of an excited ion

In this section the signature of an excited ion shall be discussed. *Excited* means, that the motional amplitude ρ_i of the mode i (i denoting the three eigenmotions $+, -, z$) is larger than in thermal equilibrium with the detection system. We are able to excite the three eigenmodes by application of an rf-field at frequency ω_i to one electrode of the trap. In case of the axial mode we call this a *dipole-excitation*. For the radial modes one half of a split electrode is used which we call a *quadrupole-excitation*. Consequently, the oscillatory motion of the ion induces a current

$$I = \frac{q}{D_i}\dot{\rho}_i = \frac{q}{D_i}\omega_i \rho_i \tag{4.11}$$

in the trap electrodes. The parameter D_i is called the *effective electrode distance* and characterizes the coupling strength of the ion to the resonant circuit. The magnitude of D_i can be calculated analytically by the determination of the Green's-function of a specific trap geometry [45]. The signal at the input of the amplifier is given by the voltage drop across the system resistance R_{sys}:

$$U = R_{\mathrm{sys}} I \kappa^2 \quad . \tag{4.12}$$

Thus, a peak appears in the frequency spectrum on top of the noise resonance of the tank circuit from which the oscillation frequency of the ion can be determined.
The SNR can be calculated by the ratio of Eq. (4.12) and Eq. (4.10)

$$\mathrm{SNR}^2 = \frac{(R_{\mathrm{sys}} I \kappa)^2}{4 k_B T R_{\mathrm{sys}} \kappa^2 + e_{\mathrm{Amp}}^2} \quad , \tag{4.13}$$

which is proportional to the square of the motional amplitude ρ_i. However, a higher amplitude increases the sensitivity to inhomogeneities of the trapping fields which would cause unwanted shifts of the motional frequencies. Thus, low-noise amplifiers and high system resistances are needed to obtain a high SNR for the detection of small motional amplitudes. There exists an optimal coupling factor κ_{opt} for which the SNR is maximized

$$\kappa_{\mathrm{opt}} \approx \left(\frac{e_{\mathrm{Amp}}^2}{4 k_B T R_p^2 / R_{\mathrm{Amp}}} \right)^{\frac{1}{4}} \quad . \tag{4.14}$$

Summarizing, the sensitivity of a single particle detector is based on the careful design of

- an inductance with a high quality factor Q
- an amplifier with high input resistance R_{Amp} and low-noise characteristics e_{Amp}.

4.3 Dip detection - signature of a thermalized ion

The voltage drop induced by the motion of the ion produces a force which modifies the equation of motion

$$\ddot{\rho}_i + \omega_i^2 \rho_i = -\frac{q^2}{m_p D_i^2} \dot{\rho}_i Z_i(\omega) \quad . \tag{4.15}$$

The additional force opposes the motion of the ion and results in a damping with the time constant

$$\tau = \frac{1}{\gamma} = \frac{m D_i^2}{Re\,|Z_i|\,q^2} \quad . \tag{4.16}$$

After several τ the motion of the ion will reach thermal equilibrium with the tank circuit. The time averaged energy in the mode i will then be equal to the thermal energy at the detector temperature T_i

$$\langle E_i \rangle = \frac{1}{2} m \omega_i^2 \left\langle \rho_i^2 \right\rangle = \frac{1}{2} k_B T_i v. \tag{4.17}$$

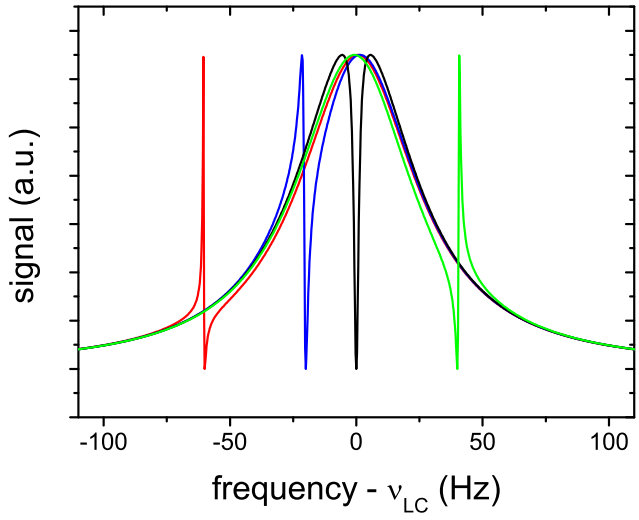

Figure 4.2: The interaction of the thermalized ion with the tank circuit can be modeled as a series lc-circuit in parallel to a parallel LC-circuit. The real part $Re\,|Z_i|$ of the transfer function is plotted for various particle frequencies. The detection system parameters are listed in Tab. 4.1. Since the inductance of the tank circuit is orders of magnitudes smaller than the equivalent inductance l of the ion, the linewidth of the dip signal is about two orders of magnitude narrower than the resonance curve of the tank circuit.

Since the detection systems are operated at cryogenic temperatures, this process, called *resistive cooling*, is the standard technique to cool the motion of the particle.
The characteristics of a thermalized ion can be investigated by inserting the induced current of Eq. (4.11) into Eq. (4.15). One obtains

$$m\frac{D_i^2}{q^2}\dot{I} + Z_i(\omega)I + \frac{m\omega_i^2 D_i^2}{q^2}\int dtI = 0 \tag{4.18}$$

an equation similar to that of a series lc-circuit

$$l\dot{I} + rI + 1/c\int dtI = 0 \quad . \tag{4.19}$$

Thus, the particle can be interpreted as a series lc-circuit with

$$l = m\frac{D_i^2}{q^2} \text{ and } c = \frac{q^2}{m\omega_i^2 D_i^2} \quad , \tag{4.20}$$

which has a vanishing resistance on resonance. This means that the particle shortens the thermal noise resonance of the tank circuit at its oscillating frequency $\omega_i = (lc)^{-1/2}$, which provides a second possibility to measure the eigenfrequency but in contrast to the scheme presented in the previous section now at low particle energies.
The exact line shape of the so-called dip can be determined by investigation of the

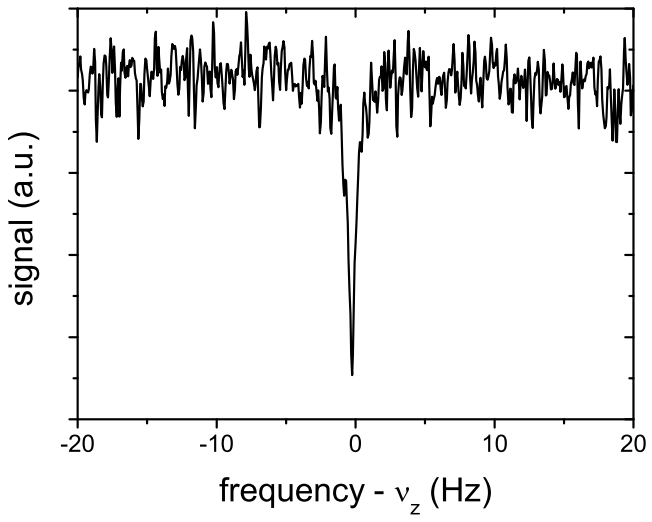

Figure 4.3: A single proton in thermal equilibrium with the axial detection system in the analysis trap is shown (for parameters see Tab. 4.1).

impedance of a series lc-circuit in parallel to a parallel LC-circuit. The observed frequency spectrum is given by the thermal noise of the real part of the impedance

$$\begin{aligned} Re\,|Z_i| &= \frac{1/R_{\mathrm{sys}}}{1/R_{\mathrm{sys}}^2 + \left(\left(\omega C_{\mathrm{sys}} - \frac{1}{\omega L}\right) - \left(\omega l - \frac{1}{\omega c}\right)^{-1}\right)^2} \\ &= \frac{R_{\mathrm{sys}}}{1 + \left(Q\left(\frac{\omega}{\omega_{\mathrm{LC}}} - \frac{\omega_{\mathrm{LC}}}{\omega}\right) - \Delta\omega_i\left(\omega - \frac{\omega_i^2}{\omega}\right)^{-1}\right)^2} \quad , \end{aligned} \tag{4.21}$$

which is shown in Fig. 4.2 for various particle frequencies. $\Delta\omega_i = R_{\mathrm{sys}}/l$ defines the width of the dip on resonance ($\omega_i = \omega_{\mathrm{LC}}$)

$$\Delta\nu_i = \frac{\Delta\omega_i}{2\pi} = \frac{1}{2\pi\tau} = \frac{R_{\mathrm{sys}}q^2}{2\pi m D_i^2} \quad . \tag{4.22}$$

For small particle numbers N (uncorrelated case) the width scales proportional to N [60]

$$\Delta\nu_i = \frac{N R_{\mathrm{sys}}q^2}{2\pi m D_i^2} \quad , \tag{4.23}$$

which is utilized for the production of a single proton in the trap as will be discussed in chapter 6.

The resulting frequency spectrum consists of the thermal noise of $Re\,|Z_i|$, the current noise i_{Amp} and the voltage noise e_{Amp} of the amplifier. A spectrum of a single proton in thermal equilibrium with the axial detection system in our analysis trap is shown in Fig. 4.3.

The frequency information of the ion's motion is encoded in the thermal noise giving the

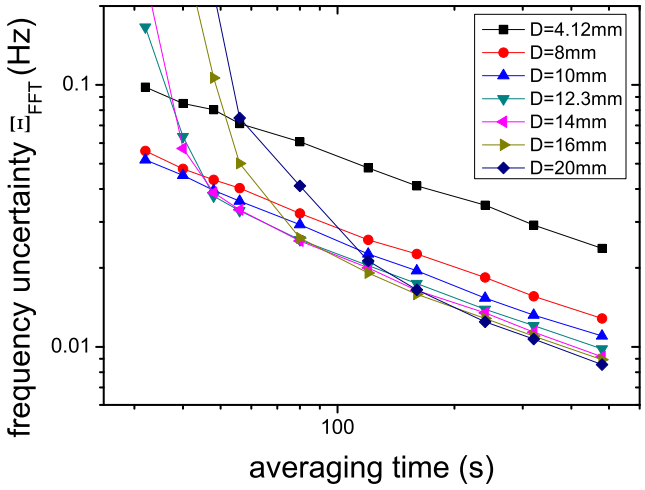

Figure 4.4: Simulated frequency uncertainty Ξ_{FFT} as a function of averaging time T for the dip technique. The parameters for the axial detection system for the analysis trap were utilized for the simulation. The effective electrode distance D was varied, which modifies the linewidth of the noise dip. The frequency uncertainty decreases due to averaging of the thermal noise. A sharper dip yields a more precise determination of the motional frequency. For short averaging times, the dip cannot be resolved reliably for large effective electrode distances, which increases the frequency uncertainty.

SNR per unit bandwidth

$$\mathrm{SNR}^2 = \frac{4k_BTRe\,|Z_i| + i_{\mathrm{Amp}}^2 Re\,|Z_i|^2\kappa^2}{e_{\mathrm{Amp}}^2} \quad . \tag{4.24}$$

Since a higher SNR allows for a faster measurement, a large resistance R_{sys} is required. However, increasing R_{sys} also affects the width of the dip and thus the precision with which the frequency of the ion can be determined.
This is investigated by a Monte Carlo Simulation, reproducing $n = 5000$ noise spectra of a single proton (as shown in Fig. 4.3) for various averaging times. In Fig. 4.4 the frequency uncertainty Ξ_{FFT} is plotted for various effective electrode distances $D_{z(\mathrm{AT})}$ as a function of the averaging time. Two informations can be obtained:

- the frequency uncertainty scales $\propto 1/\sqrt{T}$ favoring a longer averaging process.
- in general a sharper dip allows for a more precise frequency determination. In practice there is a limit for short measurement times due to the Fourier limit.

However, both conclusions are only valid for an absolutely stable motional frequency, which is not fulfilled in a real experiment. A drift or fluctuations of the oscillation frequency counteract the benefit of a longer averaging time. The experimental optimal averaging

time T_{opt} strongly depends on the achievable stability of the motional frequency as will be discussed in chapter 8. Typical averaging times are in the range of 40 to 90 s. Thus, the design of a detection system should be focused on highest frequency resolution in this regime.

4.4 Sideband coupling

A detection system for the axial mode is connected to both of our traps which is used for two different purposes: First, we can cool the eigenmode to the ambient cryogenic temperature. Second, we can measure the axial frequency with the dip technique. In addition we can couple the remaining modes to the axial mode by application of a quadrupole field of the form $z\vec{e}_\rho + \rho\vec{e}_z$ [61]. In this section we describe how this coupling allows us to control the temperature of the radial modes and measure ω_- and ω_+ with the axial detection system.
For a resonant coupling field $\omega_{\mathrm{rf}} = \omega_z \pm \omega_\mp$ we obtain classical Rabi oscillations [49].
In **time domain** this appears as an amplitude modulation of each mode

$$z(t) = z_0 \sin\left(\frac{\Omega_0}{2}t\right)\sin\left(\omega_z t\right) \tag{4.25}$$

$$\rho_\pm = \rho_{\pm,0}\cos\left(\frac{\Omega_0}{2}t\right)\sin\left(\omega_\pm t\right) \quad , \tag{4.26}$$

where Ω_0 is the Rabi frequency

$$\Omega_0 = \frac{qE_0}{2m\sqrt{\omega_z\omega_\pm}} \quad , \tag{4.27}$$

which depends on the strength E_0 of the coupling field. We can use this energy exchange between the two modes to cool the radial mode. For further discussion we focus on the coupling of the modified cyclotron mode to the axial mode with respective quantum numbers n_+ and n_z. For cooling we use a sideband at the difference of the two frequencies. An absorption of an rf-photon with energy $\hbar\omega_{\mathrm{rf}} = \hbar(\omega_+ - \omega_z)$ leads either to $(n_z - 1, n_+ + 1)$ or $(n_z + 1, n_+ - 1)$. For long time scales of the coupling field, the equilibrium state will be reached, which is defined by equal quantum numbers $n_z = n_+$. Since the axial mode is in contact to its detection system the average axial quantum state is defined by the temperature of the tank circuit. Accordingly, the temperature of the modified cyclotron mode is given by

$$T_+ = \frac{\omega_+}{\omega_z}T_z \quad . \tag{4.28}$$

For a sideband of frequency $\hbar\omega_{\mathrm{rf}} = \hbar(\omega_z + \omega_+)$ an absorption of an rf photon leads to $(n_z + 1, n_+ + 1)$. Thus, the energy of both modes increases in the presence of the coupling field.
The same argumentation holds for the magnetron mode. However, due to the negative

energy of E_- the two sidebands change role compared to the modified cyclotron mode. For a sideband with frequency $\omega_{\mathrm{rf}} = \omega_z + \omega_-$ the equilibrium state is given by

$$T_- = \frac{\omega_-}{\omega_z} T_z \quad . \tag{4.29}$$

Due to the frequency scaling of Eq. (4.28) and (4.29) the final temperature of the magnetron mode is below the temperature of the cryogenic environment and it is higher for the modified cyclotron mode. Moreover, after a sideband coupling of both radial modes to the axial mode, the modified cyclotron temperature is a factor of ω_+/ω_- higher than the temperature of the magnetron mode. This means that the radii of both radial modes are equal after coupling to the axial detection system (see Eq. (2.13)). For further cooling of the modified cyclotron mode, we utilize a dedicated detection system which is connected to the precision trap and provides resistive cooling to the ambient cryogenic temperature. As we will see in chapter 8 this temperature reduction is crucial for the detection of spin transitions in the analysis trap.
In order to determine the radial frequency information by the application of sideband coupling we can rewrite Eq. (4.25)

$$z(t) = \frac{1}{2} z_0 \left[\sin\left(\left(\omega_z + \frac{\Omega_0}{2} \right) t \right) + \sin\left(\left(\omega_z - \frac{\Omega_0}{2} \right) t \right) \right] \quad . \tag{4.30}$$

Thus, in **frequency domain** the axial dip in the power spectrum splits into two dips ω_l, ω_r with a separation equal to the rabi frequency Ω_0

$$\omega_l = \omega_z - \frac{\Omega_0}{2} \tag{4.31}$$

$$\omega_r = \omega_z + \frac{\Omega_0}{2} \quad . \tag{4.32}$$

The radial frequency is obtained by a measurement of the axial frequency ω_z and the double-dip frequencies $\omega_{l,r}$ by

$$\omega_+ = \omega_l + \omega_r - \omega_z + \omega_{\mathrm{rf}} \tag{4.33}$$

$$\omega_- = -\omega_l - \omega_r + \omega_z + \omega_{\mathrm{rf}}, \quad , \tag{4.34}$$

where the first equation corresponds to a resonant coupling of the modified cyclotron mode $\omega_{\mathrm{rf}} = \omega_+ - \omega_z$ and the second equation corresponds to a resonant coupling of the magnetron mode $\omega_{\mathrm{rf}} = \omega_z + \omega_-$. For a small detuning δ of the coupling field $\omega_{\mathrm{rf}} = \delta + \omega_z \pm \omega_\mp$ the Rabi frequency is given by $\Omega = \sqrt{\Omega_0^2 + \delta^2}$. Additionally, the double-dip frequencies are shifted

$$\omega_l = \omega_z - \frac{1}{2}(\delta + \Omega) \tag{4.35}$$

$$\omega_r = \omega_z + \frac{1}{2}(\delta + \Omega) \quad . \tag{4.36}$$

The two radial frequencies can be calculated by Eq. (4.33) and (4.34) despite a detuned coupling field. Thus, the double-dip technique is a very robust method to determine the radial eigenfrequencies.

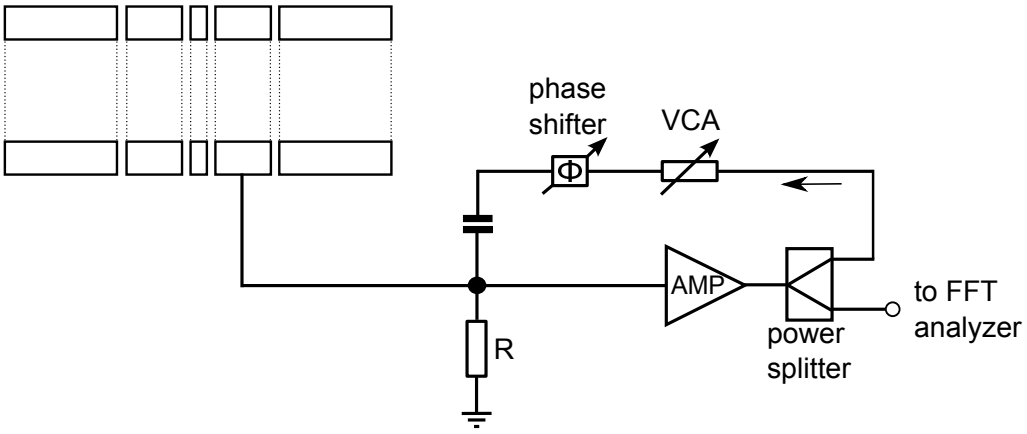

Figure 4.5: Schematic of the feedback loop. The LC-circuit with resistance R is attached to one correction electrode. Part of the amplified signal is capacitively fed back to the tank circuit. The signal is phase shifted by Φ. The gain G_{FB} is controlled by the amplifier and a voltage regulated attenuator VCA.

4.5 Feedback - control of the ion temperature

The concept of active electronic feedback [62, 63, 64, 65] is schematically shown in Fig. 4.5. The signal derived at the output of the amplifier is phase-shifted and fed back to the tank circuit. Since the induced voltage drop is proportional to the ion current we can write the additional force due to the feedback $F_{\mathrm{FB}} = m\gamma_i G_{\mathrm{FB}}\dot{\rho}_i$, where G_{FB} is the feedback gain. The equation of motion (Eq. (4.15)) is modified

$$\begin{aligned} \ddot{\rho}_i + \omega_i^2 \rho_i &= -\gamma_i \dot{\rho}_i - F_{\mathrm{FB}}/m_p \\ &= -\gamma_i \dot{\rho}_i - G_{\mathrm{FB}}\gamma_i \dot{\rho}_i \\ &= -\gamma_i \dot{\rho}_i (1 - G_{\mathrm{FB}}) \quad . \end{aligned} \tag{4.37}$$

Thus, feedback can be utilized to enhance or suppress the damping term depending on the sign of G_{FB}. The sign of G_{FB} can be controlled by adjusting the phase of the feedback signal. For a phase shift of $\Phi = 0°$ the feedback adds constructively resulting in a stronger damping ($G_{\mathrm{FB}} < 0$, positive feedback). For $\Phi = 180°$ the particle is less damped ($G_{\mathrm{FB}} > 0$, negative feedback). The effect of active feedback can be modeled by an effective resistance R_{eff} seen by the particle

$$R_{\mathrm{eff}} = R_{\mathrm{sys}}(1 - G_{\mathrm{FB}}) \quad . \tag{4.38}$$

The ratio of effective parallel resistance R_{eff} and particle temperature T_{eff} is a fluctuation-dissipation invariant, and thus $T_{\mathrm{eff}} = T(1 \pm G_{\mathrm{FB}})$, where T is the temperature of the detection system without feedback ($G_{FB} = 0$).
Active electronic feedback is commonly used in our experiment for different purposes

- **negative feedback** is utilized to cool the eigenmotions below the physical temperature of the detection systems. In the magnetic bottle the linewidth of the Larmor

resonance as well as the modified cyclotron resonance scale proportional to the particle temperature (see section 3.2). Thus, a reduction of the axial temperature by application of negative feedback to the axial detection system allowed us to reduce the linewidth, which increases the precision of the frequency determination (see chapter 8). Furthermore, we apply negative feedback to the modified cyclotron detection system to reduce axial frequency fluctuations in the analysis trap which scale with T_+ (see chapter 8).

- **positive feedback** is utilized to increase the effective resistance of the tank circuit. Thus, the linewidth of the noise-dip can be increased. Using positive feedback for to the detection system for the modified cyclotron motion allowed us to resolve the cyclotron noise-dip of a single proton (see chapter 7).

4.6 Transient recorder - a real-time data acquisition system

In this section a tool for the continuous monitoring of motional frequencies is presented. With the so-called transient recorder the real time signal of a thermalized ion can be recorded. Thus, the FFT-analysis can be performed after data taking for the same data set for various parameters. The advantages of the transient recorder analysis for systematic studies as well as detector optimization are discussed in this section.
In chapter 3 the frequency fluctuation Ξ was introduced, which is defined as the standard deviation of the difference of two consecutive frequency measurements $\alpha = \nu(t) - \nu(t+T)$ separated by the time T. We can distinguish between three different types of background fluctuations

- Ξ_{dec} describes fluctuations which decrease with increasing averaging time T. This is for example Ξ_{FFT}, which is given by the uncertainty of the frequency determination with the dip technique as discussed in section 4.3.

- Ξ_{inc} describes fluctuations which increase with increasing averaging time T. This is for example Ξ_{radial} which is given by energy fluctuations in the radial modes in the magnetic bottle as discussed in section 3.5. These fluctuations can be described by a random walk.

- Ξ_{const} describes fluctuations which are constant for increasing averaging time T. For example Ξ_{V}, which is given by voltage fluctuations. Since the voltage fluctuates around a mean value with a less pronounced drift component, Ξ_{V} has a negligible time dependence compared to Ξ_{radial}.

A measurement of $\Xi^2_{\mathrm{tot}} = \Xi^2_{\mathrm{inc}} + \Xi^2_{\mathrm{dec}} + \Xi^2_{\mathrm{const}}$ as a function of the averaging time T (shown in Fig. 4.6) provides useful information of the time scaling of Ξ_{tot} and enables the investigation of the source for the frequency fluctuation. Since the error of Ξ_{tot} scales $\propto 1/\sqrt{2N}$ a large number of measurements N is required for a specific averaging time T. About six hours of data taking are needed for each $\Xi_{\mathrm{tot}}(T)$. With the transient recorder, a dataset of

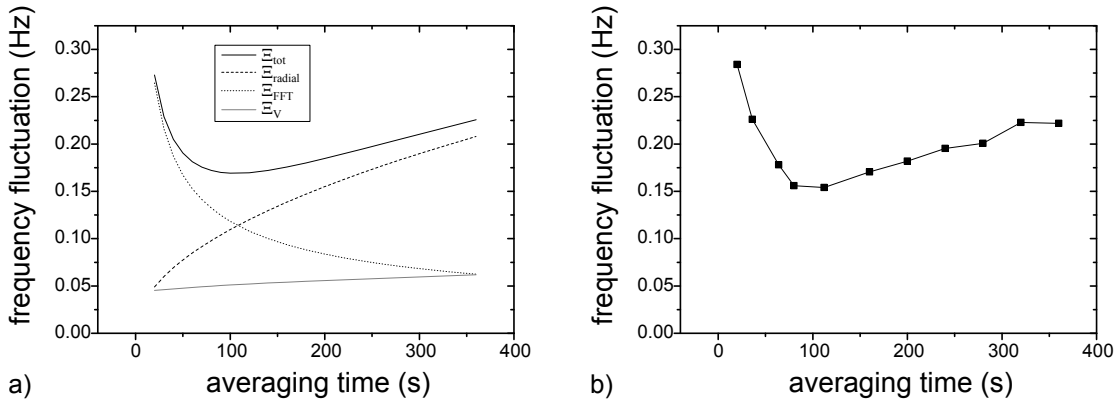

Figure 4.6: a) Calculated frequency fluctuation Ξ_{tot} (solid black line) as a function of the averaging time T. The dotted curve corresponds to the frequency uncertainty Ξ_{FFT} of the frequency measurement which decreases with T. The contribution of voltage fluctuations Ξ_{V} with a very low T-dependence is shown in grey. The dashed curve corresponds to a phenomena in the magnetic bottle field of the analysis trap: A random walk of the radial energy causes an axial frequency fluctuation Ξ_{radial} which increases with T. b) Experimental data of the axial frequency stability in the analysis trap, which was recorded and analysed with the transient recorder.

about six hours can be evaluated for about twelve different averaging times in one night. Thus a plot of Ξ_{tot} as a function of T can be obtained approximately four times faster than with the convential FFT-analyzer. Moreover, during a convential measurement of $\Xi_{\mathrm{tot}}(T)$ the different contributions and the total magnitude of Ξ_{tot} would vary which would reduce the significance of the measurement. Since the analysis with the transient recorder is based on the same dataset, the corresponding sources for the frequency fluctuations are exactly the same.
The optimal averaging time T_{opt} can be easily obtained from such an analysis which is given by the minimum of $\Xi_{\mathrm{tot}}(T)$.
Moreover, we can vary additional FFT-parameters as for example the resolution to obtain the lowest Ξ_{FFT}. Once more - since the analysis is based on the same data, we can assign changes of $\Xi_{\mathrm{tot}}(T)$ to the variation of the FFT-parameters only. Thus, we can optimize our FFT-parameters very effectively.

The transient recorder can be separated into the data taking and data analysing part. The data taking is accomplished with a standard soundcard in a personal computer. The data analysis is accomplished with a program written in *Labview*. In the first part the FFT is performed. The frequency determination is conducted afterwards. Different parameters are varied automatically to create a plot as in Fig. 4.6.

	Axial AT	Axial PT	Cyc PT	Axial AT&PT (old)
L (mH)	1.91	1.2	0.00168	1.45
ν_{LC} (MHz)	0.742	0.785	28.97	0.68
Q	9500	5000	1250	5800
R_{sys} (MΩ)	85	63	0.382	36
D_i (mm)	13.9	7.7	15.5	4.5 and 7.7
$\Delta\nu_i$ (Hz)	1.1	1.2	0.004	4.3 and 1.5
SNR (dB)	25	12	18	16

Table 4.1: The parameters for the three detection systems are listed. L is the inductance of the coil, ν_{LC} is the resonance frequency, Q is the quality factor, R_{sys} is the effective parallel resistance, D_i is the effective electrode distance and SNR gives the signal-to-noise ratio of the resonator as defined by Eq. (4.24)

4.7 Experimental realization of the detection systems

Our experiment utilizes three different detection systems:

- A detection system for the axial mode which is connected to one endcap of the analysis trap. (Axial AT)
- A detection system for the axial mode which is connected to a correction electrode of the precision trap. (Axial PT)
- A detection system for the modified cyclotron mode which is connected to one half of a split correction electrode in the precision trap. (Cyc PT)

The parameters for the detection systems are listed in Tab. 4.1. The last column gives the parameters of the former axial detection system [45] which was connected to both traps. The benefit of two separate axial detection systems is the reduction of the trap capacitance in parallel to each tank circuit. Thus, higher inductances L and consequently higher quality factors could be achieved. However, due to space restrictions toroidal coils had to be employed rather than the single solenoid before which are more complex to design and construct. The design, assembly and optimization of these tank circuits was part of the PhD thesis of Andreas Mooser [57]. He performed elaborate investigations of loss mechanisms in superconducting tank circuits. This allowed to build separate axial tank circuits with very high quality factors. The design of the cyclotron detection system was accomplished by Stefan Ulmer in the course of his PhD thesis [45]. Summarizing, highly sensitive detection systems are available to detect the motion of a single proton in our trap.

Chapter 5

Experimental setup

The Penning traps and the detection systems compose the heart of our experiment. They form the basis for the determination of the g-factor of a single proton and hence have been discussed in detail in the previous chapters 2, 3 and 4. However, a high-precision measurement of the g-factor also requires for a cryogenic environment to obtain small motional amplitudes of the proton, a stable magnetic field and low-noise electronics. The complete experimental setup, which contains these additional components is briefly described in this chapter. For further details see also [46] and [66].
In the first section 5.1, the liquid helium dewar which provides the cryogenic temperatures and the superconducting magnet are presented. The Penning traps are housed in a vacuum chamber (section 5.2) which is located in the homogeneous field of the superconducting magnet. The detection systems are placed as close to the traps as possible (section 5.3). The electrical connections between the electronics located in the cryogenic region and room temperature electronics are described in section 5.4. The performance of the high-precision voltage source, which provides the voltages for the electrostatic trapping potential is discussed in section 5.5. Frequency synthesizers, spectrum analyzers and voltage supplies are used to manipulate, detect and control the motion of the proton. In section 5.6, computer programs written in *Labview* are presented, which automate these processes and analyse the acquired data.
A complete revision of the whole experiment led to a lot of changes. A summary of all changes in comparison to the description of the former apparatus given in [45, 46] is presented in section 5.7.

5.1 Apparatus

The experimental setup is shown in Fig. 5.1. The Penning traps are located in the homogeneous region of a superconducting magnet with field strength $B_0 = 1.899\,\mathrm{T}$ and with an 88 mm diameter horizontal warm bore. A liquid helium and liquid nitrogen cryostat located on top of a CF200 double-cross vacuum chamber provides the cryogenic temperatures for the traps. The cryostat replaced the former pulse tube cooler due to vibration

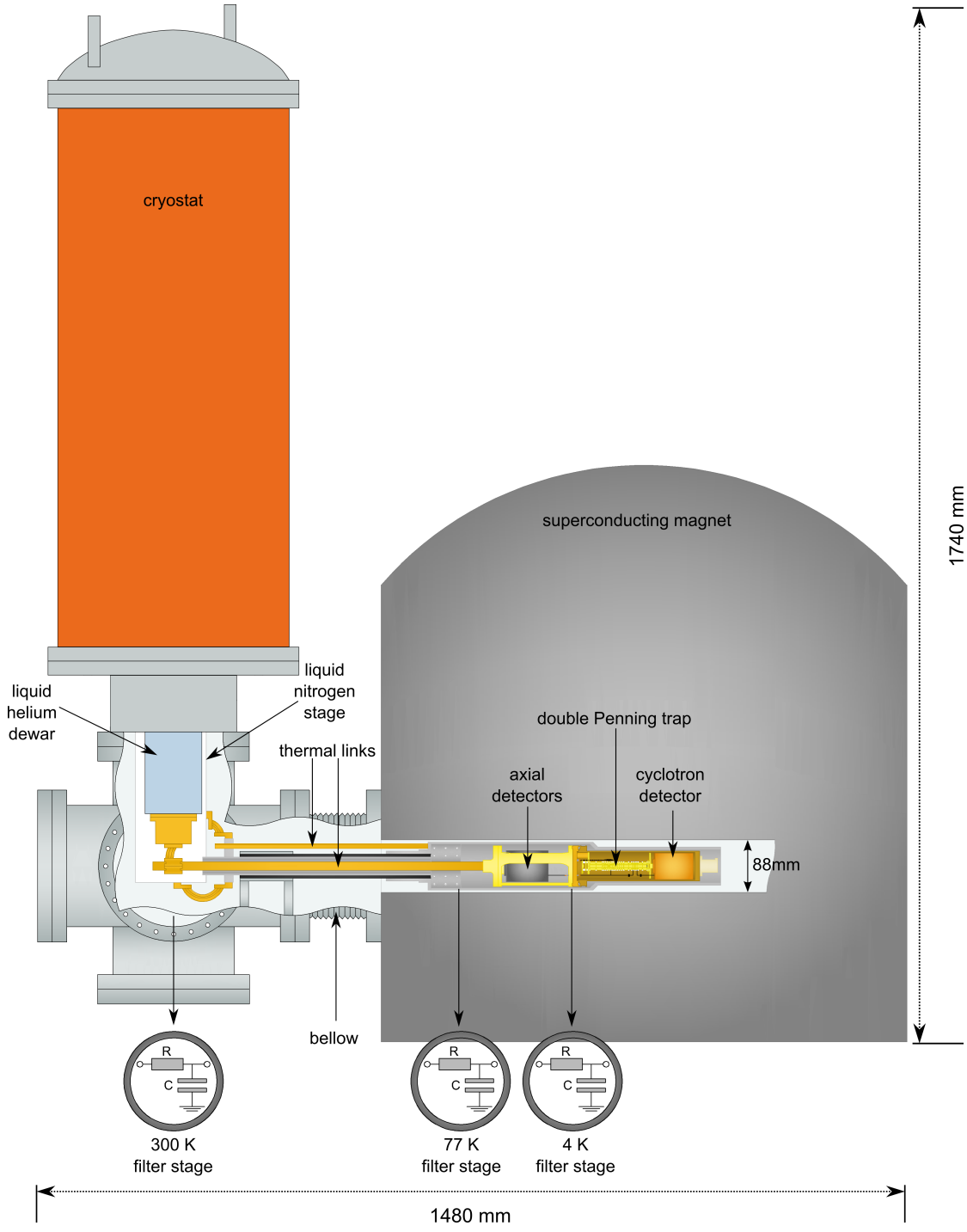

Figure 5.1: Schematic diagram of the experimental setup adopted from [47]. The double-Penning trap setup is located in the homogeneous region of the superconducting magnet. A liquid cryostat provides the cryogenic temperatures. The trap chamber and the superconducting detection systems are connected to the cryostat by a high-purity copper rod. The cryostat is mounted on top of a CF-200 double-cross, which is connected to the magnet by a flexible bellow.

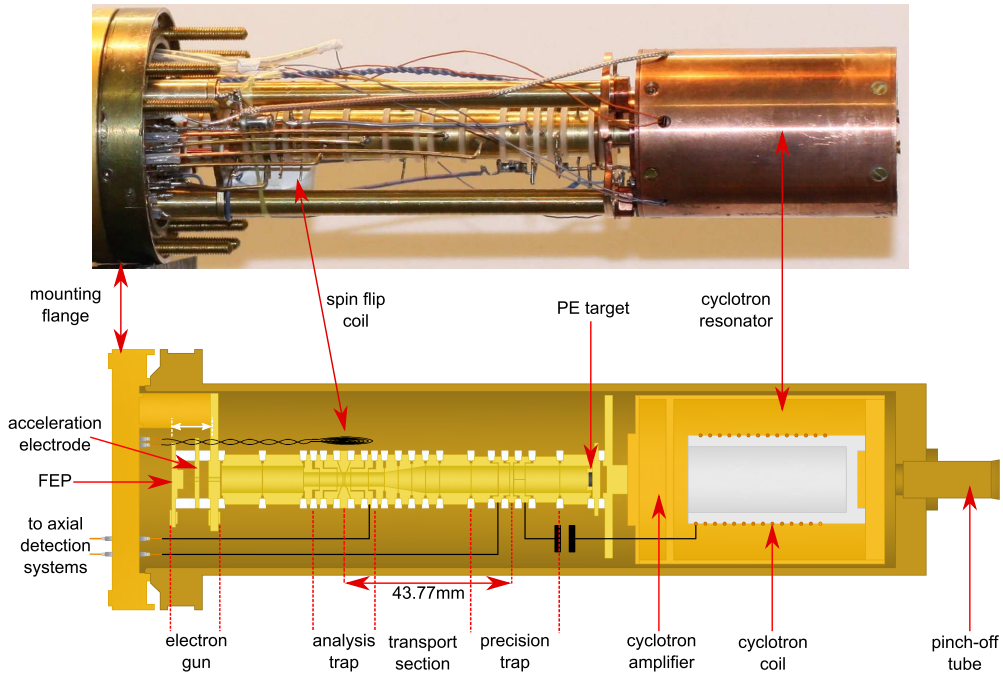

Figure 5.2: Top: Photograph of the electrode stack and the cyclotron detection system. Bottom: Cross-sectional view of the trap chamber adopted from [47]. The position of the analysis trap is shifted towards the precision trap compared to the photograph since the new transport section is shorter [45].

issues (see section 5.7). The double-cross is mounted on an adjustable table and is connected by a bellow to the bore of the magnet. Thus, it is possible to vary the position of the traps within all three dimensions. A pressure of $5 \cdot 10^{-8}$ mbar is achieved for the insulation vacuum of the double-cross and the magnet bore. The trapping region is connected to the cold finger of the helium dewar by a high-purity copper rod surrounded by thermal heat shields which are connected to the liquid nitrogen reservoir. The reservoirs have a capacity of 35 l liquid helium and 35 l liquid nitrogen, respectively. The hold time for liquid helium is five days and liquid nitrogen has to be filled every three days. A cool down of the experiment from room temperature to 4.2 K takes about 24 hours and 80 l of liquid helium. We achieved a temperature of $T = 4.3\,\mathrm{K}$ at the trapping region and $T = 80\,\mathrm{K}$ at the heat shields mounted around the traps. Details of the cryo-mechanical design can be found in [67]. The design of the new cryostat is discussed in [57].
The whole experiment is surrounded by a wooden box which is temperature stabilized. As a result, the daily peak-to-peak fluctuations of the temperature of the double-cross could be reduced by a factor of 40 to a level of about 50 mK [57].

5.2 Trap chamber

The double-trap setup shown in Fig. 5.2 is placed in a vacuum chamber made of oxygen-free electrolytic (OFE) copper. The indium sealed flange on one side of the chamber contains

all soft-soldered electronic feedthroughs to the chamber. The tube on the opposite side is used to evacuate the chamber at room temperature to a pressure better than $1 \cdot 10^{-6}$ mbar. Having achieved this pressure, the chamber is closed by a pinch-off tool which creates a permanent cold-welded seal. After cooling down, the pressure inside the trap chamber is reduced by orders of magnitude due to cryo-pumping. As a result a vacuum better than 10^{-16} mbar is achieved in such a system [30]. Thus, protons can be stored for arbitrarily long times and collisions with rest gas atoms can be neglected.
The closed setup requires the in-trap production of protons. To this end, the trap stack is extended by an electron beam source on one side and a target plate on the opposite side as shown in Fig. 5.2. Electrons are emitted from the field emission point (FEP) for a voltage of about 1 kV on the acceleration electrode relative to ground. The energy of the electrons is defined by a negative voltage of the order of 50 V applied to the FEP. The emitted electrons follow the magnetic field lines and sputter atoms and molecules from the surface of the polyethylene target which are subsequently ionized in the potential of the precision trap. Electron currents of about 10 nA for about 2 s are sufficient to produce protons (see chapter 6).
The electron source is fixed to a holding plate. A second holding plate on top of the target is pressed to the first by three copper rods. This centers and compresses the electrode stack. The rf-field to drive spin transitions is generated by disc coils which consist of about 6 concentric windings fixed to a teflon-holder [68]. The coils are mounted to the copper rods, next to the ring electrode of each trap.
All trap electrodes are made of OFE copper which are gold plated to avoid oxidation. In case of the analysis trap special care has to be taken in order to obtain the calculated potential. First, the mechanical tolerance was decreased to 3 μm since a smaller trap size implies a higher sensitivity on machining errors. Second, the surface has to be polished since the grooves of the machining tool prevent a uniform gold layer. In order to prevent deviations of the electrode dimensions a very gentle polishing technique using Q-tips is applied [46]. The resulting surface is electrolytically gold-plated with an average thickness of about 5 μm. A silver barrier-coating of 15 μm prevents diffusion of the gold layer into the copper. For the analysis trap electrodes, a nickel barrier-coating had been employed, since nickel is a more suited barrier and the resulting magnetic inhomogeneity is negligible. Sapphire rings are used as spacers between the electrodes to guarantee electrical isolation and assure thermal conductivity.

5.3 Detection systems

Three detection systems are available for the determination of the g-factor:

- The detection system for the modified cyclotron frequency consists of a helical resonator and a low-noise amplifier. The amplifier is mounted on top of the resonator. The solenoid and its cylindrical housing are made of oxygen-free electrolytic (OFE) copper. Superconducting materials have no benefit for this detection system since rf-

losses in superconductors are significant in this frequency regime [55]. The detection system is located inside the trap chamber to avoid the additional capacitance and loss resistance of the trap chamber feedthrough. The parameters of the cryogenic part of the cyclotron detection system are given in Tab. 4.1. The signal is guided to room temperature where it is further amplified by a low-noise *Minicircuits ZFL-500LN* amplifier. For FFT-analysis the signal is converted to audio frequencies by a *Minicircuits ZAD-6+* mixer and is analysed with *Stanford Research SR780* FFT spectrum-analyzer.

- The two axial detection systems for each trap are located outside the trap chamber since the loss mechanisms in the feedthroughs are of less importance at their operating frequencies. Moreover, by utilizing special feedthroughs made of sapphire, the corresponding losses could be further reduced. The axial detection systems consist of two toroidal coils in separate cylindrical housings. Here, superconducting materials of niobium-titanium are used for the wire and the housing to obtain high quality factors. The two low-noise amplifiers are placed right next to the resonators to avoid additional parasitic capacitances. Tab. 4.1 summarizes the parameters of the cryogenic section of the axial detection systems. A second amplification stage at room temperature is followed by a single-sideband mixer (both *Stahl Electronics*). Down-conversion of a signal at frequency ν_{rf} to ν_{IF} with a double-sideband mixer at frequency $\nu_{\mathrm{LO}} = \nu_{\mathrm{rf}} - \nu_{\mathrm{IF}}$ has the following drawback [69]: The signal at the lower sideband $\nu_{\mathrm{image}} = \nu_{\mathrm{LO}} - \nu_{\mathrm{IF}}$ is also converted to ν_{IF}. Thus, noise at the lower sideband, which is caused by our amplifiers, would decrease the SNR of the detection systems. Thus, a single-sideband mixer from *Stahl Electronics* is utilized, which suppresses the lower sideband by about 60 dB. The down-converted spectrum at ν_{IF} is analyzed with a a *Stanford Research SR780* FFT spectrum-analyzer. By comparison of this spectrum with the original spectrum at ν_{rf}, which was analyzed with a *R&S FSP13* spectrum-analyzer, we observed no degradation of the SNR.

5.4 Wiring and filtering

This section gives an overview of all electronic connections in our apparatus. The wires represent thermal bridges between room temperature and the cryogenic region, which lowers the hold time of our cryostat and increases the temperature of our detection systems and the traps. In order to reduce the corresponding heat load, materials of low thermal conductivity and small diameters have to be chosen. However, the focus of this summary is not the heat input of the wires but the possible introduction of noise to our trap electrodes, especially to those of the analysis trap. We assume that a radial field drives the modified cyclotron mode. Thus, the filtering concept is presented in this section, motivating the changes given in the section 5.7. A detailed overview of the wiring also covering the respective thermal input is given in [46].
We can distinguish between three different groups of connections: DC, RF and HV (high

voltage):

- The **DC**-lines are used for biasing of the trap electrodes and the amplifiers. Three low-pass filter stages at 300 K, 77 K and 4 K are implemented. The position of the stages is indicated in Fig. 5.1. Each filter consists of two 820 kΩ resistors in parallel and a 2.7 nF capacitor connected to ground. The only unfiltered DC-lines going down to 4 K are the drain supplies for the cryogenic amplifiers since they require a current to flow. Dissipation in the resistor of a DC-filter would cause an additional heat load. However, the corresponding detection systems attached to the precision trap should be of no concern since they are far from the analysis trap. For the axial detection system attached to the analysis trap we reduced a possible impact on the proton by connecting the tank circuit to the endcap instead of the correction electrode (see section 5.7).

- The **RF**-lines are used for excitation, detection and feedback. All excitation lines are attenuated by 20dB at room temperature. The signals are guided to the trap and the spin flip coils by shielded twisted pair lines. Each excitation line which is connected to trap electrodes passes a voltage divider at 4 K consisting of a 4.7 pF capacitor in series and a 15 pF capacitator connected to ground.

- One unfiltered **HV**-line is needed to bias the acceleration electrode of the electron gun. Shielding of the connection is realized by guiding the corresponding cable inside a metal tube which is anchored to ground. Additional shielding of the analysis trap from possible noise of the acceleration electrode is realised by the holding plate which is placed in between and is set on ground potential.

5.5 DC supply

The trapping potentials are generated by a high-precision voltage source *UM1-14 LN* from *Stahl Electronics*. It features ten fast-channels with 16-bit resolution providing a voltage of 0 to −14 V. These channels are used for biasing the transport electrodes and the endcaps of both traps. The six 24-bit precision-channels are used for the correction electrodes and the ring electrode of both traps. The voltage range is 0 V to −14 V for the precision trap and 0 V to −4 V for the analysis trap.
As discussed in section 3.1 the axial frequency in the analysis trap has to be stable enough to detect single spin transitions. For a spin flip measurement, the endcaps are set on ground potential. Thus the potential depth is given by the voltage applied to the ring electrode. A spin flip measurement consists of at least two axial frequency measurements and a spin flip drive in between, which overall takes approximately $T = 180\,\mathrm{s}$. This means, that the frequency fluctuations due to voltage fluctuations should be less than $\Delta\nu_{z,\mathrm{SF}}/\nu_z = 2 \cdot 10^{-7}$ for the period T.

The relative voltage stability of the *UM1-14LN* was measured with an 8.5-digit *Fluke*

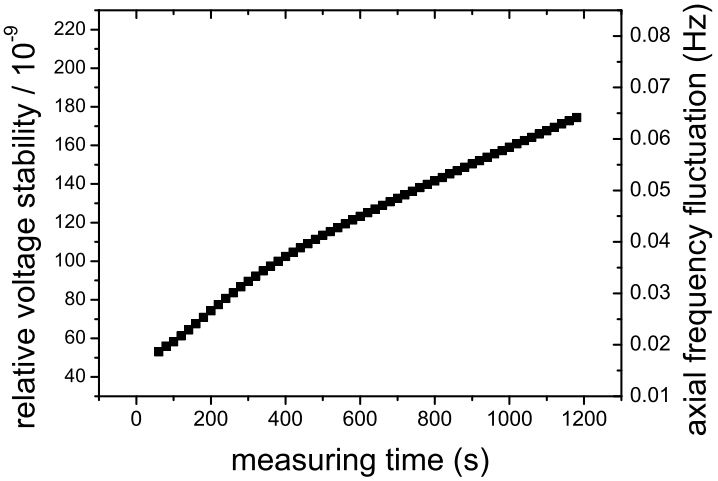

Figure 5.3: Relative voltage stability of the *UM1-14 LN* voltage supply as a function of the measuring time. The right axis shows the expected equivalent frequency fluctuations of the axial frequency.

8508A multimeter taking one data point every 20 s. The relative uncertainty of the multimeter in the 2 V-range for a confidence level of 95 % (for a period of 24 hours and temperature variations of maximum ±1 K) is given by 0.2 ppm of the range plus 0.5 ppm of the reading [70]. For a measurement of 1 V, this corresponds to an absolute uncertainty of 900 nV. However, no information on the short-term stability is given in the datasheet. Thus, the presented measurement of the voltage stability of the *UM1-14 LN* can only be interpreted as an upper limit of the voltage fluctuations of the voltage supply since the measurement noise or a possible drift of the multimeter could not be determined.
The performance of one precision channel of the *UM1-14LN* for the biasing of the analysis trap is shown in Fig. 5.3. The equivalent frequency fluctuations are below one third of a spin transition for a period of $T = 10$ min. Thus, voltage stability is no obstacle for spin state analysis. In order to further reduce the short term fluctuations, the voltage source is surrounded by a massive copper housing. Thus, fluctuations of the ambient temperature are smoothed and averaged. The long term temperature drifts are suppressed by the temperature stabilization of the whole apparatus. The measured fluctuations of the axial frequency of a single proton in the precision trap are even lower than expected from the measured voltage fluctuations (see section 7.1.3).

5.6 Control program

Automation is one of the most important points for a successful data acquisition and analysis. Obtaining an information just by pushing a button rather than by manual

read-out and analysis by hand is crucial for building up complex routines like a g-factor measurement as described in section 3.4. However, setting up this automation is not only a very time consuming exercise but also a crucial part since any mistake can cause loss of the proton and systematic uncertainties. It became one of my main priorities within this thesis. We chose Labview 8.2. as programming environment since it is the standard language for device control and data acquisition. Control programs for nearly every commercial device with a suited interface (USB, LAN, GPIB or RS-232) are provided by the corresponding manufacturer. Our experiment incorporates several frequency synthesizers, voltage sources, a spectrum- and an FFT-analyzer for particle control and detection. For environmental monitoring and controlling, temperature- and pressure-monitors as well as appropriate control systems are utilized. All these instruments have to be operated simultaneously and in combination. Our main focus for automation was set on modularity giving a toolbox of little self-explanatory programs to control and manipulate devices and to build more complex modules. Thus, any user can set up his own program in a very short time without worrying about the details of each sub-program. Since Labview is a very intuitive programing language it is even suited for unexperienced programmers. We also thought of programming our own script language as in [71] but discarded this possibility since it would mean a huge amount of work for implementation and also for maintenance. Still, I spent a lot of time setting up this toolbox and wiring all these little Labview programs. The everyday experimental routines were combined to a main control program shown in Fig. 5.4 which was also frequently modified and extended during my PhD thesis to meet the actual requirements. Up to now, 60 different routines were combined in this master program. Simple routines as for example for excitation, transport, cooling of the proton and also more complex routines as for example for tuning-ratio optimization and asymmetry compensation are implemented. The data acquisition requires an appropriate organization of all collected spectra on our hard disk. We chose a chronological order which gives for a single spectrum a path like

```
Data{\}June{\}13062011{\}TuningRatio{\}
FFT_06_13_14_54_38_TR_0.863_VR_3.16_Avg_60s_Magnetron.lvm.
```

The filename is composed of a timestamp and the parameters of the corresponding routine. The timestamp (`FFT_m_d_H_M_S`) assures the uniqueness of a single measurement and facilitates the mapping of measurements to the documentation in the lab book. The set of parameters (`TR_0.863_VR_3.16_Avg_60s`) is chosen to cover the main aspects of the given routine. Special circumstances can be added manually as a text (`Magnetron`) to the filename.

However, data acquisition is only half of the story since automated routines create a lot of data. In the early days of the experiment in summer 2008 we took about 5.000 spectra in one month. At the end of my thesis this was increased to more than 100.000 per month. The increased complexity of the measurement tasks does not only require

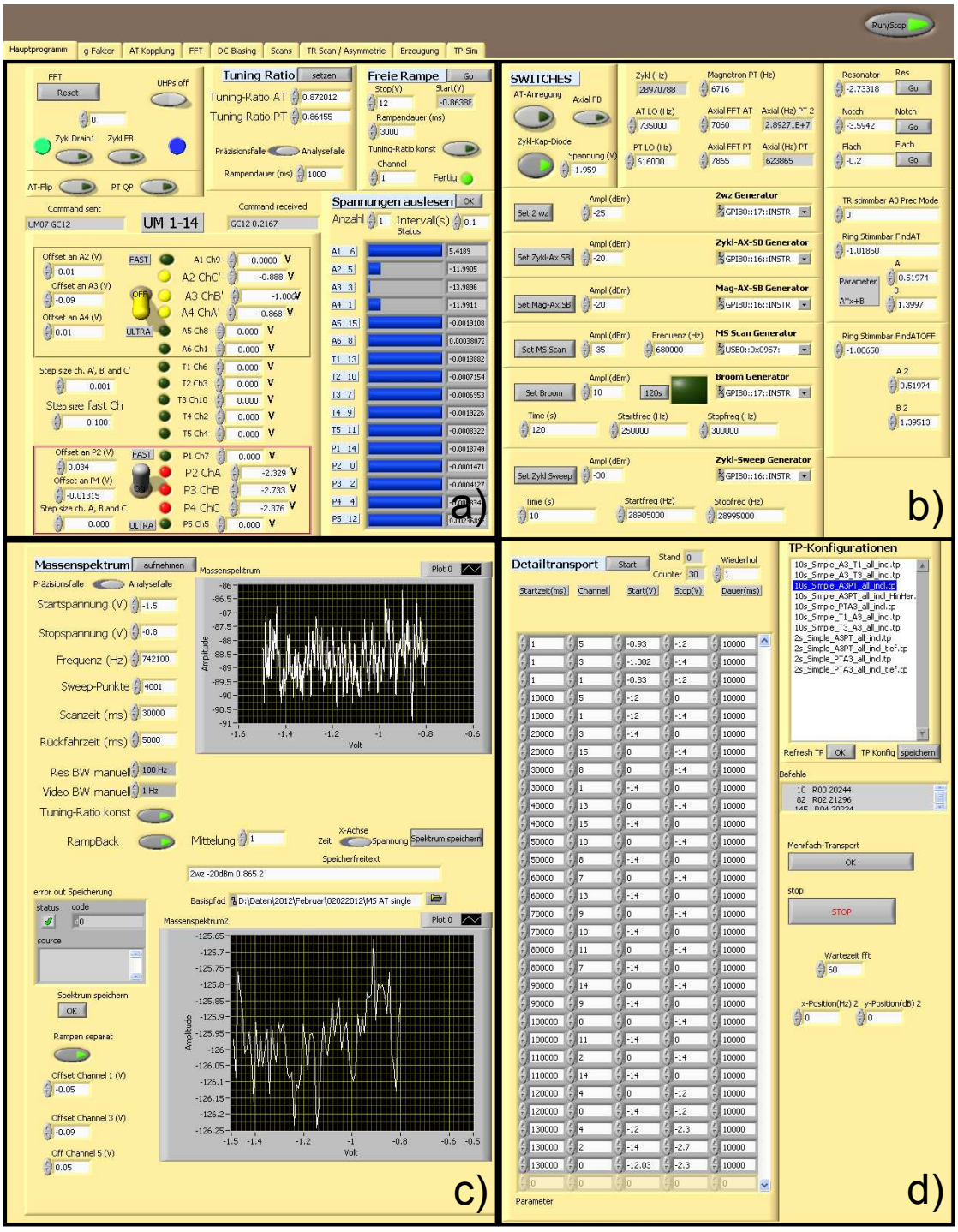

Figure 5.4: Screenshot of the proton control program. a) contains the control elements for the voltage supply of the trap electrodes. The control elements for particle excitation and sideband coupling are shown in b). The control and monitoring elements for mass-spectra are located in the lower left quarter c). The exchange of the proton between the two traps can be configured and executed with the control elements shown in d). In order to obtain a clear arrangement, the remaining tasks are placed on additional pages of the tab control.

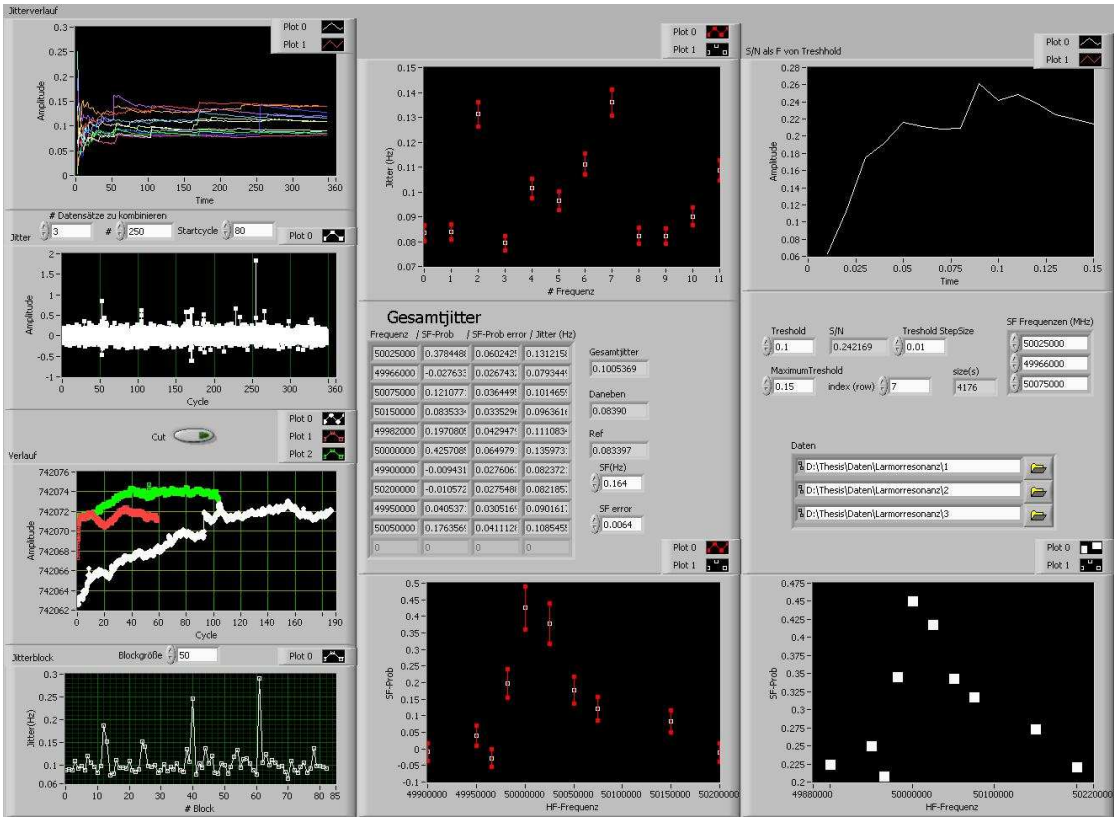

Figure 5.5: Screenshot of the Larmor resonance program. The program evaluates the differences of two subsequent axial frequency measurements as explained in section 3.5.1 and 3.5.2 to obtain a Larmor resonance curve. *Labview* offers the possibility to arrange several plots on the front panel for diagnostics and data comparison. Combinations of different data sets can be easily evaluated and compared.

a simple way to set up a program but also an easy way to analyse the data. A simple tuning ratio optimization consists of 10 spectra only differing by the voltage applied to the correction electrodes. The corresponding data could still be acquired and analysed manually. But a Larmor resonance curve consists of about 40.000 measurements with several intermediate tasks like sideband cooling, spin driving and many more steps. The analysis of this data can also be accomplished with Labview programs since it offers the great possibility to monitor data in a very well-arranged way. Complex data analysis as fitting routines can be integrated as external scripts. Accordingly, also difficult analysing can be executed within a Labview program. In Fig. 5.5, our analysis program for the Larmor frequency measurement is shown. It evaluates the spin flip attempts for different driving frequencies for the statistical- and the threshold-method presented in section 3.5.1 and 3.5.2, respectively.

5.7 Technical improvements

Our main motivation for a complete revision of our experimental setup was the reduction of axial frequency fluctuations in the analysis trap. These fluctuations precluded a spin state analysis as needed for the application of the double-trap method described in section 3.4. We tackled this problem from two sides:
On one hand we reduced the time needed to perform an axial frequency measurement. This means that we decreased the frequency uncertainty Ξ_{FFT} for a given averaging time (see Fig. 4.6). To this end, new axial detection systems were implemented which have been designed in the course of the PhD thesis of A. Mooser [57].
On the other hand we minimized the sources of the frequency fluctuations. We observed correlations of the frequency instabilities with the radial mode energies (see chapter 8). Based on the scaling of this effect, we concluded that background noise was responsible for the frequency fluctuations Ξ_{radial}. Thus, we tried to remove or at least reduce any possible noise sources:

- For all DC-connections of the analysis trap electrodes, the capacitors of the 4 K filter-stage were increased by a factor of ten.
- The voltage divider of the dipole-excitation line of the analysis trap located at 4 K was increased to 3.3 pF versus 18 pF to ground.
- The quadrupole excitation, which had been connected to a split electrode was completely removed. Thus, any noise introduced by the quadrupole-excitation-line is eliminated. Alternatively, we can couple the radial modes to the axial modes by application of a suited rf-field to the spin flip coil. In order to create a comparable field at the trap center, we have to increase the signal of the frequency synthesizer by approximately 30 dB.
- Although the axial resonator can be considered as a perfect short at the frequencies of the radial modes, we moved the axial detection from the correction electrode to the endcap. This results in an increased effective electrode distance for the radial mode. Thus, a possible noise source has less impact on the proton.

The achieved frequency stability (see chapter 8) clearly indicates that at least one of the listed changes was an improvement. However, we did not evaluate each of the steps separately since this would have taken too much time but implemented all simultaneously. Thus, we cannot judge which of the changes was the most significant.

A second motivation for an alteration of the setup were the vibrations of the puls tube cooler [72]. These precluded a high-precision measurement of the free cyclotron frequency in the precision trap - an essential ingredient of the g-factor measurement. Thus, the puls tube cooler was replaced by a liquid cryostat.

Chapter 6

Production of single protons and their transport

We produce protons by the bombardment of a polyethylene target with electrons from a field emission point as described in section 6.1. However, not only protons are produced by the electron beam but all kind of (low-charged) ions which have to be removed in the following. To this end different cleaning techniques described in section 6.2 are applied. Further reduction of the number of protons to a single proton is presented in section 6.3. The last part of this chapter deals with the transport of protons between the two traps.

6.1 Production of an ion cloud

By application of a positive voltage of about 1 kV to the acceleration electrode (see Fig. 5.2), an electron beam of about 10 nA is emitted. A negative voltage of 50 V applied to the field emission point sets the kinetic energy of the electrons. The electrons follow the magnetic field lines and hit the target plate at the opposite side of the electrode stack, which contains the target made of black polyethylene. Atoms and molecules are emitted which are subsequently ionized by the electron beam. Particles which are ionized in the trapping potential of the precision trap are consequently trapped. The electron gun is turned on for about 2 s to produce a cloud of ions.

6.2 Removing impurity ions

We can analyze the constituents of the ion cloud with a so-called mass spectrum. To this end, we apply a voltage ramp $V(t)$ to our ring and correction electrodes while maintaining a constant tuning-ratio. The axial frequency of different ion species will match the resonance frequency of the axial detection system at different points of the voltage ramp.

$$\nu_z(t) = \frac{1}{2\pi}\sqrt{\frac{2qc_2}{m}V(t)} \quad . \tag{6.1}$$

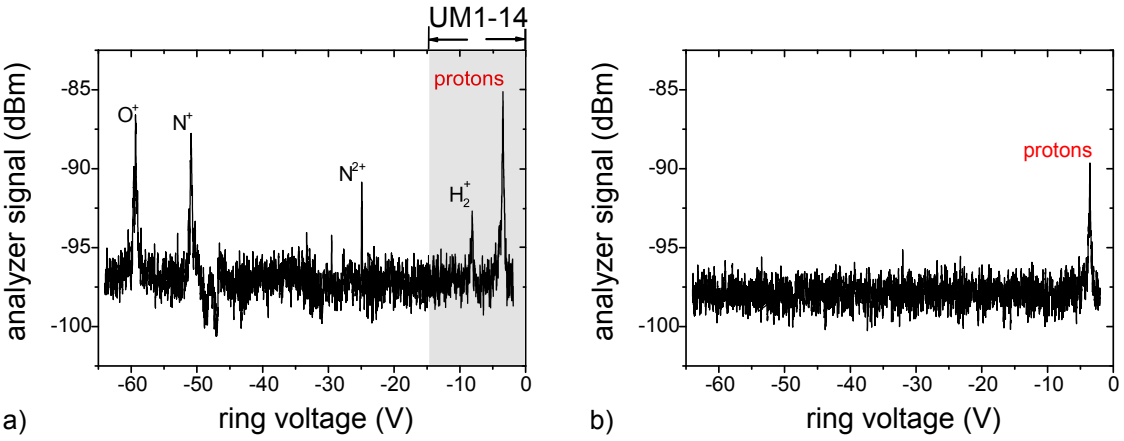

Figure 6.1: Mass spectra after trap loading a) and after cleaning b) [45]. Due to the limited voltage range of the voltage supply UM1-14 (shaded area), only H_2^+ and protons can be monitored routinely. Extension of the mass spectrum requires an exchange of the biasing supply. After the cleaning procedure explained in the text only protons are observed in the mass-spectrum b).

Since the axial motion of the ions is excited after production, a peak appears on top of the noise resonance as described in section 4.2. Monitoring the signal strength at the resonance frequency of the detection system as a function of ramping time or equivalently ramping voltage yields a mass-spectrum as shown in Fig. 6.1.
Removal of unwanted ion species is accomplished by excitation of the axial motion. To this end we utilize two different dipolar excitation drives in our precision trap:

1. All contaminants have a lower axial frequency than a proton for a given potential since a proton has the highest q/m. Thus, a low-frequency broadband noise drive realized by a stored wave inverse-fourier transform (SWIFT) [73] with a corner frequency of 500 kHz is applied to the dipole-excitation line of the trap. The axial motion of protons is additionally protected by a notch filter. Tuning the potential to obtain an axial frequency of $\nu_z \approx 700\,\text{kHz}$, a suppression of 60 dB of the axial driving field for protons is achieved as shown in Fig. 6.2.

2. Narrow RF-sweeps ($\Delta\nu = 10\,\text{kHz}$, $\Delta t = 120\,\text{s}$) are applied at the axial frequencies of unwanted ion species.

After each of these procedures the trapping potential is lowered to $V_0 = -0.1\,\text{V}$ to evaporate hot ions. A potential of $-7\,\text{V}$ is applied to the target electrode to attract the ions.
It is important to notice, that there is no known experimental routine which proves the purity of a proton cloud. A mass-spectrum is not suited since only a few ion species can be monitored and it is not sensitive to a single ion. Alternatively, we can search for modifications of experimental routines (e.g. a cyclotron cooling curve) which can be assigned to the presence of contaminants. However, not observing such a modification does not automatically indicate a clean trap. We chose the duration and the amplitude of the

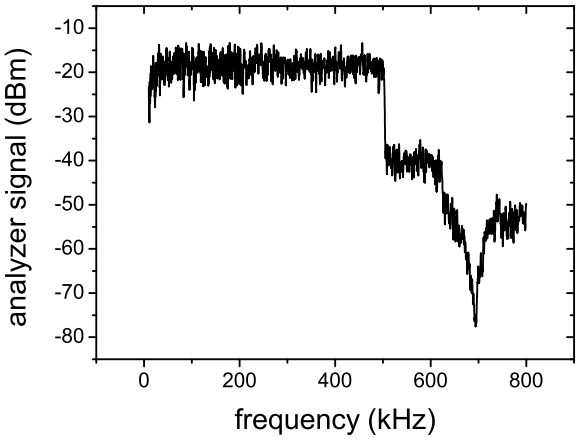

Figure 6.2: Frequency spectrum of the SWIFT signal followed by the notch filter [45]. This signal is applied to the dipolar excitation line to remove all undesired ions. The axial frequency of protons is tuned to the center of the notch filter. Thus, the axial motion of the proton is protected from the excitation.

SWIFT-signal in a way to leave only a few protons in the trap. It is assumed that all unwanted ion species are removed since they experience a much stronger excitation and therefore should be lost earlier than protons.
Still, every unexpected and at first glance unexplainable behaviour of the proton can be easily assigned to a contaminant since the interaction of two ions is complicated and can manifest itself in various effects [74]. Thus, an additional cleaning procedure was implemented which focuses on the instability of the eigenmotion of undesired ion species. According to Eq. (2.5) stable storage is only possible if the discriminant is positive

$$\omega_c^2 - 2\omega_z^2 > 0 \quad . \tag{6.2}$$

This means that ions get lost when the radial force due to the electric field is larger than the Lorentz force

$$2\sqrt{2c_2V_0} > \sqrt{\frac{q}{m}}B_0 \quad , \tag{6.3}$$

which is experimentally realized by ramping the ring voltage in our analysis trap to $V_0 = -150\,\mathrm{V}$. Only protons experience stable trapping conditions for this potential depth meanwhile all other ion species are lost. The analysis trap is perfectly suited for this cleaning procedure since c_2 is more than a factor of three larger than in the precision trap. Moreover, the magnetic field B_0 is reduced due to the ferromagnetic ring electrode. To provide a ring voltage of $V_0 = -150\,\mathrm{V}$ a separate voltage supply was employed and the capacitors of the corresponding DC-filters were exchanged. We assume that this cleaning procedure is much more robust than the SWIFT- and sweep-techniques since it is based on the fundamental trapping conditions rather than on increasing the axial amplitude of

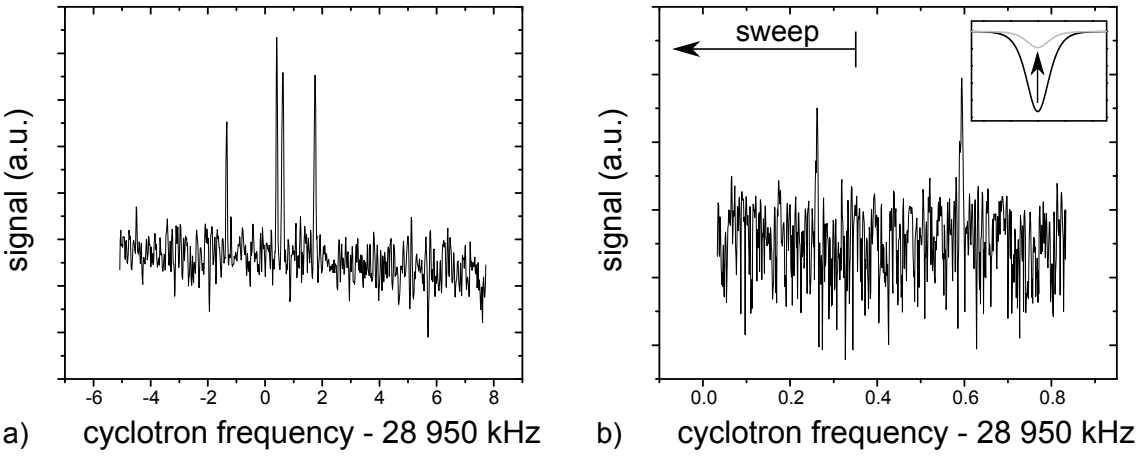

Figure 6.3: a) Frequency spectra of the modified cyclotron mode of a cloud of protons. In a) the discrete peaks indicate individual protons. The cleaning procedure is illustrated in b). The left peak corresponds to an excited proton which can be further excited by an external driving field swept down in frequency. The energy in the modified cyclotron mode is increased until the proton leaves the trapping potential. Instead of further heating of the modified cyclotron mode, the trapping potential can be lowered until the proton is lost (see inset of b)). The larger amplitude of the right peak indicates, that this signal is generated by more than one proton with approximately the same cyclotron energy.

undesired ion species.

6.3 Reducing the number of protons

Reducing the number of protons is under much better control than cleaning of contaminants since we are able to count the number of protons in our trap. According to Eq. (4.23) the width of the axial noise dip is proportional to the number of trapped protons. Thus we can count protons by measuring the width of the axial noise dip.
Having a cloud of more than one proton the modified cyclotron mode is excited to remove hot protons until one proton is left. Due to imperfections of the trapping potential, an increase of the cyclotron energy causes a decrease of the oscillation frequency (see chapter 2). Thus, the peak of the excited proton cloud will be broadened due to the energy spread. By application of several excitation sweeps, the broad signal splits into discrete peaks, each indicating an individual proton. A spectrum of an excited proton cloud is shown in Fig. 6.3. Two different techniques can be applied to reduce the number of protons:

- An rf-sweep can be applied to drive protons from the trap. The frequency is swept downwards since a higher motional amplitude results in a lower motional frequency. Thus, the particle is gradually heated until it leaves the trap. The starting frequency is chosen low enough to leave the cold proton unaffected.

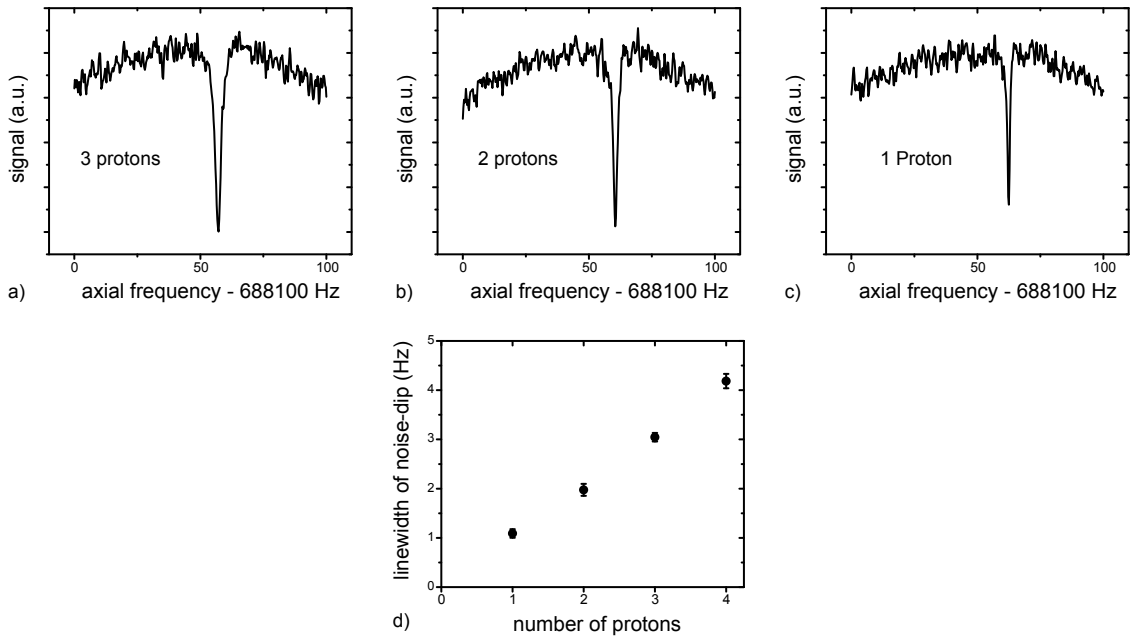

Figure 6.4: a)-c) Axial frequency spectra for various numbers of protons [45]. The width of the noise dip increases linearly with the particle number which is summarized in d).

- Protons with high motional amplitudes in the modified cyclotron mode are removed by lowering the trapping potential. The evaporation rate can be controlled by the potential depth which means that a proton with a certain modified cyclotron frequency (equivalent to a certain energy) will leave the trap at a specific ring voltage. This procedure requires a little experimental experience but works very reliable.

Both procedures can be utilized to prepare a single proton. In Fig. 6.4 the width of the axial noise dip is shown as a function of the number of particles. By measuring the linewdith of the axial noise dip, we can prove that a single proton is left in the trap.

6.4 Transport

The determination of the g-factor requires a fast and reliable exchange of the proton between the AT and the PT. Therefore, appropriate voltage ramps are applied to the transport electrodes separating both traps. The diameter of the transport electrodes varies since the inner diameter of the AT is about a factor of two smaller than for the PT. In a first design the constriction was realized within a single transport electrode as shown in Fig. 6.5a). However, we were not able to pass a proton through this electrode although we tried many different transport schemes. Investigating the transport efficiency is complicated since diagnosis tools are only available in the PT. Moreover it is very time consuming since every loss of protons requires a reloading and the preparation procedure presented in the previous section. We finally succeeded by separating the constriction into three electrodes as shown in Fig. 6.5b). Moreover, we split both endcaps of the

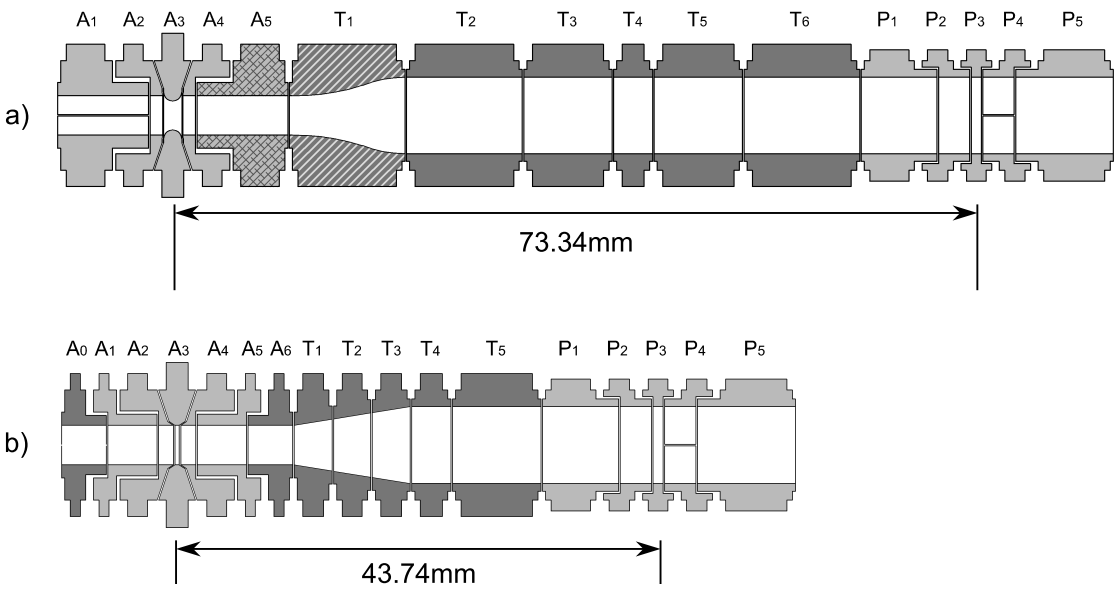

Figure 6.5: a) Electrode stack with the former transport section (dark grey) between analysis trap (left) and precision trap (right). No protons returned to the precision trap when transporting them into the transport electrode T_1 (dashed). b) As a solution, the constriction was split into three separate electrodes T_1-T_3 and both endcaps of the analysis trap were split into two electrodes A_5+A_6 and A_0+A_1, respectively. With this configuration, the transport of protons between both traps works reliably. Sketch adopted from [46].

analysis trap into two electrodes. Due to the shorter length of the transport electrodes and endcaps of the analysis trap, the distance between both traps is reduced. With this configuration, we immediately achieved a reliable exchange between both traps. From our experimental observations we conclude that transport electrodes should in general be short compared to their inner diameter [46]. Thus, the electrostatic potential is under much better control. Moreover, the gold deposition in longer electrodes works not properly resulting in a nonuniform surface of gold, silver (barrier-layer) and copper. The different work functions of these materials result in a disturbed potential which might lead to particle losses.

A transport of the proton between the precision trap PT and the analysis trap AT is conducted in the following way: The transport starts by ramping down the ring voltage of the PT to $-14\,\mathrm{V}$. Then the adjacent electrode towards the AT (P_2) is ramped down to $-14\,\mathrm{V}$ meanwhile the opposite adjacent electrode (P_4) is ramped to ground potential. This procedure is subsequently repeated with the next electrodes towards the AT until the proton reaches the ring electrode (A_3) of the destination trap. The transport from AT to PT works in the same way. Each ramp takes 2 s which results in an overall transport time of 40 s.

Chapter 7

Free cyclotron frequency measurement in the precision trap

The determination of the g-factor of the proton is based on the measurement of the Larmor frequency ν_L in a well-known magnetic field. To this end, spin transitions are probed in the homogeneous magnetic field in the precision trap. The magnetic field information is obtained from a measurement of the free cyclotron frequency $\nu_c = \frac{1}{2\pi}\frac{q}{m}B_0$, which is determined from the three eigenfrequencies of the trapped proton by application of the invariance theorem (see Eq. (2.8)). The uncertainty of the free cyclotron frequency is given by

$$\Delta\nu_c = \sqrt{\left(\frac{\nu_+}{\nu_c}\Delta\nu_+\right)^2 + \left(\frac{\nu_z}{\nu_c}\Delta\nu_z\right)^2 + \left(\frac{\nu_-}{\nu_c}\Delta\nu_-\right)^2} \quad . \tag{7.1}$$

In this chapter, the corresponding uncertainties for the frequency determination of each eigenmode will be discussed. Due to the hierarchy of the eigenfrequencies $\nu_+ \gg \nu_z \gg \nu_-$, the resulting precision of the free cyclotron frequency is mainly limited by the uncertainty of the measurement of the modified cyclotron frequency ν_+.

This chapter is separated into three parts, each covering the measurement of one of the eigenfrequencies of the trapped proton:
The determination of the axial frequency ν_z is discussed in the first section 7.1. A precise measurement of ν_z is not only important for the determination of ν_c but also for most experimental routines.
The measurement of the magnetron frequency ν_- by a sideband-coupling is presented in section 7.2.
Different measurement schemes for the modified cyclotron frequency ν_+ are discussed in section 7.3.

7.1 Measurement of the axial frequency

We detect the axial frequency as a dip in the noise spectrum, which provides the possibility to measure ν_z at small motional amplitudes. Various optimization procedures as harmonicity tuning (section 7.1.1), trap alignment (section 7.1.2), asymmetry compensation (section 8.2) and energy calibration [45] prove the variety of applications of the axial detection system.

7.1.1 Harmonicity tuning

The precise determination of the axial frequency with the dip-technique requires the reduction of anharmonicities of the trapping potential. The proton is tuned into resonance with the detection system by a proper voltage at the ring electrode. A non-vanishing anharmonicity of the trapping potential leads to a broadening and a reduction of the depth of the noise-dip due to the Boltzmann-distributed energy of the axial mode. The lineshape is given by the convolution of the Lorentzian lineshape (see Eq. (4.21) for $\nu_z = \nu_{LC}$) and the thermal Boltzmann distribution [45]

$$\chi(\omega) = \frac{A}{\pi k_B T_z} \int_0^\infty dE_z exp\left(-\frac{E_z}{k_B T_z}\right) \frac{\gamma_z/2}{\left(\omega - \omega_z\left(1 + \frac{3}{4}\frac{c_4}{c_2^2}\frac{E_z}{qV_0}\right)\right)^2 + \gamma_z^2/4} \quad , \tag{7.2}$$

where E_z is the axial energy, T_z is the temperature of the axial detection system, A is a normalization factor and γ_z is the damping constant of the axial detection system. Only the lowest order of the anharmonicity c_4 has to be considered since higher order corrections (c_6,...) can be neglected due to the small particle amplitudes in thermal equilibrium with the cryogenic detection system.
The electrostatic anharmonicities are reduced by optimization of the voltage applied to the correction electrodes. The ratio between the correction and ring electrode voltages is called tuning-ratio TR. Axial frequency spectra for different tuning-ratios are shown in Fig. 7.1a). The narrowest dip with the largest depth indicates the most harmonic potential. With this method, the tuning-ratio can be optimized to a precision of 0.2 mUnits.
Further optimization of the trapping potential is realized by a measurement of the energy-dependent shift of the axial frequency, which scales proportional to the electrostatic anharmonicity (see Eq. (2.21)). The axial frequency is recorded as a function of the tuning-ratio for two different axial energies. The higher axial energy is realized by an increased temperature of the detection system due to a broadband white noise drive at the corresponding feedback line. A vanishing frequency shift indicates the optimal tuning-ratio. Note that the contribution of the c_6-term is only negligible for a moderate increase of the axial temperature. For higher temperatures, a vanishing frequency shift would correspond to finite c_4 and c_6-terms with opposite signs and the resulting tuning-ratio would not be the optimal tuning-ratio for the dip detection at low temperatures. Thus, the temperature is only slightly increased until a significant difference between the axial frequencies for the hot

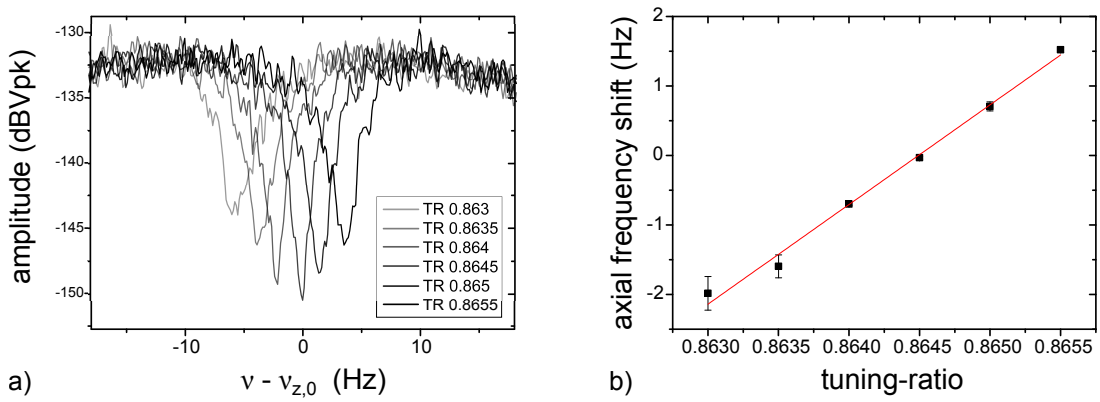

Figure 7.1: a) Axial noise dip of a single proton for different tuning-ratios. The trap is not completely *orthogonal* ($D_2 = 3.3\,\mathrm{Hz/mUnit}$), which results in a shift of the axial frequency as a function of the tuning-ratio. The lowest c_4-term is indicated by the dip with the largest depth. The optimal tuning-ratio can be determined with a precision of 0.2 mUnits. b) Axial frequency shift between two different axial temperatures as a function of the tuning-ratio (squares). The shift scales linearly with the tuning-ratio, as expected from Eq. (2.21). The optimal tuning-ratio of $TR_{\mathrm{opt}} = 0.86449(4)$ can be determined from a linear regression (solid line).

and the cold proton as a function of the tuning-ratio is observed as shown in Fig. 7.1b). The temperature difference can be calculated from the slope $\Delta\nu_z/\Delta TR$ (see Eq. 2.21) and yields

$$\Delta T_z = \frac{8}{3}\frac{m_p\pi^2\nu_z}{k_B}\frac{c_2}{d_4}\frac{\Delta\nu_z}{\Delta TR} = 35\,\mathrm{K} \quad . \tag{7.3}$$

The size of c_2 and $d_4 = \partial c_4/\partial TR$ can be found in Tab. 2.1). For this low temperature, the contribution of the c_6-term is neglected.
From a fit to the data the optimal tuning-ratio $TR_{\mathrm{opt}} = 0.86449(4)$ can be determined. The uncertainty of 0.04 mUnits corresponds to an anharmonicity of $c_4 = 1.3 \cdot 10^{-7}\,\mathrm{mm}^{-4}$. The corresponding systematic shift of the free cyclotron frequency can be calculated from the resulting frequency shifts of the three eigenfrequencies (see Eq. (2.21) to Eq. (2.23)). This results in a relative shift of ν_c of the order of 10^{-11} for energies of about 1 meV in the motional modes. Thus, corrections due to the electrostatic anharmonicities are no limitation for a relative precision of 10^{-9} in the proton g-factor.

7.1.2 Trap alignment

The invariance theorem even holds for a small tilting angle θ between the symmetry axis of the trap with respect to the magnetic field axis [41]. This means that a tilt does not cause a systematic shift of the free cyclotron frequency. However, a misalignment would lead to an unwanted increase of the magnetron radius when transporting the proton between the

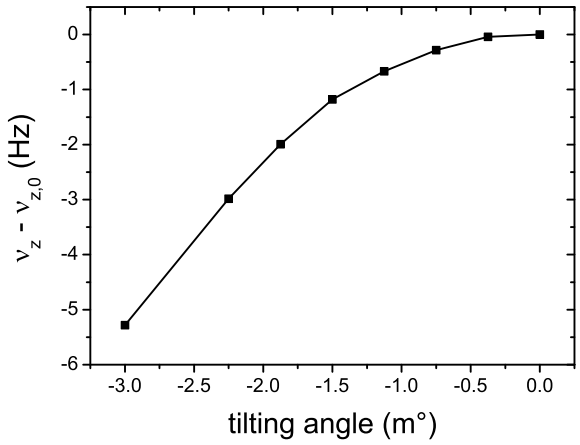

Figure 7.2: Axial frequency as a function of the tilting angle between the electrostatic axis and the magnetic field axis. The optimization procedure was stopped for the largest axial frequency, which corresponds to a vanishing tilt in the horizontal plane.

traps. Thus, a tilt should be avoided. The mechanical support of our experiment provides the possibility to compensate a possible misalignment by adjusting the angle θ between the electrostatic axis and the magnetic field axis. The axial frequency depends on the tilting angle [41]

$$\nu_z(\theta) = \nu_{z,0}\sqrt{1 - \frac{3}{2}\sin^2(\theta)} \approx \nu_{z,0}\left(1 - \frac{3}{4}\theta^2\right) \quad . \tag{7.4}$$

Thus, the axial frequency can be utilized to monitor the tilt of the precision trap when shifting the apparatus as shown in Fig. 7.2. The largest axial frequency indicates an aligned precision trap in the horizontal plane. The decrease of the axial frequency for a further rotation as expected from Eq. (7.4) was not recorded since hysteresis in the adjustement mechanics would prevent a simple reproducibility of the minimzed angle. A similar optimization process has to be performed for the vertical plane in order to obtain a perfect aligned trap. After optimization, the magnetron radius was observed to be unaffected by particle transport.

7.1.3 Axial frequency stability

To obtain a relative uncertainty better than $\Delta\nu_c/\nu_c < 1\,\text{ppb}$ for the free cyclotron frequency, the axial frequency has to be determined with a precision better than $\Delta\nu_z < 1\,\text{Hz}$ (see Eq. (7.1)).

The long-term stability of the axial frequency is shown in Fig. 7.3a). The peak-to-peak fluctuations of 0.4 Hz correspond to relative fluctuations of $\Delta\nu_c/\nu_c = 0.4\,\text{ppb}$. The stability of the axial frequency Ξ, which is defined as the standard deviation of the difference between two subsequent measurements of ν_z, is shown in Fig. 7.3b) as filled squares. Further

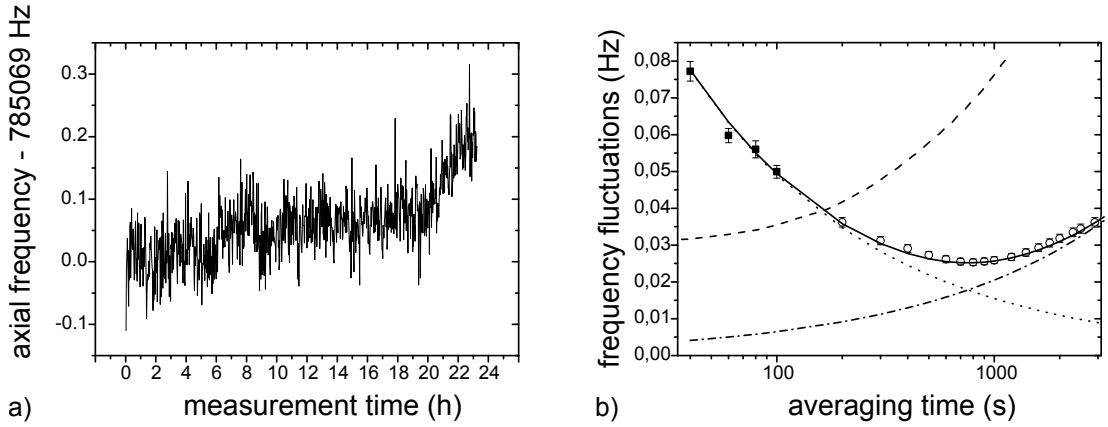

Figure 7.3: a) Subsequent axial frequency measurements over a period of one day for an FFT-averaging time of $T = 100\,\mathrm{s}$. The difference of the average of i subsequent frequency measurements is calculated and the standard deviation of these frequency differences as a function of the averaging time ($i \cdot 100\,\mathrm{s}$) is shown in b) as unfilled circles. The filled squares correspond to independent datasets which were obtained for different FFT-averaging times. The datapoints are approximated by the solid line, which is given by the sum of two contributions: The decreasing dotted curve corresponds to the frequency uncertainty due to noise averaging of the FFT-spectrum. A drift of the voltage supply which biases the electrodes causes an increase for longer averaging times, which is observed for averaging times $T > 800\,\mathrm{s}$ (dashed dotted line). The dashed line corresponds to the frequency stability which is expected from the measured voltage stability (see section 5.5) being significantly lower than expected from the measured voltage stability.

informations for longer averaging times can be determined from the measurement shown in Fig. 7.3a): The difference of the average of i subsequent axial frequency measurements is calculated. The standard deviation of these differences as a function of the averaging time ($i \cdot 100\,\mathrm{s}$) is shown as unfilled circles in Fig. 7.3b). Noise averaging of the FFT-spectrum, which allows for a more precise determination of the axial frequency from the dip in the noise spectrum for longer averaging times, causes a decrease of the frequency uncertainty (dotted line). An increase of the frequency fluctuations due to voltage fluctuations for averaging times $T > 800\,\mathrm{s}$ is observed. The solid line approximates the data, which is the sum of the contributions of voltage fluctuations (dashed dotted line) and noise averaging (dotted line). However, the observed scaling of the voltage fluctuations is not explainable by the measured voltage stability (dashed line)(see section 5.5). This discrepancy can be explained by the unknown noise- and drift-characteristics of the multimeter, which was utilized to measure the voltage stability and the improved temperature stability of the voltage supply.
The frequency fluctuations for an averaging time of $T = 40\,\mathrm{s}$ correspond to an uncertainty of the free cyclotron frequency of $\Delta\nu_c/\nu_c = 0.07\,\mathrm{ppb}$. Thus, the uncertainty of the axial frequency measurement is no limitation for a measurement of ν_c with a relative precision of 10^{-9}.

7.2 Measurement of the magnetron frequency

We measure the magnetron frequency ν_- with the double-dip technique described in section 4.4. A driving field at $\nu_{\mathrm{rf}} = \nu_z + \nu_- + \delta$ is applied to one half of a split correction electrode of the precision trap with an amplitude of $-34\,\mathrm{dBm}$ at the room temperature flange of the quadrupole-excitation line. The driving field leads to a coupling of the magnetron mode to the axial mode. The resulting double-dip spectrum is shown as solid line in Fig. 7.4a) and b). The dotted curve shows the single dip spectrum, which is obtained from an independent measurement with no coupling field. The magnetron frequency can be determined from

$$\nu_- \quad = \quad -\nu_l - \nu_r + \nu_z + \nu_{\mathrm{rf}} \quad , \tag{7.5}$$

where ν_l and ν_r are the left and right frequencies of the double-dip, ν_z is the frequency of the single-dip and ν_{rf} is the driving frequency. For the plot shown in a), a magnetron frequency of $\nu_- = 10640.55(10)\,\mathrm{Hz}$ is obtained which agrees well with the value for b) $\nu_- = 10640.48(9)\,\mathrm{Hz}$. The detuning of the coupling field from the resonance frequency is given by $\delta = -4\,\mathrm{Hz}$ and $\delta = +4.5\,\mathrm{Hz}$ for Fig. 7.4a) and Fig. 7.4b), respectively. The double-dip frequencies as a function of the coupling frequency are shown in Fig. 7.4c) which yields an avoided crossing [61]. The relative precision of better than $\Delta\nu_-/\nu_- = 10^{-5}$ corresponds to a contribution to the relative uncertainty of the free cyclotron frequency of less than 10^{-11}. Thus, the measurement of the magnetron frequency is no limitation for a sub-ppb

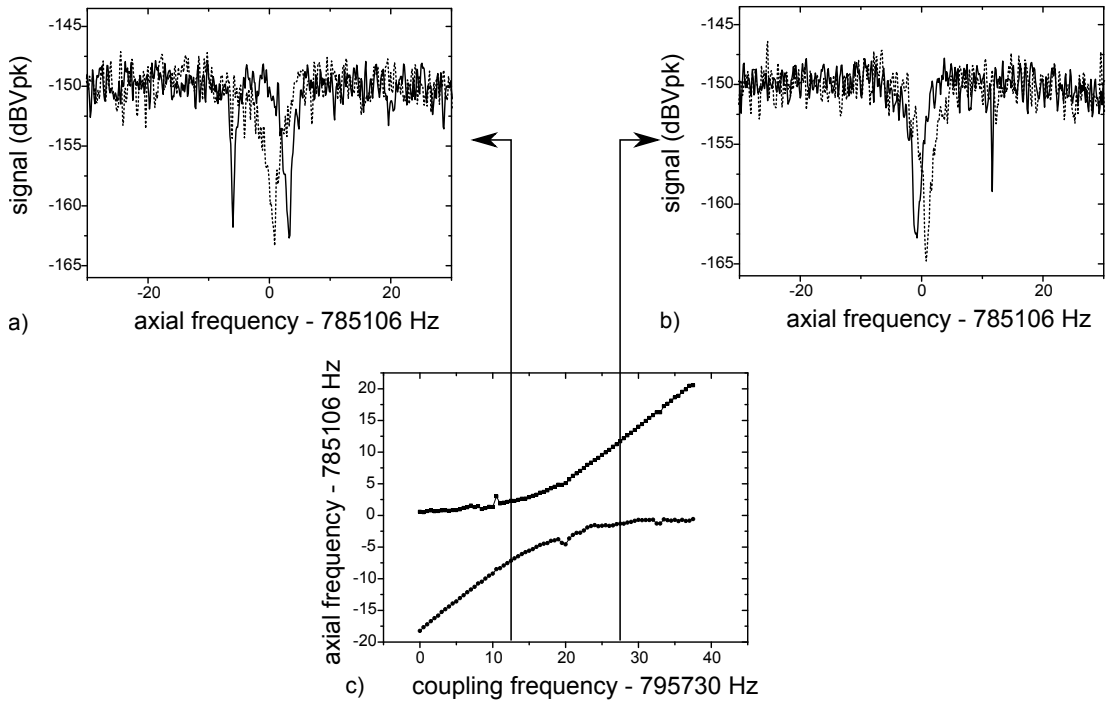

Figure 7.4: a) and b): A single proton in thermal equilibrium with the axial detection system. Each spectrum was obtained in $T = 50\,\mathrm{s}$ averaging time. The double-dip spectrum (solid line) is obtained for a sideband-coupling field at frequency $\nu_{\mathrm{rf}} = \nu_z + \nu_- + \delta$. The detuning from resonance is given by $\delta = -4\,\mathrm{Hz}$ in a) and $\delta = +4.5\,\mathrm{Hz}$ in b), respectively. For a larger detuning, the separation of the dips increases. The dotted curve shows the single-dip spectrum, which is obtained without coupling field. The magnetron frequency of $\nu_- = 10640.55(10)\,\mathrm{Hz}$ for a) and $\nu_- = 10640.48(9)\,\mathrm{Hz}$ for b) is calculated using Eq. (7.5). c) The frequencies of the double-dips are plotted as a function of the coupling frequency, which yields an avoided crossing [61].

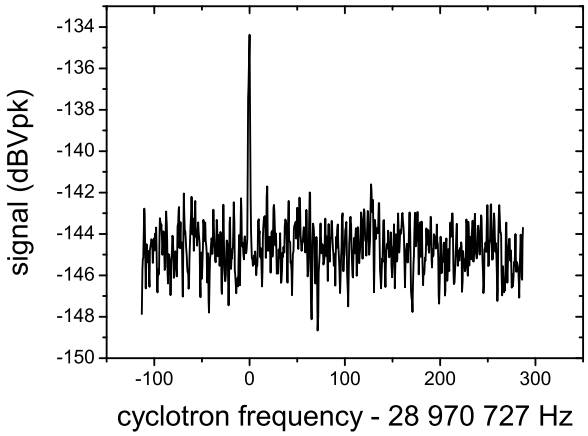

Figure 7.5: The signal of an excited proton is shown.

determination of the free cyclotron frequency.

7.3 Measurement of the modified cyclotron frequency

This section gives an overview of different detection schemes for the modified cyclotron frequency ν_+, which have been implemented at our experiment. Since the modified cyclotron frequency ν_+ is approximately equal to the free cyclotron frequency ($\nu_+/\nu_c \approx 0.9996$), the uncertainty of the measurement of the modified cyclotron frequency is the main limitation for the measurement of the magnetic-field strength and thus for the determination of the g-factor.

7.3.1 The cyclotron cooling-curve

The convential detection technique for the modified cyclotron frequency ν_+, which utilizes the cyclotron detection system, is based on the detection of the signal generated by an excited proton. The proton is heated to an energy $E_{+,1}$ of several eV by a driving field. The frequency of the drive is swept down over a range of 1 kHz in a time of 10 s at an amplitude of -55 dBm at the room-temperature flange of the quadrupole-excitation line. After turning off the drive, the coherent signal is observed (see Fig. 7.5) and the modified cyclotron frequency can be measured. However, at such high motional amplitudes the oscillation frequency is shifted compared to the frequency at vanishing oscillation amplitude due to the presence of anharmonicities

$$\frac{\Delta\nu_+}{\nu_+}(E_+) = \left[\frac{1}{qV_0}\frac{3c_4}{c_2^2}\left(\frac{1}{4}\frac{\nu_z}{\nu_+}\right)^4 - \frac{1}{m_p\nu_z^2}\frac{B_2}{B_0}\left(\frac{\nu_z}{\nu_+}\right)^2 - \frac{1}{m_pc^2}\right]E_+ \quad . \tag{7.6}$$

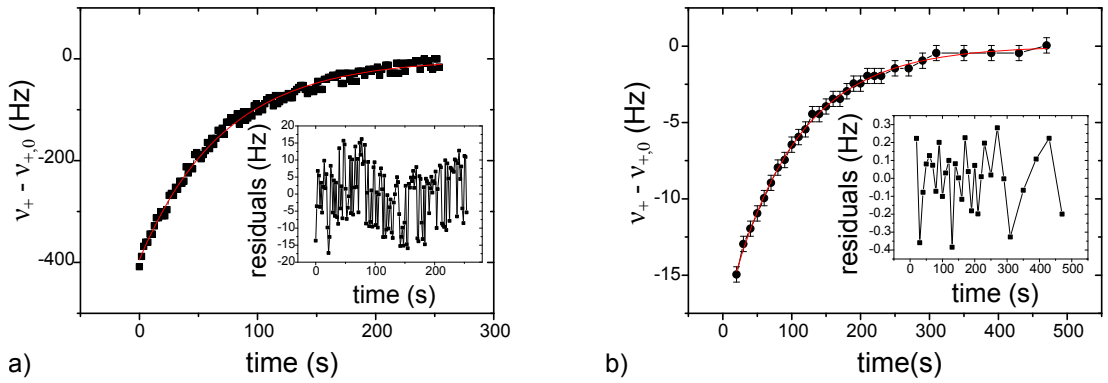

Figure 7.6: a) Time evolution of the modified cyclotron frequency for the former setup utilizing a puls-tube cooler to provide the cryogenic environment. The residuals of an exponential decay reveal large oscillations which were associated to cooler vibrations. b) A liquid cryostat provides the cryogenic temperatures for the new setup. The exponential fit to the data gives a modified cyclotron frequency of $\nu_+ = 28\,970\,739.955(92)$ Hz which corresponds to a relative uncertainty of $\Delta\nu_+/\nu_+ = 3 \cdot 10^{-9}$. The residuals of the cyclotron cooling curve are reduced by a factor of 50 compared to a), indicating that the oscillation of ν_+ was caused by vibrations of the puls-tube cooler. Note that the whole scale of the decay curve in b) is less than the scale of the residuals shown in a). The cooling time constant of $\tau_+ = 70.9(1.3)$ s for a) and $\tau_+ = 98.8(2.1)$ s for b) agrees with the corresponding measured quality factors of $Q \approx 700$ and $Q \approx 500$ of the cyclotron detection system. The quality factor of the cyclotron detection system is changed for different experimental runs due to different magnitudes of the rf-losses in the tank circuit. The highest achieved value for the quality factor is $Q = 1250$ [45](see Tab. 4.1).

The last term in the brackets corresponds to the frequency shift caused by special relativity [39]. The proton will dissipate energy in the tank circuit at the time constant τ_+ until it reaches thermal equilibrium with the detection system. Recording the evolution of the modified cyclotron frequency over time

$$\nu_+(t) = \nu_{+,0}\,(1 - \alpha_+ E_{+,1} \exp\,(-t/\tau_+)) \tag{7.7}$$

results in an exponential decay curve as shown in Fig. 7.6, where α_+ is given by the sum of the frequency shifts of Eq. (7.6). From an exponential fit to the data we can extrapolate the frequency of the modified cyclotron mode at thermal equilibrium with the detection system $\nu_{+,0}$.

Due to vibrations of the pulse tube cooler, utilized in the former setup, magnetic field variations in the range of several μT were induced. The residuals of an exponential fit to a cyclotron cooling curve clearly show these fluctuations (see inset of Fig. 7.6a)). The size of the vibrations were measured with a position sensitive diode to be of the order of 40 μm [72]. However, the homogeneity of the magnetic field at the position of the precision trap was measured with an NMR-probe, to vary at the level of 1 μT for a volume of about 1 cm^3, only [66]. The reason for the observed fluctuations of several μT due to oscillations

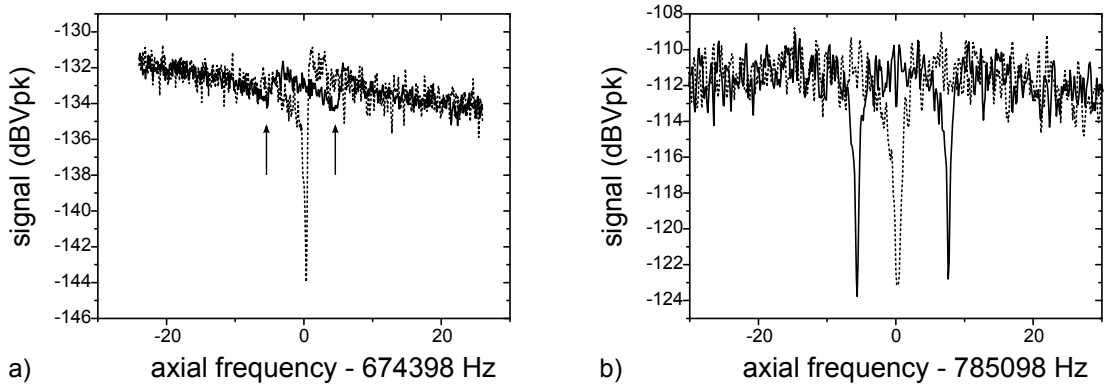

Figure 7.7: Single- and double-dip spectra of a single proton in thermal equilibrium with the axial detection system. By application of a sideband drive at $\nu_{\mathrm{rf}} = \nu_+ - \nu_z$ the axial dip splits symmetrically. a) For the puls-tube cooler, the double-dips (arrows) are smeared out due to magnetic field variations induced by cooler vibrations. b) These vibrations were eliminated by use of a liquid cryostat instead of the puls-tube cooler. A modified cyclotron frequency of 28 966 061.997(32) Hz is calculated from the frequencies of the double-dip and the single dip, which allows us to measure the modified cyclotron frequency with the double-dip technique with a relative precision of about one ppb.

in the μm-range is not understood.
In a first attempt [72], the trapping region was mechanically decoupled from the vibrating cooler stages, which reduced fluctuations in the magnetic field by a factor of ten. However, the resulting fluctuations of ± 1.1 Hz still limited the relative precision of the modified cyclotron frequency to $\Delta\nu_+/\nu_+ = 3 \cdot 10^{-8}$. Thus, the puls tube cooler was replaced by a liquid cryostat to avoid any vibration-induced magnetic field variations. A cyclotron cooling curve, which was measured with the new setup is shown in Fig. 7.6b). The residuals clearly indicate that no periodic fluctuations of the magnetic field are present when utilizing a liquid cryostat. With the improved setup, the modified cyclotron frequency can be determined with a relative precision of $\Delta\nu_+/\nu_+ = 3$ ppb in several minutes from a cooling curve.

7.3.2 Sideband coupling of the modified cyclotron mode to the axial mode

The liquid cryostat enabled us to perform more precise measurements of the modified cyclotron frequency ν_+ by a sideband-coupling to the axial mode than possible with the former setup. The two double-dip spectra shown in Fig. 7.7a) and b) were measured with the former setup utilizing a puls-tube cooler and the new setup utilizing a liquid cryostat, respectively. The improved frequency stability of the modified cyclotron mode due to the elimination of vibrations is clearly visible. The single- and the double-dip spectra shown in Fig. 7.7b) were recorded for an averaging time of $T = 90$ s, respectively. The modified

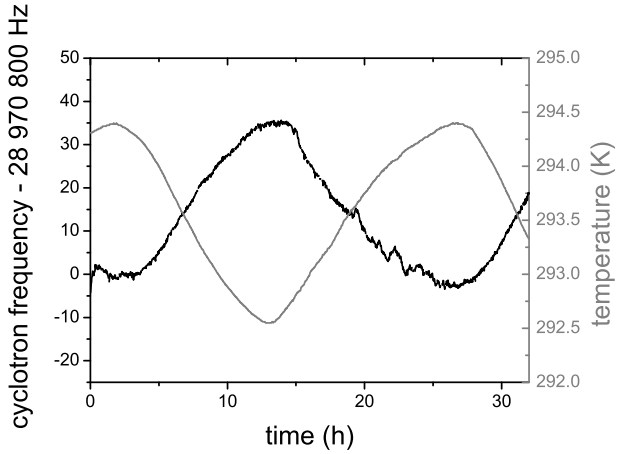

Figure 7.8: The time evolution of the modified cyclotron frequency (black) is strongly correlated to the temperature (grey) of the CF-200 double-cross (see Fig. 5.1).

cyclotron frequency is given by

$$\nu_+ = \nu_l + \nu_r - \nu_z + \nu_{\mathrm{rf}} \quad , \tag{7.8}$$

yielding a modified cyclotron frequency of 28 966 061.997(32) Hz, which corresponds to a relative uncertainty of 1.1 ppb. The measurement time of ν_+ with the double-dip technique is reduced by about a factor of three compared to the cyclotron cooling curve scheme. Due to the lower measurement time and the higher accuracy, the sideband-coupling technique is usually used to determine ν_+.

However, the observed long term stability was very poor as shown in Fig. 7.8. Peak-to-peak drifts of up to $\Delta\nu_+ = 40\,\mathrm{Hz}$ were observed for a time period of one day. A correlation of these drifts to temperature variations of the experimental setup was observed as shown in Fig. 7.8. The temperature was measured with a PT-100 sensor, thermally anchored to the CF-200 double-cross (see Fig. 5.1). A possible explanation for this correlation is the thermal expansion of the CF-200 double-cross (see Fig. 5.1). Assuming, that the observed drift is caused by the same physical effect as for the vibration induced fluctuations (see Fig. 7.6) would require a shift of the Penning traps of about $50\,\mu\mathrm{m}$. The traps are mechanically coupled to the cold finger of the helium dewar which is mounted on top of the CF-200 double-cross (see Fig. 5.1). The double-cross itself is connected to the magnet with a flexible bellow. The distance from the middle of the double-cross to the magnet is about 30 cm. For stainless steel the thermal expansion coefficient is $16.1 \cdot 10^{-6}\,\mathrm{K}^{-1}$ [75], which yields a thermal expansion for a temperature difference of 2 K of about $10\,\mu\mathrm{m}$. Thus, a shift of the traps with respect to the superconducting magnet could be the reason for the observed correlation. However, the discrepancy by a factor of 5 requires further investigation. A temperature stabilization has recently been set up by Andreas Mooser, which stabilizes the temperature of the whole apparatus including the superconducting magnet. The performance of the temperature stabilization system and

the resulting fluctuations of the modified cyclotron frequency will be part of the Ph.D.-thesis of Andreas Mooser [57].

7.3.3 The cyclotron noise-dip

A third possibility to measure the modified cyclotron frequency ν_+ is discussed in the following section: The first determination of ν_+ in thermal equlibrium with the cyclotron detection system from the noise dip is presented [1]. A corresponding publication is in preparation [76].
The main experimental challenge for the application of the dip-technique for the cyclotron mode is the lower resonance resistance R of the cyclotron detection system compared to the axial detection system. Due to the high frequency of the modified cyclotron mode the inductance L of the coil for the cyclotron mode is only $L = 1.5\,\mu\text{H}$, which is three orders of magnitude smaller than for the axial system (see Tab. 4.1). Furthermore, the quality factor is limited by losses in the LC-circuit, which scale proportional to the resonance frequency ν_{LC}, such as for example the skin-effect [77]. The resulting quality factor of $Q \approx 700$ results in a resonance resistance of $R = 200\,\text{k}\Omega$, which corresponds to a dip width for a single proton of only $\delta\nu = 3\,\text{mHz}$. This requires a much higher averaging time due to the Fourier limit. However, the modified cyclotron frequency ν_+ shifts several line widths over these time scales due to magnetic field drifts and fluctuations, and thus prevents the detection of the dip. Therefore, the dip-technique has not been applied for the measurement of the modified cyclotron frequency so far.
To overcome this problem we use active electronic feedback as described in section 4.5 in order to increase the effective resistance of the cyclotron detection system and thus the width of the noise-dip. In Fig. 7.9 a schematic of the feedback-loop for the cyclotron detection system is shown. The strength of the feedback signal G_{FB} is adjusted with a voltage controlled attenuator VCA *MC ZX73-2500S+*, which is followed by a bandpass chain consisting of two *MC BLP-30+* low-pass filters and two *MC BLP-25+* high-pass filters. The phase Φ is adjusted by a voltage controlled phase shifter *MC JSPHS-32+*. Thermal noise resonances of the cyclotron detector for different feedback gains are shown in Fig. 7.9b). In order to resolve the cyclotron dip of a single proton, quality factors of the order of 10^6 are required, which requires precise control of the gain G_{FB} and the phase Φ. The VCA and the cryogenic amplifier turned out to be the most critical componenents of the loop in order to obtain a stable quality factor of the order of 10^6. The attenuation of the VCA as a function of the control voltage is shown in Fig. 7.10. In order to obtain a stable gain, the VCA was operated at high control voltages, which reduces the sensitivity on voltage fluctuations of the corresponding biasing supply. Fixed attenuators from *Mini-circuits* were utilized for the coarse-tuning of G_{FB}. In case of the cryogenic amplifier the fluctuation of the gain was reduced by using a stable voltage source ($\Delta V_{\text{bias}}/V_{\text{bias}} \approx 10^{-6}$) for the biasing of the amplifier.

[1] The experimental realization of the cyclotron noise-dip is also part of the Ph.D.-thesis of Andreas Mooser [57]

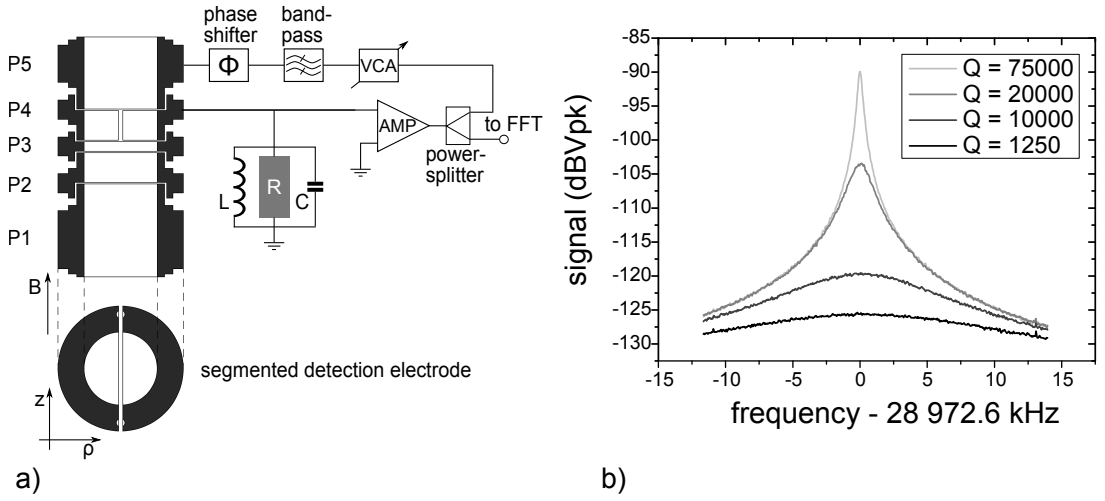

Figure 7.9: a) Schematic of the feedback loop for the detection of the cyclotron dip. The tank circuit for the modified cyclotron mode is attached to one half of the upper correction electrode $P4$. It consists of an inductance L with parasitic capacitance C yielding an effective resistance R on resonance. The detector signal is amplified (AMP) and divided to two equal fractions using a power splitter. One part is mixed down and guided to a Fast Fourier Transform (FFT) spectrum analyzer. The other one is attenuated (VCA), filtered with a bandpass, phase shifted and fed back to the upper endcap electrode $P5$ which is capacitvely coupled to the detector. b) The thermal noise resonance of the cyclotron detection system for different magnitudes of the feedback gain G_{FB} is shown. For details see text.

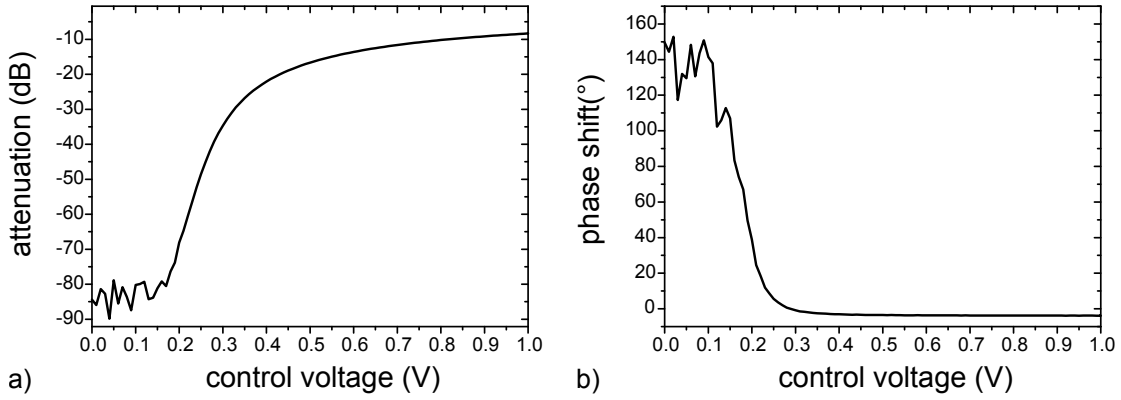

Figure 7.10: a) attenuation and b) phase shift as a function of the control voltage for the VCA *MC ZX73-2500S+*. To obtain a stable feedback gain G_{FB} and phase Φ, the VCA was operated at control voltages of about 0.7 V and was therefore only utilized for fine-tuning of the gain. Thus, the influence of voltage fluctuations of the corresponding biasing supply on the quality factor was greatly suppressed. The coarse-tuning of G_{FB} was realized with fixed attenuators from *Minicircuits*.

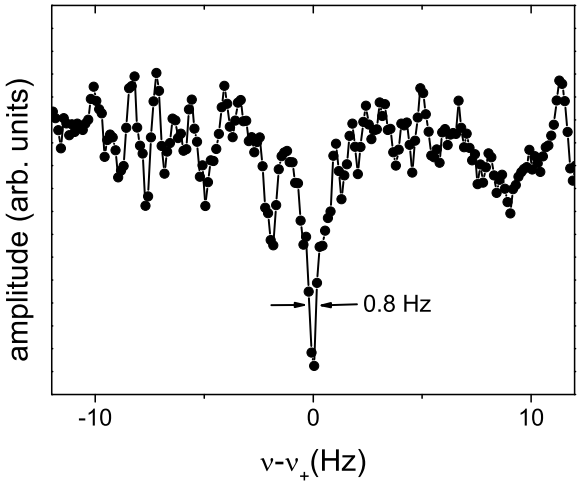

Figure 7.11: Single proton detection in thermal equilibrium with the cyclotron detection system. The quality factor of the tank circuit was enhanced to $Q \approx 200\,000$ by application of active electronic feedback. This corresponds to a line width of the noise-dip of $\Delta\nu_+ \approx 800\,\mathrm{mHz}$. From a fit of the lineshape (see Eq. (4.21)) to the data, a modified cyclotron frequency of $\nu_+ = 28\,972\,591.075(24)\,\mathrm{Hz}$ was determined.

We achieved effective resistances of $R_{\mathrm{eff}} \approx 58\,\mathrm{M\Omega}$ corresponding to $Q \approx 200\,000$, which enabled us for the first time to resolve a cyclotron dip spectrum of a single trapped proton in thermal equilibrium with the detection system, as shown in Fig. 7.11. This spectrum was recorded with 100 s averaging time. A modified cyclotron frequency of $\nu_+ = 28\,972\,591.075(24)\,\mathrm{Hz}$ was determined from a fit of the lineshape (see Eq. (4.21)) to the data.

Due to the strong correlation of the modified cyclotron frequency with the environmental temperature of the experimental setup (see Fig. 7.8) the cyclotron noise-dip could only be detected in periods of stable lab temperature. This obstacle should be overcome in the future by the temperature stabilization system [57].

The effective temperature $T_{+,\mathrm{eff}}$ of the cyclotron detection system is given by

$$T_{+,\mathrm{eff}} = T_+ \frac{R_{\mathrm{eff}}}{R} \approx 1800\,\mathrm{K} \quad , \tag{7.9}$$

for a temperature of the cyclotron detection system without feedback of $T_+ = 6.4\,\mathrm{K}$ (see section 8.4). This yields a motional amplitude of $\rho_+ \approx 30\,\mu\mathrm{m}$ (see Eq. (2.13)) during the measurement of ν_+, which is a factor of 7 larger compared to the double-dip technique. The resulting shifts of ν_+ due to anharmonicities of the trapping potentials and the relativistic mass effect are calculated using Eq. (7.6) and are summarized in Tab. 7.1. The main contribution arises from the magnetic inhomogeneity B_2. Despite the high temperature of the cyclotron mode, the corresponding frequency shift is still smaller than the shift caused by the energy of the axial mode. This becomes clear when considering the effect

Source	Size of parameter	$\Delta\nu_+$ (Hz)
Electrostatic anharmonicity	$C_4 = 1.3 \cdot 10^{-7}\,\mathrm{mm}^{-4}$	$6 \cdot 10^{-5}$
Magnetic inhomogeneity	$B_2 = 4.7\,\mathrm{T/m}^2$	-0.032
Relativistic mass effect		-0.005
Total		-0.037

Table 7.1: Systematic shifts $\Delta\nu_+$ of the modified cyclotron frequency due to anharmonicities of the trapping potentials and the relativistic mass effect for a cyclotron radius of $\rho_+ = 30\,\mu\mathrm{m}$.

of a variation of the corresponding motional amplitudes in the magnetic bottle. The axial component of the magnetic field B_z is given by

$$B_z = B_0 + B_2(z^2 - \rho^2/2) \quad , \tag{7.10}$$

which means that B_z increases on average for a larger axial oscillation amplitude and decreases with increasing cyclotron radius. The cyclotron radius ρ_+ and the axial oscillation amplitude z_0 of the proton can be expressed as

$$\rho_+ = \frac{1}{2\pi\nu_+}\sqrt{\frac{2k_BT_+}{m_p}} \approx 0.7\sqrt{T_+}\,\frac{\mu\mathrm{m}}{\sqrt{\mathrm{K}}} \tag{7.11}$$

$$z_0 = \frac{1}{2\pi\nu_z}\sqrt{\frac{2k_BT_z}{m_p}} \approx 26\sqrt{T_z}\,\frac{\mu\mathrm{m}}{\sqrt{\mathrm{K}}} \quad . \tag{7.12}$$

Thus, the systematic shift of ν_+ for an axial temperature of $T_z = 4.2\,\mathrm{K}$ is a factor of 3 larger than the corresponding shift of ν_+ for a cyclotron temperature of $T_+ = 1800\,\mathrm{K}$.
The determination of ν_+ with the dip-technique allows for the simultaneous measurement of the axial frequency ν_z with the corresponding detection system, which reduces the required measurement time for the free cyclotron frequency by a factor of two. Alternatively, strong negative feedback can be applied to the axial detection system, which reduces the shift of the modified cyclotron frequency and therefore allows for a more precise determination of ν_+ than with the double-dip technique. The technical realization of stable quality factors of the order of 10^6 is challenging, which complicates a reliable use of the cyclotron dip on long time scales. Thus, for the upcoming measurement of the g-factor, which is expected to take several weeks to months, the double-dip technique will be used. The reliability of the cyclotron-dip technique can be improved by a further optimization of the critical components of the feedback loop. Moreover, the presented measurement of the cyclotron dip utilized a cyclotron detector with a quality factor of $Q \approx 700$. Quality factors of the cyclotron detector of up to $Q = 1250$ were already achieved in former experimental runs, which would reduce the required gain to resolve the cyclotron dip and also reduce the effective temperature in the cyclotron mode, yielding systematic shifts of ν_+ below the ppb-level.
The feasibility to resolve the cyclotron dip for highly charged ions at moderate feedback gains and thus at even lower temperatures is discussed in appendix A.

Chapter 8

A single proton in the analysis trap

The analysis trap is designed to enable the discrimination between the two spin states of the proton by the application of the continuous Stern-Gerlach effect [33]. This is an essential ingredient of the experimental routine to determine the g-factor as presented in section 3.4. Therefore, the analysis trap incorporates a magnetic bottle of $B_2 = 300\,\mathrm{mT/mm^2}$, which is the largest inhomogeneity ever superimposed to a single particle Penning trap experiment [47]. As a consequence, already tiny amplitude variations of the eigenmotions cause huge frequency shifts (see section 3.3). Only the axial frequency is insensitive to thermal fluctuations of its motional amplitude. Thus, only the axial mode can be detected directly with a dedicated detection system. The small trap size ($\rho_0 = 1.8\,\mathrm{mm}$) increases the sensitivity on patch effects which can cause significant deviations from the calculated electrostatic potential [78]. This complicates the process of finding the dip signature with the axial detection system as discussed in section 8.1. However, we developed an optimization procedure presented in section 8.2 to experimentally detect and compensate the various offset potentials present on all electrodes.

The convential double-dip technique to measure the radial frequencies as presented for the precision trap (see section 7.2 and 7.3.2) can not be applied in the strong magnetic inhomogeneity. Thus, special measurement routines for ν_+ and ν_- as discussed in section 8.3 are required. A precise knowledge of the strength of the magnetic inhomogeneity gives the opportunity to interesting measurements: Due to the strong scaling of the axial frequency with the radial energies, the axial mode can be used as a *thermometer* of the mode temperatures as will be discussed in section 8.4.

The observation of a spin transition requires the ability to resolve an axial frequency shift of 171 mHz at a total axial frequency of 742 kHz. However, the stability of the axial frequency is limited due to energy fluctuations in the radial modes. We performed systematic studies on the origin of theses fluctuations which is presented in section 8.5. These investigations led to the modifications of the experimental setup as described in section 5.7 which decreased the instability of the axial frequency by a factor of 3. The increased stability of

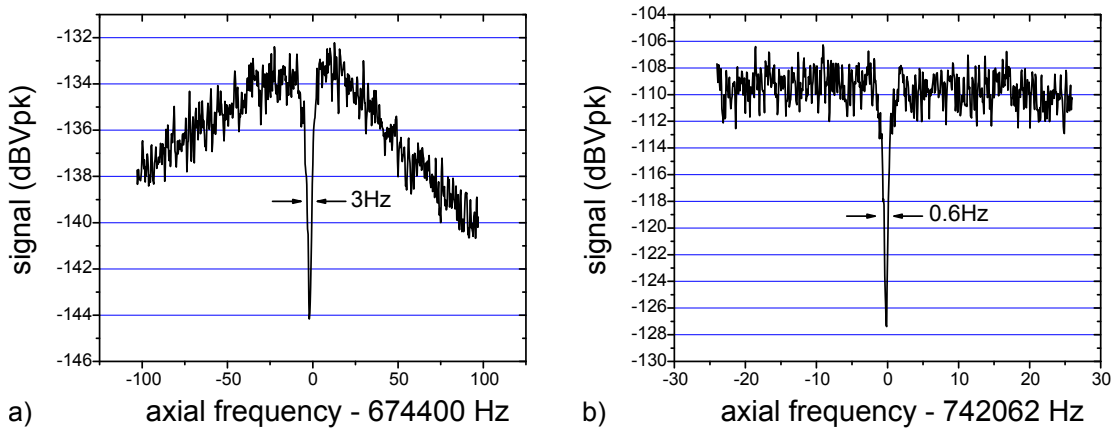

Figure 8.1: A single proton in resonance with the axial detection system in the magnetic bottle field of the analysis trap. Both spectra are obtained with an averaging time of $T = 80\,\mathrm{s}$. In a) the former axial detection system connected to both traps is utilized. The new tank circuit in b) is explicitly attached to the analysis trap (for parameters see Tab. 4.1). The new detection system is attached to the endcap instead of the correction electrode. Thus, despite the higher resonance resistance the line-width of the noise dip is decreased due to the higher effective electrode distance. The resonance frequencies of the different detection systems differ by 70 kHz, which requires an adjustement of the trapping potential.

the axial frequency is a significant improvement:
For the first time we were able to resolve individual spin transitions of a single proton (see section 8.6). Moreover, lower frequency fluctuations allow for a faster statistical determination of the Larmor frequency as discussed in section 8.7. But most important, the ability to resolve individual spin transitions allows for a direct determination of the Larmor frequency as described in section 3.5.2, which is demonstrated in section 8.7. The importance of this result for the g-factor measurement utilizing the double-trap technique is discussed in the last section.

8.1 Detecting the proton noise-dip

All measurements performed in the analysis trap are based on a measurement of the axial frequency. Thus, the very first task is to tune the proton in resonance with the detection system and detect the particle dip. Sample spectra of a single proton in thermal equilibrium with the former and the actual axial detection system are shown in Fig. 8.1.
However, the detection of the dip is hindered in the analysis trap since offset potentials play a much more important role than in the precision trap due to the smaller trap size. To tune the axial frequency of the proton in resonance with the detection system we have to apply a ring voltage of about $-1\,\mathrm{V}$, only. Offset potentials due to patch effects and thermal contact potentials are in the range of 100 mV [78]. Thus, the calculated values

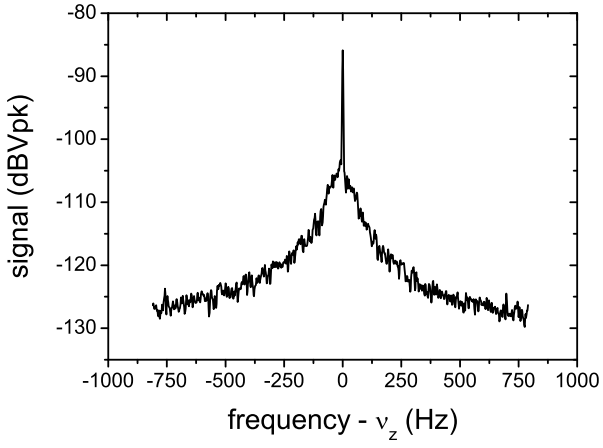

Figure 8.2: Frequency spectrum of a parametrically excited proton. The SNR is defined by the height of the peak with respect to the noise resonance of the tank circuit. The spectrum was recorded with 4 s averaging time.

for the ring voltage as well as the optimal tuning-ratio may significantly vary from the experimental values, which complicates the task of detecting the proton dip since we have to perform a two-dimensional scan:

- **Ring voltage:** The ring voltage is scanned in steps of 1 mV since the axial frequency has to match the resonance frequency of the detection system by ±200 Hz. Larger detunings than ±200 Hz lower the SNR of the dip signature which decreases the detectability.
- **TR:** To resolve the dip signature the tuning-ratio has to match the optimal tuning-ratio to at least 0.5 mUnits, corresponding to $c_4 = 24\,\mathrm{mm}^{-4}$. For larger anharmonicities the depth of the noise-dip decreases (see Eq. (7.2)).

A single dip-spectrum can be recorded in about 40 s implying that the whole scan would take several days.

We can speed up the scanning process by utilizing the $2\nu_z$-parametric-resonance of the axial mode. The phenomena of parametric excitation of an eigenmotion of a trapped particle in a Penning trap is discussed in detail in [79]. To excite the axial motion of the proton we apply a drive at $\nu_{rf} \approx 2 \cdot \nu_z$ to one endcap of the analysis trap. A peak at $\nu_{rf}/2$ on top of the noise resonance of the tank circuit as shown in Fig. 8.2 can be observed if the axial frequency of the proton is in the range $\nu_{rf}/2 \pm \epsilon$. The response width $2 \cdot \epsilon$ is defined by the strength h of the drive

$$2 \cdot \epsilon = \frac{1}{2}\nu_z \sqrt{h^2 - h_T^2} \quad , \tag{8.1}$$

where $h_T = \gamma_z/(\pi\nu_z)$ is the threshold amplitude above which parametric excitation occurs, which is proportional to the damping constant γ_z of the axial detection system. For

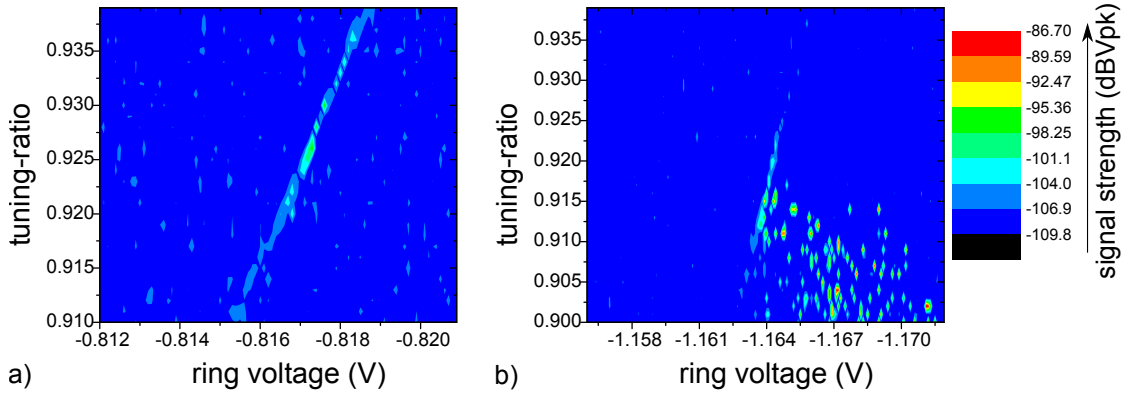

Figure 8.3: Plots of the signal strength of a parametrically excited proton. For each tuning-ratio, the ring voltage is changed in steps of 250 μV. The tuning-ratio is varied in steps of 1 mUnit. The scale of the z-axis is identical for both plots. In a) axial responses are visible over a wide range of the tuning-ratio but the ring-voltage A_3 has to match the condition $\nu_z(A_3) = \nu_{rf}/2$. The resonance voltage shifts as a function of the tuning-ratio due to the non-vanishing D_2-coefficient. The values for tuning-ratio and ring voltage for the maximum signal differ from the optimized values for the dip detection by $\Delta TR = 0.7$ mUnits and $\Delta A_3 = 0.15$ mV, respectively. In b) axial responses are not only visible for $\nu_z(A_3) = \nu_{rf}/2$ but also for smaller ring-voltages in case of a tuning-ratio which is smaller than the optimal tuning-ratio $TR_{\text{opt}} = 0.896$. For this scan, the optimized offset potentials $A_1 = -448.56$ mV, $A_2 = -21.977$ mV, $A_3 = -90$ mV and $A_4 = 21.977$ mV were applied, which correspond to a more symmetric potential than in a) (for more details see section 8.2).

stronger driving amplitudes than h_T the amplitude of the oscillation grows exponential. However, anharmonicities prevent the motion from expanding infinitely and lead to saturation of the motional amplitude. Thus, the particle can be monitored non-destructively. Due to the high SNR of the axial response we can detect a proton signal in less than 4 s compared to the 40 s required for the dip technique. A significant benefit of the parametric excitation is the low sensitivity on the tuning-ratio: We detect signals over a very wide range of the tuning-ratio which simplifies the first detection of a proton-signal. A two-dimensional scan of the ring voltage and the tuning-ratio utilizing the parametric excitation of the axial mode is shown in Fig. 8.3a). The maximum signal is obtained for a ring voltage of $A_3 = -0.817$ V and a tuning-ratio of $TR = 0.926$. Turning off the excitation, the dip signature becomes visible and after optimization of the tuning-ratio as described in section 7.1.1 the single proton dip is found for $A_3 = -0.81685$ V and $TR = 0.9253$ as shown in Fig.8.1a). The expected ring voltage A_3 and tuning-ratio TR can be extracted from analytical calculations of the trapping potential. The calculated values of $A_3 = -0.80659(3)$ V and $TR = 0.8821(2)$ deviate considerably from the experimentally determined values.

However, a more typical signature of a parametric scan in the analysis trap is shown in

Fig. 8.3b). Here, the maximum signals are obtained for tuning-ratios and ring voltages below the optimum, which is not yet understood. The only difference between Fig. 8.3a) and b) is the asymmetry of the trapping potential. However, the latter is recorded for the more symmetric potential (for further details on asymmetry see section 8.2). More detailed investigations showed that this effect is independent of the scanning-direction and the off-resonant-peaks are even visible for very low driving amplitudes near h_T. Still, we can estimate the optimum values of TR and A_3 quite well since the broadening is only present for tuning-ratios $TR < TR_{opt}$. The values for the ring voltage and the tuning-ratio obtained from Fig. 8.3b) differ by $\Delta A_3 = 0.1\,\mathrm{mV}$ and $\Delta TR = 0.1\,\mathrm{mUnits}$ only. This knowledge helped us to significantly reduce the time to find the dip signature in our analysis trap after the change of the setup. Instead of several months it took us only three days to tune the proton into resonance with our detection system and to resolve the dip signature.

8.2 Asymmetry optimization

As already discussed in section 8.1, the optimal tuning-ratio TR_{opt} and the resonance voltage $A3(\nu_z = \nu_{\mathrm{LC}})$ deviate significantly from the expected values. This is a first indicator for patch potentials on the trap electrodes. Most likely, these patch potentials also cause deviations of the *orthogonality* and the *compensation* which are key properties of a Penning trap. The design process of the analysis trap was focused on optimizing these two parameters to obtain a harmonic potential [47]. In this section, a scheme to detect and compensate the patch potentials in order to approximate the calculated potential is presented [47].

The basic principle is the detection and compensation of an asymmetry of our trapping

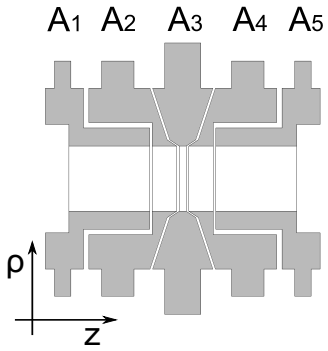

Figure 8.4: Sketch of the five-electrode analysis trap [46]. Asymmetries due to patch potentials on the electrodes are compensated by adjustement of offset voltages applied to the correction electrodes $A2$ and $A4$ and the endcap $A1$.

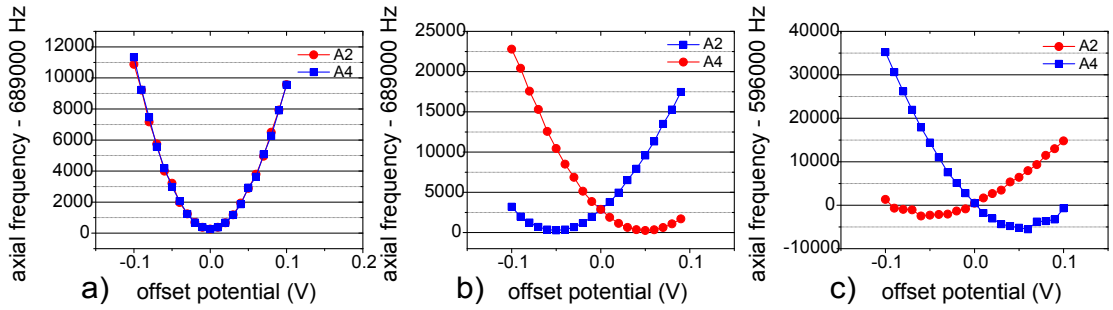

Figure 8.5: Calculated axial frequency shift as a function of an additional voltage applied to the correction electrodes $A2$ (red circles) and $A4$ (blue squares). For a symmetric potential in a) the curves are nearly symmetric (the deviation originates from the small but non-vanishing D_2-term) and equal. For a patch potential of $\delta_{A2} = -50\,\mathrm{mV}$ in b) the curves are shifted by δ_{A2} and $-\delta_{A2}$, respectively. A more complex configuration $\delta_{A2} = -50\,\mathrm{mV}$ and $\delta_{A5} = 350\,\mathrm{mV}$ is shown in c).

potential. To this end, we measure the axial frequency as a function of additional voltages applied to the correction electrodes $A2$ and $A4$ (see Fig. 8.4). Simulated curves for different patch potential configurations are shown in Fig. 8.5. For a symmetric potential (with respect to the ring electrode) the axial frequency shift as a function of an additional voltage applied to one correction electrode (or endcap) is positive and symmetric as shown in Fig. 8.5a). Moreover, in a symmetric potential the axial frequency shift is equal for both correction electrodes. In Fig. 8.5b) the simplest case for an asymmetric potential is shown. A patch potential present on one correction electrode shifts the curves. This can be compensated by application of an offset voltage to one correction electrode. An asymmetry scan for an even further disturbed potential is shown in Fig. 8.5c). The additional patch potential on the endcap cannot be compensated by offset voltages applied to the correction electrodes but requires an additional offset voltage applied to one endcap.
The experimental compensation process is performed in a smaller voltage range than the asymmetry-scans shown in Fig. 8.5 since the axial frequency can only be detected in a narrow range around the resonance frequency of the axial detection system. Experimental scans are shown in Fig. 8.6a)-c) where the voltages of the correction electrodes $A2$ and $A4$ have been varied by $800\,\mu\mathrm{V}$ only. We classify the grade of asymmetry by the slopes of the axial frequency as a function of the corresponding offsets $\Delta\nu_z^{A2}$ and $\Delta\nu_z^{A4}$. The compensation process depicted in Fig. 8.6 then basically consists of two optimization steps:

1. Voltage changes of the correction electrodes should cause the same frequency shifts $\Delta\nu_z^{A2} = \Delta\nu_z^{A4}$. Starting from a scan like Fig. 8.6a), additional voltages δ_{CE} are applied to the correction electrodes to achieve a configuration as shown in Fig. 8.6b). This configuration is called *local asymmetry compensated*.

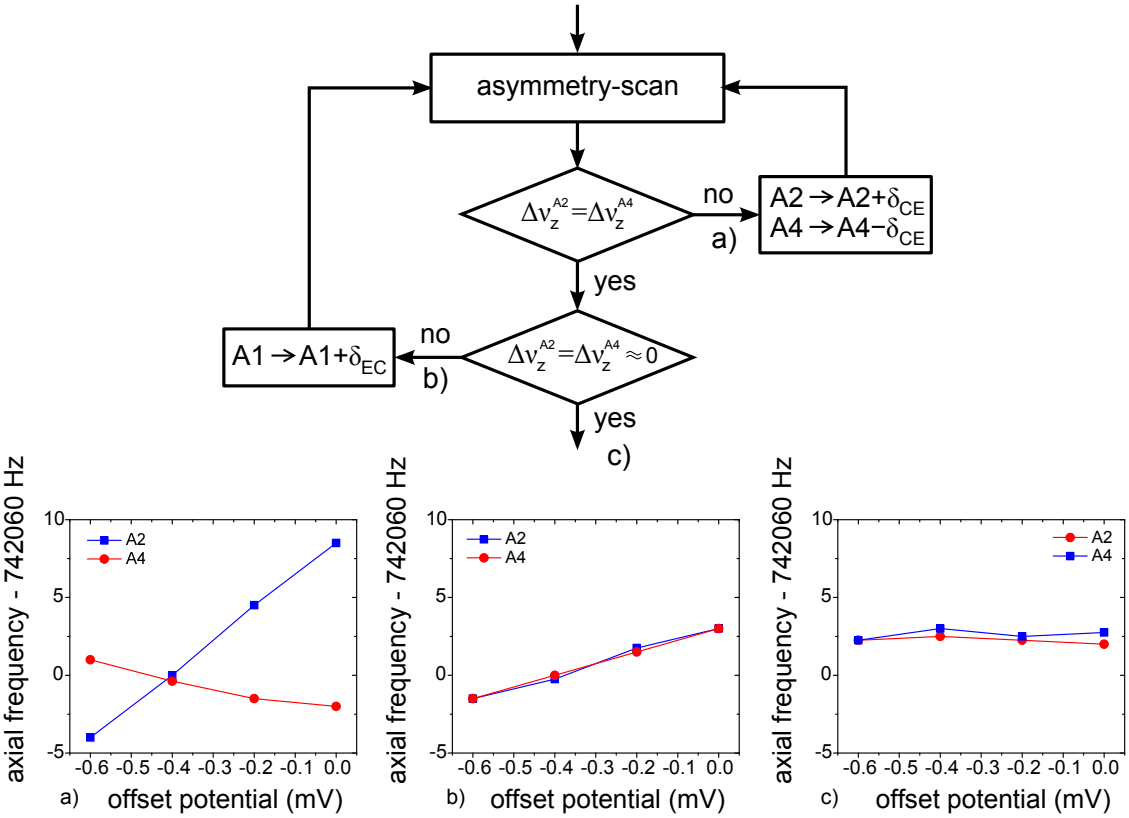

Figure 8.6: Top - Flow chart of the asymmetry compensation. Bottom - The corresponding asymmetry-scans: The axial frequency as a function of an additional voltage applied to the correction electrodes $A2$ (red) and $A4$ (blue) is shown. The slopes $\Delta\nu_z^{A2}$ and $\Delta\nu_z^{A4}$ are determined from a linear fit to the data. In a) the slopes differ, indicating an asymmetric potential. Due to an additional offset potential δ_{CE} applied to the correction electrodes the slopes in b) are equal, indicating a *local asymmetry compensated* trap. In c) the vanishing slopes indicate a *global asymmetry compensated* trapping potential.

2. Voltage changes of the correction electrodes should cause small frequency shifts $\Delta\nu_z^{A2} = \Delta\nu_z^{A4} \approx 0$. This can be achieved by additional offset potentials applied to the endcaps. The endcaps are usually kept on ground potential to achieve a stable trapping potential. Thus, we apply only one offset voltage δ_{EC} to $A1$ utilizing an ultra-stable *Fluke 343A* voltage source to minimize instabilities due to the additional voltage supply. In Fig. 8.7 the slope $\Delta\nu_z^{A2}$ for each *local asymmetry compensated* configuration as a function of the offset δ_{EC} is shown. The asymmetry-scan shown in Fig. 8.6c) corresponds to the *global asymmetry compensated* configuration for $\delta_{\mathrm{EC}} = -300\,\mathrm{mV}$ for the red data points.

Besides the information of $\Delta\nu_z^{A2}$, we obtain for each data point of Fig. 8.7 values for the orthogonality D_2, the optimal tuning-ratio TR_{opt} and the resonance voltage $A3(\nu_z = \nu_{\mathrm{LC}})$ [46]. Comparing these values with calculations as shown in Fig. 8.5 indicated, that the electrostatic deviations cannot be explained by patch potentials, only. We assume that

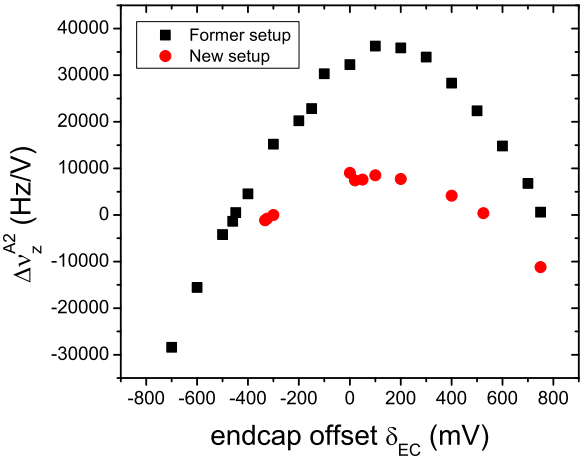

Figure 8.7: The graph shows the slope $\Delta\nu_z^{A2}$ of the *local asymmetry compensated* configurations as a function of the endcap offset δ_{EC}. The black squares were obtained for the former setup. Due to an improved setup of the analysis trap, the *global asymmetry compensated* configuration is achieved for lower offset potentials δ_{EC}. This indicates a less disturbed potential in the new setup.

a larger gap between one endcap and the adjacent correction electrode additionally disturbed the electrostatic potential. Thus, for the new setup we took even more care when setting up the electrodes of the analysis trap. The comparison of $\Delta\nu_z^{A2}(\delta)$ for the former setup and the new setup shown in Fig. 8.7 indicates that we improved the geometric properties of the analysis trap considerably.

8.3 Measurement of radial frequencies

At first glance, the routine for the g-factor measurement (see section 3.4) only requires measurements of the axial frequency. However, to determine the Larmor frequency to drive spin transitions, the magnetic field strength has to be determined which calls for a measurement of ν_+ and ν_- in addition. Moreover, a measurement of ν_c as a function of the axial position of the proton in the analysis trap yields the strength of the magnetic bottle.

The application of the double-dip technique to measure the radial frequencies is not possible in the strong magnetic inhomogeneity: The motional amplitude of the axial mode is thermally broadened since it is in contact with a thermal bath. In the presence of a coupling field $\nu_{rf} = \nu_z \pm \nu_{\mp}$, the energy of the radial mode is not constant over time too. Consequently, the axial frequency itself fluctuates due to the strong dependence on the temperature in the radial modes. In case of the magnetron mode this would lead to

frequency fluctuations up to $\delta\nu_z = 50\,\mathrm{Hz}$ which is orders of magnitude larger than the line-width of the noise dip. For the modified cyclotron mode the corresponding axial frequency fluctuations would be $\delta\nu_z = 5\,\mathrm{kHz}$. However, we can utilize these energy-dependent shifts of ν_z to determine the radial frequencies with a different measurement scheme. The measurement consists of a series of burst signals to excite the radial modes. After each excitation attempt the axial frequency is measured. For a resonant excitation the frequency difference between two subsequent axial frequency measurements is large due to energy absorption in the radial mode. As discussed in section 3.2 the linewidth of the modified cyclotron resonance is defined by the temperature of the axial mode. We apply negative feedback to the axial detection system to decrease the thermal broadening of the resonance. Fig. 8.8 shows two measurements of the modified cyclotron frequency. The measurement in Fig. 8.8a) was performed with our new axial detection system. Due to the improved SNR, we reach lower axial temperatures, which reduces the linewidth of the modified cyclotron resonance. Moreover, the spectral width $\Delta\nu_{rf}$ of the excitation pulse was decreased to approximately half the width of the modified cyclotron resonance by increasing the number of burst cycles and thus the puls length. These changes lead to a narrower response compared to the former detection, shown in in Fig. 8.8b), where axial frequency fluctuations are observed over a wide range of the excitation frequency. We give a conservative error of twice the resonance width $2 \cdot \Delta\nu_+$ yielding a relative uncertainty of $1.5 \cdot 10^{-4}$ for the modified cyclotron frequency. We applied the same method to determine the magnetron frequency to $\nu_- = 15.39(1)\,\mathrm{kHz}$.

8.3.1 Magnetic bottle measurement

We utilize the measurement scheme for ν_+ to scan the magnetic bottle field of the analysis trap. To this end, we shift the position of the proton along the symmetry axis of our trap by additional asymmetric potentials applied to the correction electrodes. The minimum of the electrostatic potential for each configuration can be analytically calculated giving the position of the proton. At each position we measure ν_+ and ν_z to determine the free cyclotron frequency ν_c by application of the invariance theorem (Eq. (2.8)). The magnetron frequency is measured the same way as the modified cyclotron frequency. But it is sufficient to measure ν_- for one position of the proton in the magnetic bottle. In Fig. 8.9 the magnetic field strength as a function of the axial position is shown. From a quadratic fit to the data the strength of the magnetic bottle term was determined $B_2 = 297(10)\,\mathrm{mT/mm^2}$, which is in perfect agreement to the theoretical value of $B_2 = 300.3807(63)\,\mathrm{mT/mm^2}$ [47].

8.4 Temperature of eigenmodes

The strong scaling of the axial frequency on the radial energies in the AT implies that the axial mode can be utilized as a *thermometer* of the radial temperatures T_+ and T_-.

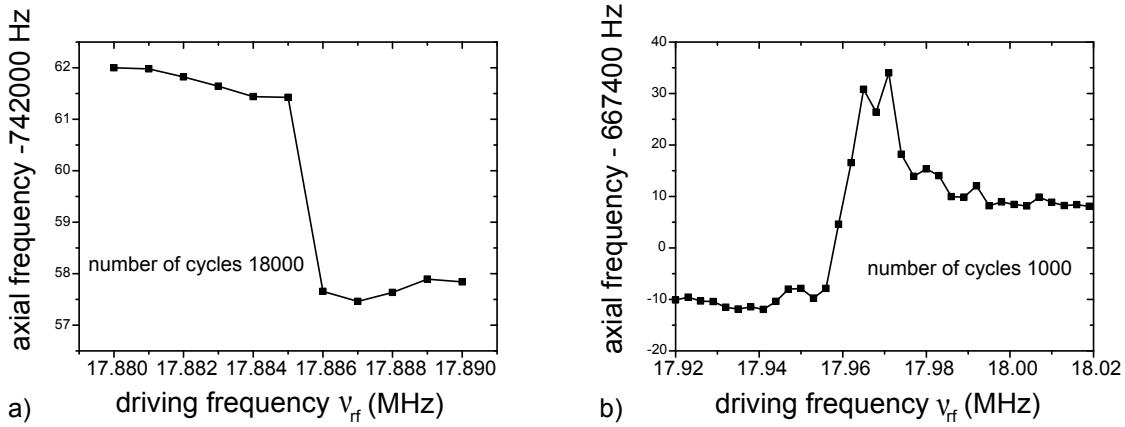

Figure 8.8: Successive measurements of the axial frequency to determine the modified cyclotron frequency in the magnetic bottle. An external driving field at ν_+ is applied between two subsequent axial frequency measurements. On resonance the energy in the modified cyclotron mode is changed which causes an axial frequency shift. In a) the axial temperature was reduced by negative feedback to a temperature of $T_z \approx 0.8\,\mathrm{K}$. This yields a linewidth of the modified cyclotron resonance of $\Delta\nu_+ \approx 1.4\,\mathrm{kHz}$. The spectral width of the excitation pulse was chosen to be of the order of $\Delta\nu_+$ by choosing an appropriate number of cycles of the burst signal. Thus, a single response is observed. The curve shown in b) was measured with the former axial detection system. The temperature was decreased to $T_z \approx 2.2\,\mathrm{K}$ resulting in a linewidth of $\Delta\nu_+ \approx 3.8\,\mathrm{kHz}$. Here, the width of the driving field, defined by the number of cycles of the pulse, is about a factor of five larger than $\Delta\nu_+$, which results in a broad response. Negative frequency jumps correspond to a decrease of the cyclotron energy, which is at first glance an unexpected result. However, the driving field does not necessarily cause an increase of the energy in the cyclotron mode: An energy change in the cyclotron mode leads to an instant change of the oscillation frequency due to the strong magnetic bottle. This means that the drive is resonant to the cylotron mode for a very short time. Thus, the phase difference of the driving field with respect to the phase of the cyclotron motion has to be considered. This can either result in an increase or a decrease of the cyclotron radius.

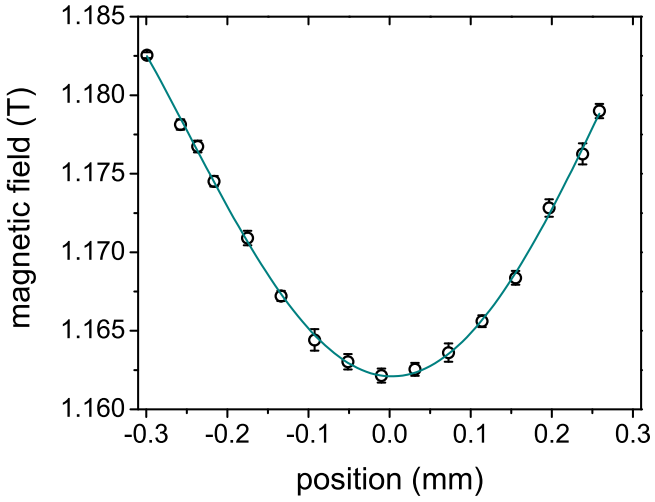

Figure 8.9: Measurement of the magnetic bottle field [47]. The proton is shifted in axial direction by application of asymmetric potentials to the correction electrodes. For each configuration the displacement is calculated analytically and the free cyclotron frequency is measured. From a parabola fit to the data a magnetic bottle strength of $B_2 = 297(10)\,\mathrm{mT/mm^2}$ was obtained.

The knowledge of the magnetic bottle strength B_2 gives the scaling of the axial frequency according to Eq. (3.6) as $\Delta\nu_z = 72\,\mathrm{Hz/K}$. Thus the absolute axial frequency is given by

$$\nu_z(T_+, T_-) = \nu_z(T_+ = 0\mathrm{K}, T_- = 0\mathrm{K}) + 72\,\mathrm{Hz/K} \cdot T_+ + 72\,\mathrm{Hz/K} \cdot T_- \quad . \tag{8.2}$$

We will see in section 8.5 that the temperatures of the radial modes play a very important role for the axial frequency stability. Thus, an absolute temperature calibration as given by Eq. (8.2) helped us to investigate the systematics of the axial frequency fluctuations in the analysis trap.
The first application of the *thermometer* is the measurement of the **magnetron temperature**. To this end, we couple the magnetron mode to the axial mode by a sideband drive at frequency $\nu_z + \nu_-$. Due to energy exchange the axial frequency fluctuates since the temperature T_-, according to T_z, is Boltzmann-distributed in the presence of the coupling field. However, after turning off the coupling field, an axial frequency measurement reflects one specific temperature of this thermal distribution. In Fig. 8.10 two successive axial frequency measurements separated by a resonant coupling of ν_z and ν_- are shown. The frequency difference of about 6 Hz corresponds to a magnetron temperature difference of 83 mK. Plotting a histogram of a series of axial frequency measurements as shown in Fig. 8.11 gives several informations:

- We obtain the axial frequency for vanishing temperature in the magnetron mode from the lower cutoff of the distribution $\nu_{z,min} = \nu_z(T_- = 0\mathrm{K})$. Thus, we can deduce the absolute temperature T_- from an axial frequency measurement.

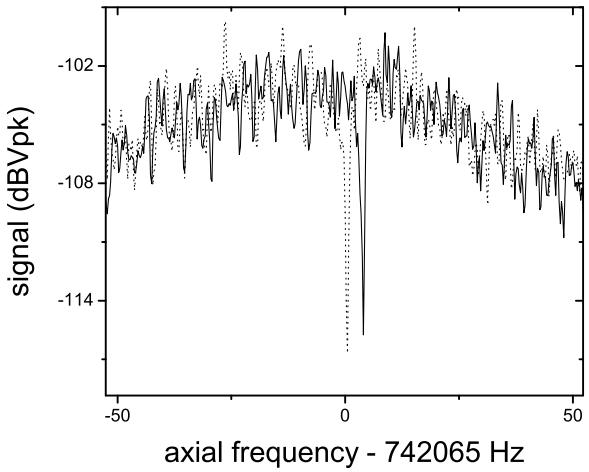

Figure 8.10: Two axial frequency spectra of a single proton in the analysis trap. The frequency difference arises from a sideband-coupling of magnetron and axial mode. The dotted curve corresponds to a 83 mK lower temperature in the magnetron mode than the solid curve.

- The temperature of the axial mode can be calculated from the width of the distribution according to Eq. (8.2). The left y-axis of Fig. 8.11 shows the axial frequency shift and the right y-Axis shows the corresponding temperature of the magnetron mode. The axial temperature can be calculated by the relation $T_z = \nu_z/\nu_- \cdot T_-$.

We obtain a temperature of $T_z = 8.23(0.61)\,\mathrm{K}$ for the axial detection system without any feedback (Fig. 8.11b)). By application of negative feedback we can reduce this temperature by almost a factor of ten to $T_z = 1.06(0.22)\,\mathrm{K}$, which corresponds to a magnetron temperature of $T_- = \nu_-/\nu_z \cdot T_z = 22\,\mathrm{mK}$, only. This is an improvement of more than a factor of two compared to the previous setup where a temperature of $T_z = 2.22(0.19)\,\mathrm{K}$ was achieved [47].
The second application of our *thermometer* is the measurement of the **modified cyclotron temperature**. At first we measure the thermal distribution of the modified cyclotron mode in our analysis trap in the same way as for the magnetron mode. However, the modified cyclotron mode is thermalized in the precision trap due to the coupling to the dedicated detection system. This means, that each data point of the distribution requires an exchange of the proton between both traps for thermalization (PT) and temperature measurement (AT) which is much more time consuming than for the magnetron mode. Moreover, the higher temperature of T_+ compared to T_- complicates the detection of $\nu_z(T_+)$. The magnetron temperature is reduced due to the coupling to the axial mode by $\nu_z/\nu_- \approx 50$. Thus, the distribution of the axial frequency is less than 50 Hz (see Fig. 8.11b)) which is less than the width of the resonator. For the modified cyclotron mode, axial frequency differences up to 2 kHz (corresponding to $\Delta T_+ = 28\,\mathrm{K}$)

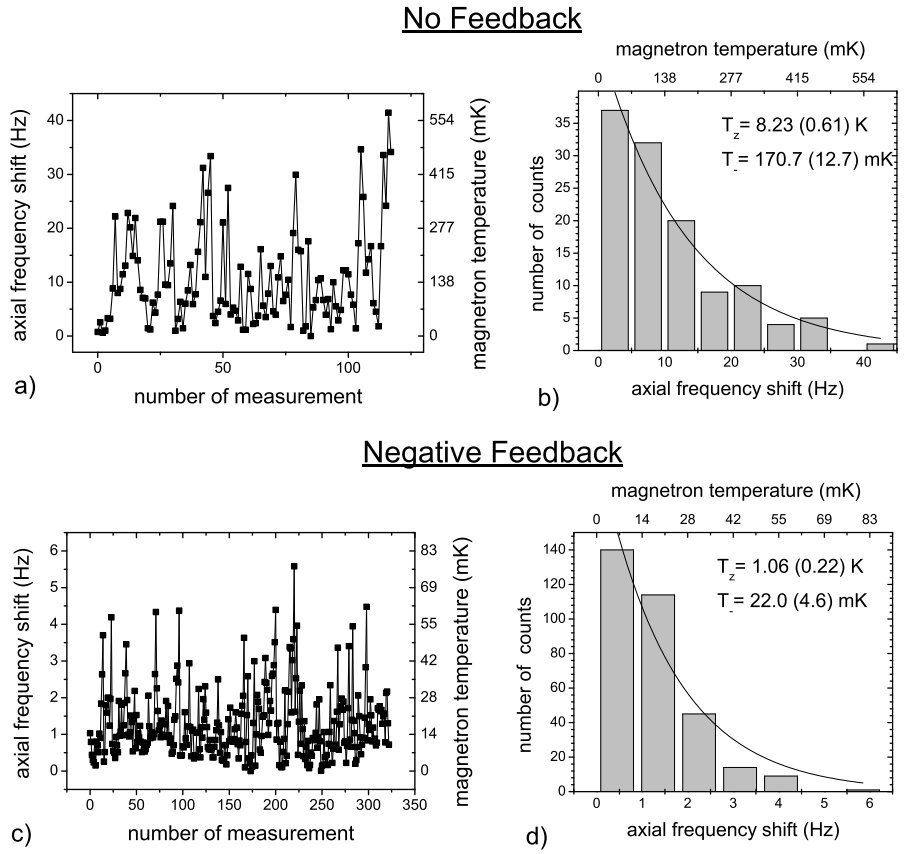

Figure 8.11: Measurement of the magnetron temperature and the temperature of the axial detection system without feedback (top) and with negative feedback (bottom) applied to the axial detection system. On the left, successive axial frequency measurements separated by a resonant coupling of magnetron and axial mode at $\nu_z + \nu_-$ are shown. Note the factor of 10 difference in scaling.t'Every axial frequency measurement corresponds to a certain magnetron temperature according to Eq. (8.2). In b) and d) the distribution of axial frequency shifts is shown, which directly maps the thermal distribution of the axial mode. The average magnetron temperature is obtained from an exponential fit to the data (solid line). The corresponding axial temperature can be calculated by the relation $T_z = \nu_z/\nu_- \cdot T_-$.

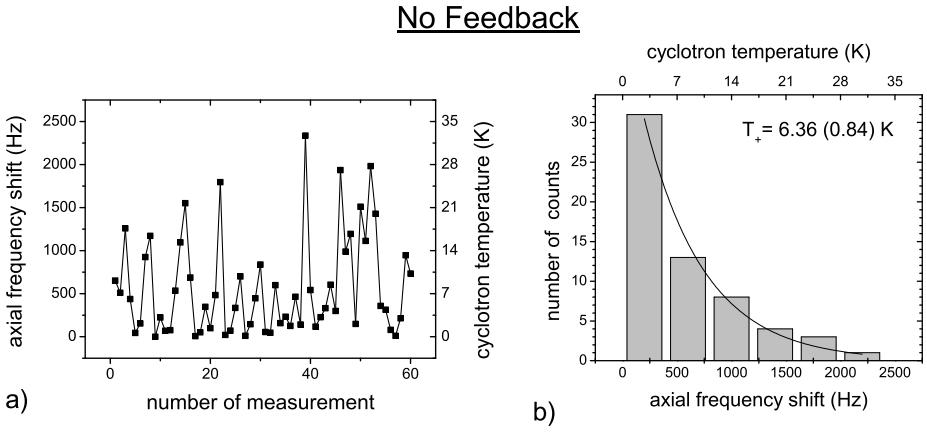

Figure 8.12: Measurement of the temperature of the cyclotron detection system without feedback. The frequency measurement is conducted in the analysis trap. Thermalization takes place in the precision trap. A waiting time of $5 \cdot \tau_+$ assures thermalization in the precision trap where τ_+ is the cooling time constant. Every axial frequency measurement corresponds to a certain cyclotron temperature according to Eq. (8.2). The right graph shows the distribution of axial frequency shifts, which directly maps the thermal distribution of the modified cyclotron mode. The temperature of $T_+ = 6.36(0.84)$ is obtained from an exponential fit to the data (solid line).

are expected. Thus, in order to measure $\nu_z(T_+)$ we have to readjust the ring voltage for each energy E_+ to tune the particle in resonance with our detection system. Results of a cyclotron temperature measurement are shown in Fig. 8.12. The 60 data points were acquired in about 26 hours giving a temperature for the detection system for the modified cyclotron frequency of $T_+ = 6.36(0.84)\,\mathrm{K}$. This temperature can be further reduced by application of negative feedback similar as described above for the axial detection system. However, due to unwanted parasitic effects at the high resonance frequency of the cyclotron detection system and the lower SNR, the temperature could only be reduced to $T_+ = 3.15(0.11)\,\mathrm{K}$ [45].

Summarizing, a proton arriving in the analysis trap can first be cooled in the magnetron mode by a sideband coupling drive to the axial mode. By application of negative feedback to the axial detection system we can reliably cool the magnetron mode to a temperature of less than $T_- < 50\,\mathrm{mK}$ in a few minutes. Having achieved a magnetron temperature of a few mK, the axial frequency directly reflects the temperature of the modified cyclotron mode (see Fig. 8.12).

8.5 Axial frequency stability in the magnetic bottle

The main experimental challenge is the determination of the spin state of the proton in the analysis trap. The tiny frequency jump of $\Delta\nu_{\mathrm{z,SF}} = 172\,\mathrm{mHz}$ due to a spin transition requires a very stable axial frequency. As discussed in section 3.5 we quantify the instability Ξ of the axial frequency by the standard deviation of two subsequent axial frequency measurements. The optimal case is an absolutely stable axial frequency corresponding to $\Xi = 0\,\mathrm{Hz}$. However, as discussed in section 3.5, a stability of the order of the size of a frequency jump due to a spin flip $\Xi \approx \Delta\nu_{\mathrm{z,SF}}$ already allows for a statistical determination of the Larmor frequency. For even lower fluctuations $\Xi < \Delta\nu_{\mathrm{z,SF}}$, the successful detection of individual spin transitions becomes accessible which is the main frontier towards a sub-ppb-determination of the g-factor. However, the first series of axial frequency measurements performed in the analysis trap showed a large instability of $\Xi(T = 80\,\mathrm{s}) = 1.8\,\mathrm{Hz}$. In this section, the investigations of the origin of these fluctuations and the improvements are discussed.
The axial frequency in the magnetic bottle is defined by the electrostatic potential (Eq. (2.16)), the radial energies (Eq. (3.6)) and the spin state (Eq. (3.18)):

$$\begin{aligned}\nu_z &= \frac{1}{2\pi}\sqrt{\frac{2qV_0c_2}{m_p}} + \frac{1}{2\pi\sqrt{2qV_0c_2m_p}}\frac{B_2}{B_0}\left(E_+ + |E_-|\right) \pm \frac{g\mu_N B_2}{\sqrt{2qV_0c_2m_p}} \\ &= \nu_{\mathrm{z},0} + \frac{1}{4\pi^2\nu_{\mathrm{z},0}m_p}\frac{B_2}{B_0}\left(E_+ + |E_-|\right) \pm \frac{g\mu_N B_2}{2\pi\nu_{\mathrm{z},0}m_p} \quad . \end{aligned} \tag{8.3}$$

The expected limitations of the frequency stability due to the electrostatic contribution can be determined from the voltage stability of the *UM1-14LN*-supply (see section 5.5). Moreover, since we utilize the same voltage source to bias both traps, we can also estimate the axial frequency fluctuations in the analysis trap due to voltage fluctuations from the measured instability of the axial frequency in the precision trap (see section 7.1.3). However, the observed fluctuations in the analysis trap were more than one order of magnitude larger than expected. We therefore concluded that radial energy fluctuations were responsible for the large instabilities since the large magnetic inhomogeneity is the main difference between both traps. Thus, the main experimental task is to avoid any changes of the energy of the magnetron mode and the modified cyclotron mode.

To further clarify the origin and to obtain a scaling of the large axial frequency fluctuations mentioned above we performed systematic studies on the axial frequency stability. Here, the transient recorder presented in section 4.6 revealed its power as a tool to measure the axial frequency fluctuation Ξ as a function of the averaging time T. We will first discuss the influence of the modified cyclotron mode temperature on the frequency stability. Fig. 8.13a) shows measurements of $\Xi(T)$ for different energies in the modified cyclotron mode. For each cyclotron temperature we observe an increase of Ξ with $\sqrt{T}$, which we attribute to quantum jumps in the modified cyclotron mode. In [45], a quantum mechanical model is given relating the quantum transitions in the modified cyclotron mode to a driving field with amplitude E_0:

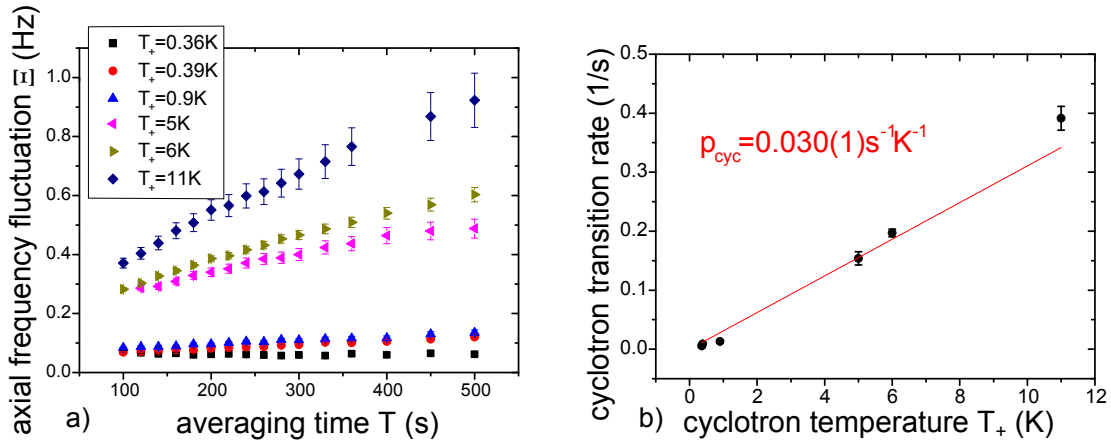

Figure 8.13: a) Axial frequency fluctuation Ξ as a function of the averaging time T for different temperatures of the modified cyclotron mode. The data was obtained from measurements of the real-time signal of the axial detection system utilizing the transient recorder. b) The rate of quantum transitions in the modified cyclotron mode is plotted as a function of the temperature of the modified cyclotron mode.

The transition amplitude between two states $|n_+\rangle$ and $|n_+ \pm 1\rangle$ is given by

$$\begin{aligned} \Gamma_{n_+ \to n_+ \pm 1} &= \langle n_+ | qE_0 \rho_+ | n_+ \pm 1 \rangle \\ &= qE_0 \sqrt{\frac{\hbar}{m\omega_+} \frac{n_+}{2}} \quad , \end{aligned} \tag{8.4}$$

where in the last step the valid approximation $n_+ \gg 1$ was used, which means that the transition amplitudes for $|n_+\rangle \to |n_+ - 1\rangle$ and $|n_+\rangle \to |n_+ + 1\rangle$ are equal. The evolution of the axial frequency can be described by a random walk with standard deviation

$$\Xi(T) = \sqrt{p_{\mathrm{cyc}} T \Delta\nu_{z,+}^2} \quad , \tag{8.5}$$

where $\Delta\nu_{z,+}$ is the size of the axial frequency jump due to one quantum transition in the modified cyclotron mode and p_{cyc} is the transition rate. Eq. (8.5) describes the observed scaling of Ξ with $\sqrt{T}$. From the dataset shown in Fig. 8.13a) we obtain the scaling of the transition rate p_{cyc} as a function of the temperature of the modified cyclotron mode. As shown in Fig. 8.13b) the transition rate scales linearly with T_+, as expected from Eq. (8.4). A temperature dependence of the transition rate of $p_{\mathrm{cyc}}/T_+ = 0.030(1)\,\mathrm{s}^{-1}\mathrm{K}^{-1}$ is obtained from a linear fit to the data.

This transition rate can be used to quantify the strength E_0 of the driving field. If we assume E_0 to be a white-noise driving field with constant amplitude over the linewidth of the modified cyclotron resonance $\Delta\nu_+$, the transition rate p_{cyc} is obtained from Fermi's golden rule

$$p_{\mathrm{cyc}} = \Delta\nu_+ \frac{2\pi}{\hbar} \rho(E_+) \Gamma_{i\to f}^2 \quad . \tag{8.6}$$

Here $\rho(E_+) = 1/\hbar\omega_+ = \text{const.}$ is the density of states of the one-dimensional harmonic oscillator. We obtain an amplitude of $E_0 = 7\,\mathrm{nV}/\sqrt{\mathrm{Hz}}$ which illustrates the sensitivity of

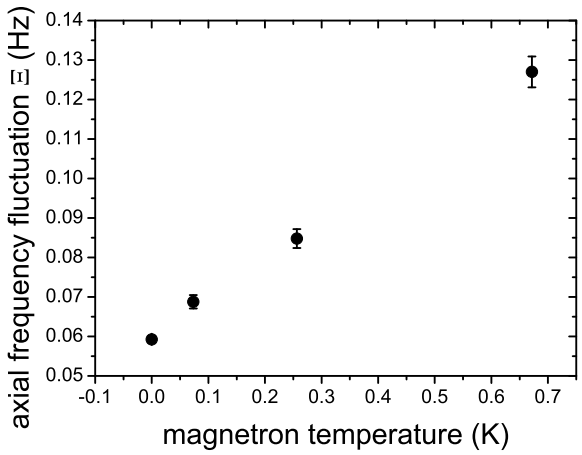

Figure 8.14: Axial frequency fluctuation as a function of the magnetron mode temperature T_-. The magnetron mode is thermalized by a sideband-coupling to the axial mode. By application of strong negative feedback to the axial detection system, we are able to reach temperatures of $T_- = 22\,\mathrm{mK}$ on average as shown in Fig. 8.11. For further discussion see text.

the modified cyclotron mode.

Energy fluctuations in the magnetron mode are also of concern but less important as we will see. Fig. 8.14 shows the axial frequency fluctuation for different temperatures in the magnetron mode. We also observe an increasing instability as the energy in the magnetron mode is raised. However, we are able to cool the magnetron mode reliably to temperatures of only several mK (see Fig. 8.11). Moreover, the magnetron radius itself is very stable which means that the magnetron temperature varies only by a few mK over a period of several days. We therefore concluded that the observed instabilities of the axial frequency scale with the magnetron temperature but are caused by cyclotron quantum jumps. Thus, the contribution of the magnetron mode to the axial frequency fluctuation can be neglected - if the mode is properly cooled.
Summarizing, the following informations on the origin and scaling of the axial frequency fluctuations were obtained:

1. The fluctuations increase with the absolute radial energy.

2. The fluctuations mainly arise from spurious quantum jumps in the cyclotron mode.

3. The fluctuations are caused by a white noise drive.

t' In order to increase the axial frequency stability, the amplitude E_0 of the driving field has to be minimized. Due to the tiny magnitude of the noise field we are not able to measure E_0 with a classical spectrum analyzer. This means, that the success of a change of any parameter can only be judged by a measurement of Ξ. It was found that for a reproducible

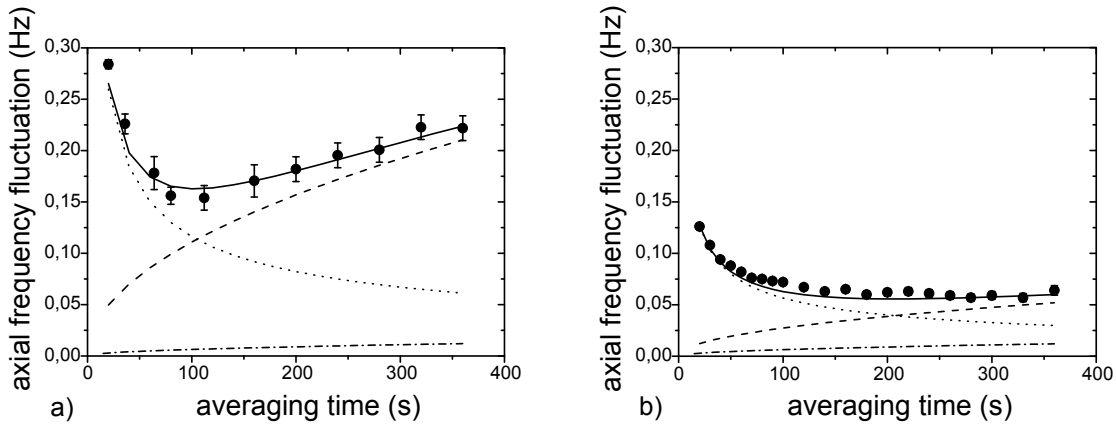

Figure 8.15: Frequency fluctuation of the axial mode as a function of the FFT-averaging time for the former setup in a) and the new setup in b). The differences of the apparatus are discussed in section 5.7. The decreasing dotted curve corresponds to the frequency uncertainty due to noise averaging of the FFT-spectrum. The dashed curve corresponds to noise driven quantum jumps in the cyclotron mode at a rate of $0.026\,\mathrm{s}^{-1}$ for a) and $0.002\,\mathrm{s}^{-1}$ for b), respectively. The contribution of voltage fluctuations (dashed dotted line) was obtained from the measured frequency stability in the precision trap. The solid line represents the sum of the three contributions which approximates the experimental data (black circles) very well.

result, we have to take data for about eight hours with the transient recorder.
The main aspects to avoid a noise drive at the trap electrodes are listed in [45] and [46]. A stability as shown in Fig. 8.15a) was reached which allowed for a statistical detection of the Larmor resonance as described in section 3.5.1. In order to suppress the driving field even more, we changed the whole apparatus as described in section 5.7. With these changes, we were able to reduce the transition rate p_{cyc} by about a factor of four compared to the rate $p_{\mathrm{cyc}}(T_+ = 1\,\mathrm{K}) = 0.125(21)\,\mathrm{s}^{-1}$ of the former setup. Moreover, due to the improved detection systems the contribution to Ξ by noise averaging of the FFT-spectrum is significantly lowered [57]. Thus, we are able to resolve the dip signature in less averaging time which further reduces the observed axial frequency fluctuation.
Having achieved this level of stability we investigated the influence of an asymmetric trapping potential on the axial frequency stability. To this end, $\Xi(T)$ was measured for different offsets applied to the endcap $A1$ which is shown in Fig. 8.16. For each offset ΔA_1, the correction electrodes are tuned to achieve a *local asymmetry compensated* potential as described in the previous section. The *global asymmetry compensated* configurations for $\Delta A_1 = -300\,\mathrm{mV}$ and $\Delta A_1 = +525\,\mathrm{mV}$ correspond to the potential configurations which approximate the calculated potential best. However, the best stability is obtained for $\Delta A_1 = 0\,\mathrm{mV}$. We assume that voltage fluctuations of the additional voltage supply to bias A_1 decrease the frequency stability and therefore keep A_1 at ground potential for all further measurements.

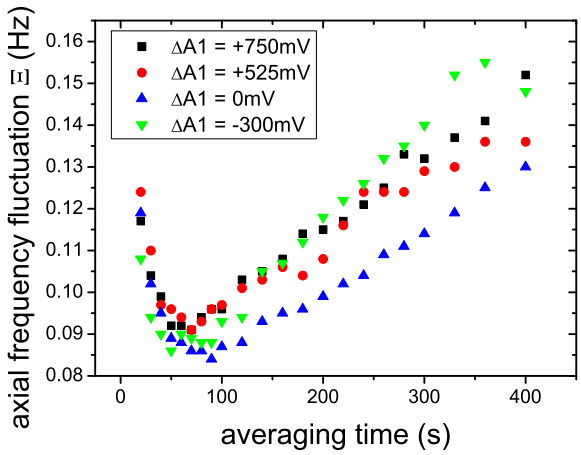

Figure 8.16: Axial frequency fluctuation as a function of the FFT-averaging time for different offset-voltages applied to the endcap A_1. For each offset ΔA_1, the trap is *local asymmetry compensated* by application of appropriate offset-voltages to the correction electrodes. For the offsets $\Delta A_1 = -300\,\mathrm{mV}$ and $\Delta A_1 = +525\,\mathrm{mV}$ the trap is *global asymmetry compensated*. However, the best stability is obtained for $\Delta A_1 = 0\,\mathrm{mV}$ which indicates that the additional voltage source to bias A_1 has a negative influence on the axial frequency stability.

Summarizing, we [1] achieved a frequency stability of $\Xi = 60\,\mathrm{mHz}$. This is about one third of a frequency jump due to a spin flip, which implies that the detection of individual spin transitions is possible as presented in the following section.

8.6 Individual spin transitions

In order to detect spin flips the axial frequency is repeatedly measured for an averaging time of $T = 90\,\mathrm{s}$. Spin transitions are induced after twelve successive axial frequency measurements. To this end, a resonant rf-field is applied to the disc coil attached to the trap tower to generate the required radial B-field as shown in Fig. 8.17. The signal is generated by an *RS SMB 100A* signal generator followed by an *RS HVV10* power amplifier. Both devices are turned off during axial frequency measurements. The proton is further protected from the output noise of the power amplifier by an additional relay. A bandpass chain consisting of two *MC BLP-70+* low-pass filters and two *MC BLP-50+* high-pass filters is used to suppress unwanted sidebands. The amplitude of the rf-signal at the room-temperature flange is $+27\,\mathrm{dBm}$ at a frequency of $\nu_{\mathrm{rf}} = 50.0\,\mathrm{MHz}$. The duration of $t_0 = 10\,\mathrm{s}$ is chosen to saturate the transition implying that a spin flip probability of $P_{\mathrm{SF}} = 50\%$ is achieved.

[1] The presented optimization of the axial frequency stability and the detection of individual spin transitions is also part of the Ph.D.-thesis of Andreas Mooser [57]

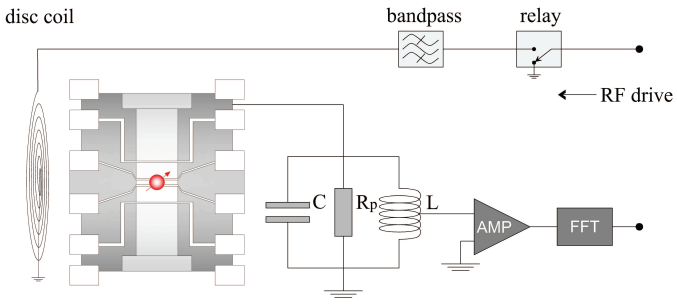

Figure 8.17: Experimental setup to drive spin transitions [46]. The radial magnetic field is generated by an rf-drive applied to the disc coil next to the analysis trap. For details of the signal chain see text.

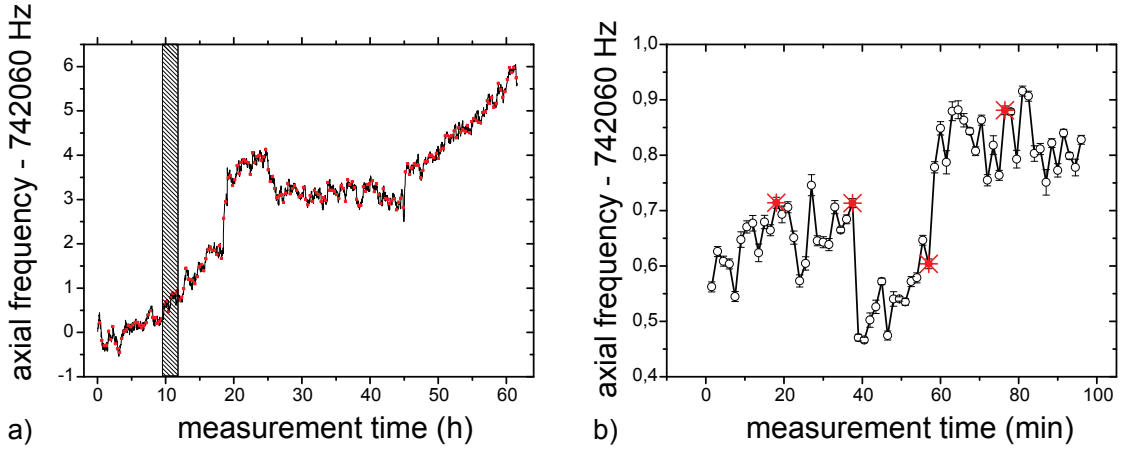

Figure 8.18: Axial frequency as a function of time. In a) the whole measurement sequence is shown. Spin flip attempts after twelve successive axial frequency measurements are indicated by the red datapoints. The interval of the dashed area is shown in b) in detail. Spin flips are induced after the crossed datapoints. The two large frequency jumps indicate spin transitions which allows us to directly determine the spin orientation of a single proton for the first time.

Fig. 8.18a) shows the evolution of the axial frequency as a function of time for a period of about 60 hours. The red datapoints indicate spin flip attempts. A zoom of the dashed interval is shown in Fig. 8.18b). The spin flip drive was turned on after the crossed datapoints. Two large frequency jumps are visible after a spin flip attempt which can be unambiguously assigned to spin transitions. The size of the frequency jump of $-180(10)$ mHz perfectly agrees with the expected value of 171 mHz. Moreover, the assumption that the first frequency jump is caused by a change of the spin state from 'down' to 'up' is confirmed by an opposite second frequency jump of 181(12) mHz, where the spin flips back from 'up' to 'down'. This is the first detection of individual spin transitions of a single proton.

The sequence shown in Fig. 8.18b) is the clearest signature for individual spin transitions in the whole dataset of Fig. 8.18a). So the question arises how significant the frequency jumps for the remaining spin flip attempts are. The framework discussed in section 3.5.2

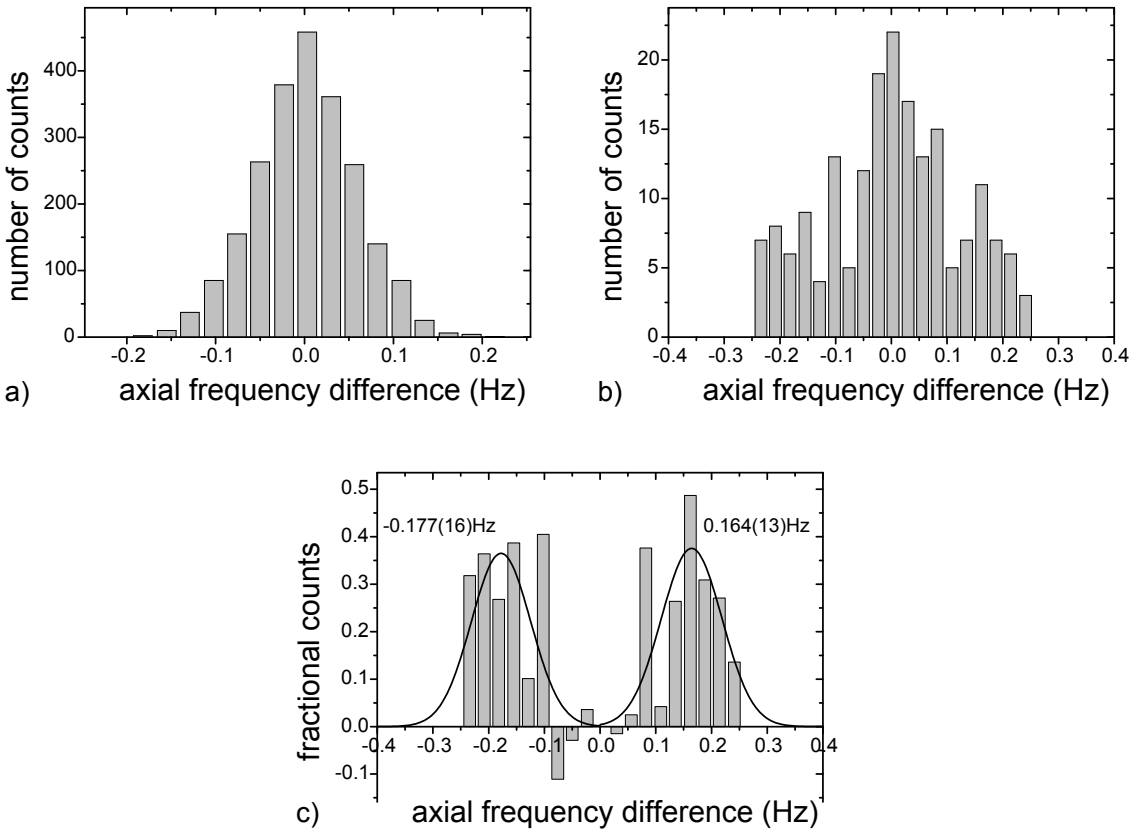

Figure 8.19: Distribution of axial frequency differences. a) shows the distribution when no spin flip drive was applied. b) shows the distribution for spin flip attempts. The statistics are a factor of twelve lower than in a). For the distribution shown in c) the normalized distributions a) and b) were subtracted. The position of the maxima of the two distributions agree with the expected size of an axial frequency jump due to a spin flip $\Delta\nu_{\mathrm{z,SF}} = 171\,\mathrm{mHz}$.

gives a very precise answer of how many spin transitions are detected correctly. For every spin flip attempt the measured frequency shift is compared to a certain threshold α_t. Each α_i, which is larger than α_t, is assigned to a spin transition. Depending on the magnitude of the background frequency instability Ξ_{back} and on the threshold α_t we can calculate the probability to misinterpret a spin flip attempt.
The model presented in section 3.5.2 assumed an overlap of three distributions corresponding to spin state changes from 'up' to 'down', 'down' to 'up' and a steady spin state. These distributions should be separated by the size of the frequency jump due to a spin flip $\Delta\nu_{\mathrm{z,SF}} = 171\,\mathrm{mHz}$ and broadened by the size of the background frequency instability Ξ_{back}. Fig. 8.19 shows a detailed analysis of the dataset of Fig. 8.18a). The histogram shown in Fig. 8.19a) gives the frequency instability $\Xi_{\mathrm{back}} = 55.0(0.6)\,\mathrm{mHz}$ of the axial frequency measurements without any spin-flip drive. The histogram shown in Fig. 8.19b) corresponds to the distribution of axial frequency differences for spin flip attempts, which shows the expected three peaks. We can further clarify the broadening of Fig. 8.19b) compared to Fig. 8.19a) by subtraction of the normalized distributions. The resulting distribution shown in Fig. 8.19c) should only contain successful spin flip attempts. A Gaussian fit gives the mean value of the left distribution of $-177(16)\,\mathrm{mHz}$ and $164(13)\,\mathrm{mHz}$ for the right distribution, which is in excellent agreement with the calculated change in the axial frequency caused by a spin flip. Moreover, the width of both distributions of $106(32)\,\mathrm{mHz}$ and $109(27)\,\mathrm{mHz}$ respectively is also in agreement with the measured background fluctuation Ξ_{back}. Thus, a spin flip drive does not cause additional frequency fluctuations due to a possible increase of the rate of cyclotron quantum jumps.
This is a very important result, since it shows the feasibility of the threshold-method to obtain a Larmor resonance curve as described in section 3.5.2.

8.7 Larmor resonances

In order to obtain a Larmor resonance curve, the spin flip probability as a function of the frequency of the external driving field is measured. To this end, the measurement procedure presented in the previous section is slightly modified and extended.
The basic cycle i consists of a series of axial frequency measurements ν_z separated by an excitation drive whose frequency ν_{rf} is varied in discrete steps:

- Axial frequency measurement $\nu_{z,0}$

1. No excitation drive
   - Axial frequency measurement $\nu_{z,1}$
2. Off-resonant drive $\nu_{\mathrm{rf}} = \nu_{\mathrm{ref}}$
   - Axial frequency measurement $\nu_{z,2}$

3a. Resonant drive $\nu_{\mathrm{rf}} = \nu_{\mathrm{exc,a}}$

- Axial frequency measurement $\nu_{z,3}$

3b. Resonant drive $\nu_{\mathrm{rf}} = \nu_{\mathrm{exc,b}}$

restart the cycle

For each cycle, the axial frequency differences $\alpha_{\mathrm{back}} = \nu_{z,1} - \nu_{z,0}$, $\alpha_{\mathrm{ref}} = \nu_{z,2} - \nu_{z,1}$, $\alpha_{\mathrm{exc,\,a}} = \nu_{z,3} - \nu_{z,2}$, $\alpha_{\mathrm{exc,\,b}} = \nu'_{z,0} - \nu_{z,3}$ are calculated, where $\nu'_{z,0}$ is the axial frequency of the following cycle. This yields the distributions of the axial frequency differences α^i for the different driving frequencies with the corresponding standard deviations Ξ_{back}, Ξ_{ref}, $\Xi_{\mathrm{exc,a}}$, $\Xi_{\mathrm{exc,b}}$. The cycle is repeated until the standard deviations Ξ converge to constant values. By comparison of Ξ_{back} and Ξ_{ref}, the effect of the driving field on the modified cyclotron motion can be tested. For equal fluctuations Ξ_{back} and Ξ_{ref}, it can be concluded, that the modified cyclotron mode is unaffected by the drive and that an increase of Ξ is due to spin transitions. The number of different resonant driving frequencies can of course be increased in order to obtain a better resolution of the resonance curve in frequency domain.

8.7.1 Larmor resonances measured with the previous setup

The spin flip probability of each driving frequency can be obtained by comparison of the standard deviations Ξ as discussed in section 3.5.1 (see Eq. (3.26)) or by analysis of each α as discussed in section 3.5.2. The power of the first method has already been demonstrated for comparably high background fluctuations $\Xi_{\mathrm{back}} \approx \Delta\nu_{z,\mathrm{SF}}$ for the previous setup [52, 47]. In Fig. 8.20 resonance curves obtained with the statistical analysis are shown. Each data point in Fig. 8.20a) was measured by repeating the above described cycle for about 500 times, which took overall about one week [52]. The solid line gives the best fit of Eq. (3.13) to the data. The parameters of the magnetic bottle strength $B_2 = 300\,\mathrm{mT/mm^{-2}}$, the irradiation time $t_0 = 10\,\mathrm{s}$ and the axial temperature $T_z = 9.5\,\mathrm{K}$ are fixed. Free fit parameters are the amplitude of the magnetic driving field b_{rf} and the Larmor frequency ν_L. A Larmor frequency of $\nu_L = 50.0351(52)\,\mathrm{MHz}$ is obtained from the fit, which corresponds to a relative uncertainty of $1.0 \cdot 10^{-4}$.
As discussed in section 3.2, the lineshape of the resonance curve is given by the thermal distribution of the axial mode in the magnetic bottle. Thus, the precision of the Larmor frequency determination can be increased by reduction of the axial temperature. The resonance curve shown in Fig. 8.20b) was obtained for a lower axial temperature of $T_z = 2.2(0.2)\,\mathrm{K}$ [47]. For each spin flip attempt, the axial temperature is reduced by application of strong negative feedback. The axial frequency measurement is performed without feedback applied. The excitation frequency was varied in 15 discrete steps with the highest resolution near the sharp edge of the resonance curve to obtain a precise information of the Larmor frequency. The solid line again is a fit of Eq. (3.13) to the data points which yields a Larmor frequency of $\nu_L = 50.064971(91)\,\mathrm{MHz}$.

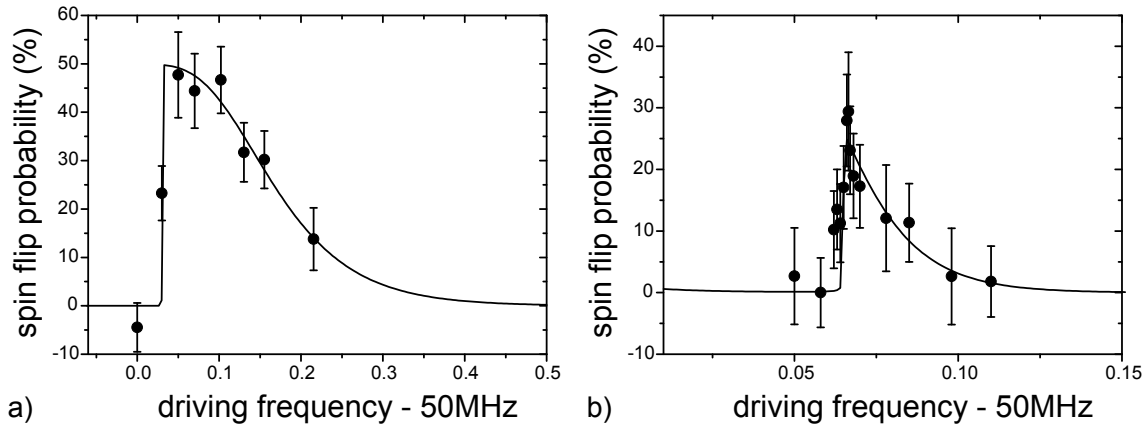

Figure 8.20: Larmor resonance curves measured with the former setup. The solid line is a fit of the resonance line shape given in Eq. (3.13) to the data. In a) the Larmor frequency was determined to $\nu_L = 50.0351(52)\,\mathrm{MHz}$ for an axial temperature of $T_z = 9.5\,\mathrm{K}$ [45]. For the measurement shown in b) negative feedback was applied to the axial detection system resulting in an axial temperature of $T_z = 2.2(0.2)\,\mathrm{K}$. The Larmor frequency was determined to $\nu_L = 50.064971(91)\,\mathrm{MHz}$ [46]. The second measurement was conducted for a different electrostatic potential, which results in a shift of the proton in axial direction and thus a different magnetic field strength. Accordingly, the measured Larmor frequency is different. For details see text.

8.7.2 Larmor resonance measured with the new setup

With the new detection system we are now able to reach axial temperatures down to $T_z = 1.06(0.22)\,\mathrm{K}$ as presented in section 8.4. Thus, a sharper resonance curve than that shown in Fig. 8.20b) to obtain a Larmor frequency with a relative uncertainty better than 10^{-6} should be possible. However, this would require precise control of the temperature of the magnetron mode as discussed in section 3.3. The obtain a relative uncertainty better than 10^{-7} for the Larmor frequency, the magnetron temperature has to be kept constant to a level of $T_- = 5\,\mathrm{mK}$.

The more relevant question is, whether the improved stability of the axial frequency is good enough to allow for the determination of the g-factor in the precision trap. As a demonstration, we measured a Larmor resonance in the analysis trap. The above described cycle was repeated for three different excitation frequencies $\nu_{\mathrm{exc,a}} < \nu_{\mathrm{exc,b}} < \nu_{\mathrm{exc,c}}$ for 100 times. The (familiar) statistical analysis of the data is shown in Fig. 8.21a). Due to the low background fluctuations of $\Xi_{\mathrm{back}} = 56\,\mathrm{mHz}$ a clear signature of the resonance is obtained in less than 15 hours.

For the analysis shown in Fig. 8.21b) each axial frequency difference α is compared to a certain threshold $\alpha_t = 80\,\mathrm{Hz}$ as described in section 3.5.2. Each spin flip attempt is individually examined as in the case of the double-trap technique. Due to the finite width of the background fluctuations, successful spin flips are obtained for vanishing spin flip probability. Thus, the baseline of the resonance is raised to $P_{\mathrm{SF}}(\nu_{\mathrm{exc,a}}) = 14.4(1.1)\,\%$.

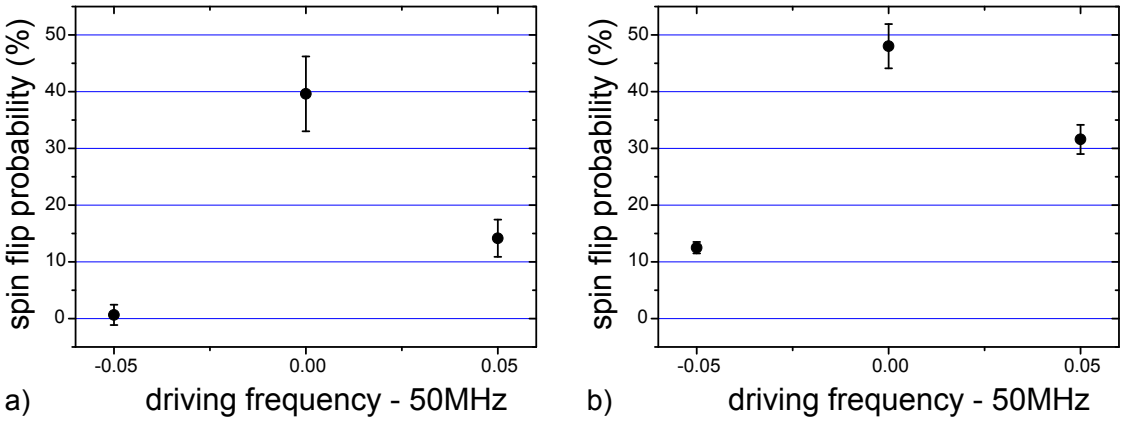

Figure 8.21: Larmor resonance curves measured with the new setup. The aim of this measurement was not to resolve the line shape of the resonance curve as in Fig. 8.20 but to test the direct detection scheme. In a) the data was evaluated with the statistical method. In b) each frequency jump α was compared to the threshold $\alpha_t = 80\,\mathrm{mHz}$. All driving attempts with $\alpha > \alpha_t$ were assigned to be successful. The data shows that the spin flip probability can be analysed with the direct detection scheme. For details see text.

This is in perfect agreement with the expected value of $P_{\mathrm{SF}}(\nu_{\mathrm{exc,a}}) = 14.5\,\%$, which is calculated from the magnitude of the background fluctuations (see Eq. (3.30)).
The comparison of Fig. 8.21a) and Fig. 8.21b) shows, that the threshold-method can be utilized to resolve the Larmor resonance and thus employ the double-trap technique to determine the g-factor in the precision trap.

8.8 Towards a sub-ppb measurement of the g-factor

In this section, the feasibility of the double-trap technique to determine the g-factor with a precision of about 10^{-9} is discussed. The analysis of the Larmor resonance shown in Fig. 8.21b) proofed the applicability of the threshold-method in the analysis trap. However, transfer to the precision trap is complicated by two aspects:

1. **Spin state preparation:** In order to determine the success of a spin flip attempt in the precision trap correctly, the spin state in the analysis trap has to be detected correct twice. First, when the proton leaves the analysis trap and second when it returns to the analysis trap. Thus, the baseline of the Larmor resonance in the precision trap is additionally raised, lowering the SNR of the resonance curve.
   This problem can at least be reduced by the following spin state preparation procedure performed in the analysis trap:
   Spin flip attempts are conducted until a frequency difference $|\alpha_p| > \epsilon\Delta\nu_{z,\mathrm{SF}}$, with $\epsilon > 1$, is detected. From the sign of α_p, the final spin state can be determined. The probability that the first frequency jump $|\alpha_p|$ is not caused by a spin flip (and thus

the initial spin state is not detected correctly with a probability of 50 %) is given by:

$$P_{\text{false prepared}} = \sum_{N=0}^{\infty} (P_{\text{SF}} P_{\text{Flip}})^N (1 - P_{\text{SF}}) P_{\text{Steady}} \quad , \tag{8.7}$$

with

$$P_{\text{Flip}} = 1 - \int_{-\alpha_p}^{\alpha_p} g(\Xi_{\text{back}}, \Delta\nu_{z,\text{SF}}) \text{d}\alpha \tag{8.8}$$

$$P_{\text{Steady}} = 1 - \int_{-\alpha_p}^{\alpha_p} g(\Xi_{\text{back}}, 0) \text{d}\alpha \quad , \tag{8.9}$$

where P_{Flip} gives the probability, that for a spin transition, a frequency difference larger than α_p is measured. Analogous, P_{Steady} gives the probability, that for a steady spin state, a frequency difference larger than α_p is measured.
For axial background fluctuations of $\Xi_{back} = 80\,mHz$, $P_{SF} = 50\,\%$ *and* $\alpha_p = 250\,mHz$, $P_{Flip} = 16\,\%$ *and* $P_{Steady} = 0.17\,\%$ *are obtained which yields* $P_{false\ prepared} = 0.2\,\%$.
Thus, the initial spin state can be prepared with a very low uncertainty in the analysis trap.

2. **Cyclotron temperature preparation:** The probability to misinterpret a spin flip attempt in the analysis trap is increased for larger axial frequency fluctuations. As discussed in section 8.5 the frequency stability decreases for higher temperatures of the cyclotron mode. Thus, spin state analysis in the AT gives reliable results for small cyclotron radii, only. The cyclotron temperature of the proton is defined by the detection system in the PT. By application of negative feedback temperatures of $T_+ = 3.15(0.11)\,\text{K}$ were reached. However, for each spin flip attempt in the precision trap, the modified cyclotron frequency is measured which implies a heating of the modified cyclotron mode. Thus, each cycle requires time consuming cooling of the modified cyclotron mode before transport to the AT. Moreover, the cyclotron radius of the proton leaving the precision trap can only be detected in the analysis trap. Thus, preparation of suitable cyclotron radii is the bottleneck of the double-trap measurement of the g-factor.
This, however, reveals the importance of the decreased cyclotron transition rate as a function of the cyclotron temperature, which was achieved with the new setup. It significantly increases the acceptance range of cyclotron temperatures for successful spin state analysis.

Summarizing, the increased axial frequency stability eliminates the last obstacle for a g-factor measurement in the precision trap. The rate of spurious quantum jumps in the cyclotron mode was significantly reduced. This allows to prepare the spin state in the analysis trap with high reliability and reduces the time to achieve a sufficiently low cyclotron temperature.
A Larmor resonance in the precision trap is feasible - opening the door towards a ppb determination of the magnetic moment of a single proton an thus in a similar way also for a single antiproton.

Chapter 9

Conclusion and outlook

In this thesis, important progress towards a high-precision determination of the proton g-factor was achieved.
Several improvements concerning the precise determination of the free cyclotron frequency in the precision trap were realized. The implementation of a new liquid cryostat proved to solve the problem of oscillations of the magnetic field strength, which were induced by the former utilized puls-tube cooler. This allows now for routinely measurements of the free cyclotron frequency at the ppb-level. Moreover, the first detection of the modified cyclotron frequency of a single particle in thermal equilibrium with the detection system was demonstrated. Due to careful optimization of the cyclotron feedback loop we were able to reach quality factors of the order of 10^6, which allowed us to resolve the single proton noise-dip in resonance with the cyclotron detection system with a relative statistical uncertainty of less than one ppb in 100 s averaging time. Systematic shifts for the corresponding temperature of 1800 K are about one ppb. The axial detection system can be utilized to determine ν_z simultaneously, since the high-precision measurement of the modified cyclotron frequency is not accomplished by a sideband-coupling to the axial mode. Thus, the measurement time for the free cyclotron frequency is reduced by about a factor of two, compared to the conventional sideband coupling technique.
Moreover, great progress was achieved for the spin state detection in the magnetic bottle field of the analysis trap. The key issue over the past years was the realization of a sufficiently stable axial frequency to enable the observation of spin flips as axial frequency jumps. In this thesis, detailed investigations of the origin of axial frequency fluctuations in the analysis trap were performed. The analysis of the axial frequency stability with the transient recorder allowed us to identify energy fluctuations in the modified cyclotron mode as the reason for the frequency fluctuations. Moreover, these investigations revealed a scaling of the frequency fluctuations with the absolute radial energy. The preparation of a proton with radial energies of a few μeV allowed us to perform a statistical detection of spin flips in the analysis trap to determine the g-factor of the proton with a relative precision of 9 ppm [46]. Further reduction of energy fluctuations in the radial modes was realized by a complete revision of the experimental setup, which resulted in the detection

of individual spin transitions of a single proton for the first time. It is now possible to determine the spin state of a proton in our analysis trap with high fidelity.
Summarizing, the precise determination of the free cyclotron frequency as well as the detection of the spin state of a single proton were realized in this thesis. These important steps allow for the realization of the double-trap technique to measure the g-factor of a single proton with a relative precision of about one ppb.

9.1 Future improvements

This section gives an overview of ideas to improve the experimental setup, which are related to two different aspects: The first section describes possible improvements concerning the high-precision measurement of the eigenfrequencies in the precision trap. The second part introduces possible developments for an improved spin state fidelity in the analysis trap.

9.1.1 High precision frequency measurement in the precision trap

Temperature stabilization We observed a strong correlation of the modified cyclotron frequency with the temperature of the apparatus. Thus, the realization of a temperature stabilization is the first task, in order to eliminate the corresponding drifts of the modified cyclotron frequency. This system has recently been implemented by Andreas Mooser in the course of his Ph.D.-thesis and shows promising results.

Self shielding coil Further reduction of magnetic field fluctuations can be achieved by the implementation of a self shielding coil [80]. This concept has been successfully applied in several high-precision Penning trap experiments [30, 81, 82, 83]. It relies on the principle of magnetic flux conservation in a closed superconducting loop. The closed loop can for example be realized by a superconducting solenoid. For a suited geometry of the coil, flux conservation corresponds to magnetic field conservation at the center of coil. Thus, external magnetic field fluctuations are compensated. For our experiment the self-shielding coil could be wound around the trap chamber, centered at the position of the precision trap in axial direction.

Sharper resonance lines The ferromagnetic ring electrode of the analysis trap leads to a considerable magnetic inhomogeneity in the precision trap of $B_2 = 4.7\,\mathrm{T/m^{-2}}$. This results in a broadening of the resonance curves of ν_c and ν_L of the order of a few ppb due to the Boltzmann distributed energy in the axial mode. This is no obstacle for the upcoming determination of the g-factor at the ppb-level. However, for an improved future determination of the g-factor with a relative precision of the order of 100 ppt, this systematic limitation has to be considered. The first possibility to reduce B_2 at the position of the precision trap is a larger distance between analysis trap and precision trap. This can be realized by an extension of the transport section by additional electrodes. For the current dimensions of the trap chamber, a corresponding increase of the distance by a

factor of about 1.7 can be realized (see Fig. 6.5). This would reduce the magnetic bottle in the precision trap, originating from the ferromagnetic ring of the analysis trap, by a factor of ten.
Further separation of both traps does not necessarily imply a reduction of the magnetic inhomogeneity in the precision trap due to possible inhomogeneities caused by other materials in the bore of the magnet.

Another possibility to obtain sharper resonance lines, is the reduction of the axial temperature during the measurement of ν_L and ν_c. The feasibility of a temperature reduction by about a factor of ten was demonstrated for the axial detection system attached to the analysis trap. However, the corresponding decrease of the linewidth and the SNR of the axial dip has to be considered, which will reduce the measurement accuracy of the axial frequency with increasing feedback strength. This obstacle can be overcome for a determination of ν_+, which is independent of the axial detection system. A possible realization is the measurement of ν_+ with the dip-technique, which would allow for the application of strong negative feedback to reduce the axial temperature during the measurement of ν_+.

9.1.2 Advanced spin state analysis

Possible improvements to increase the spin flip fidelity, which would reduce the required measurement time and increase the resolution of a Larmor resonance, are discussed in the following.

Increasing the spin flip fidelity The probability to detect the correct spin state in the analysis trap can be increased by the reduction of the resonance frequency ν_{LC} of the axial detection system. The frequency uncertainty due to noise averaging of the FFT-spectrum Ξ_{FFT} is independent on the absolute axial frequency. But the frequency jump due to a spin flip is inverse proportional to the axial frequency. Thus, the relative contribution of the measurement uncertainty Ξ_{FFT} is reduced for a smaller absolute axial frequency. However, a smaller resonance frequency implies a decreased potential depth to tune the proton into resonance with the detection system. The asymmetry optimization procedure demonstrated that patch potentials in the order of the trapping potential can be detected and compensated. A potential depth of 0.5 V is feasible. This would reduce the relative contribution of Ξ_{FFT} to the axial frequency fluctuations by a factor 1.5 , which would increase the spin flip fidelity. However, the $1/f$-noise of the amplifier has to be considered. A possible degradation of the measurement accuracy due to an increased noise of the amplifier has to be investigated.

Improved cyclotron feedback loop The axial frequency fluctuations in the analysis trap scale proportional to the energy of the modified cyclotron mode, which corresponds to a decreasing spin flip fidelity. Thus, only a small part of the Boltzmann-distributed energies in the modified cylotron mode after thermalization in the precision trap is suited for a successful spin state analysis. This means, that several transport and thermalization cy-

cles are required until an appropriate cyclotron energy is obtained. An improved feedback loop to reduce the effective temperature of the cyclotron detection system would decrease the time which is required to obtain a sufficient low energy of the modified cyclotron mode. This would correspond to a reduction of the measurement time for the Larmor resonance in the precision trap. The lowest attainable temperature is limited by additional noise introduced by the components of the feedback loop. Thus, a lower temperature could be realized by a cryogenic amplifier with improved noise characteristics, since the total noise of the amplifier system is mainly defined by the first cryogenic stage. Cryogenic amplifiers with low equivalent input-noise were developed for the axial detection systems [57, 58]. The feasibility to utilize these amplifiers for the cyclotron-detection system at higher frequencies has to be investigated.

The realization of the proposed improvements would require an alteration of the experimental setup. However, already now spin state analysis of a single proton with high fidelity is possible and the broadening of the resonances in the precision trap is only of the order of a few ppb. Thus, the very next step is the measurement of the magnetic moment with the double-trap technqiue in order to determine the g-factor with a relative precision at the ppb-level.
The presented techniques and developments are directly applicable for the corresponding experiment with the antiproton. The BASE-collaboration has very recently started to set up an apparatus dedicated to the measurement of the g-factor of the antiproton [36]. Thus, the realization of a stringent test of CPT-symmetry is under way. With these fascinating prospectives this thesis is closed.

Appendix A

Cyclotron noise-dip for a cloud of protons

This appendix discusses the application of the cyclotron-dip technique for Penning trap experiments on highly charged ions. Due to the higher charge states, lower quality factors than in case of a single proton are sufficient to resolve the cyclotron dip since the width of the dip scales proportional q^2/m (see Eq. 4.23), where q is the charge and m is the mass of the ion. On the one hand, this would greatly relax the technical challenges concerning the stability of the feedback gain and on the other hand it would allow for a measurement of ν_+ at temperatures below those which are obtained for the double-dip technique. This possibility was demonstrated for a cloud of 25 protons, yielding a dip-width equivalent to that for a single hydrogen-like iron ion $^{52}Fe^{25+}$. Here, only a quality factor of $Q \approx 5000$ was required to resolve the cyclotron dip in 90 s averaging time as shown in Fig. A.1a). The corresponding cyclotron temperature of $T_+ \approx 42\,\mathrm{K}$ is a factor of 4 less than for the sideband coupling technique. The determination of ν_+ with the cyclotron dip allows for a simultaneous measurement of the axial frequency as shown in Fig. A.1b), which is the main experimental advantage of the cyclotron dip since it allows for a factor of 2 faster determination of the free cyclotron frequency. From a fit to the corresponding spectrum the motional frequencies were determined, which are summarized in Tab. A.1. The mag-

Measured frequency	Relative uncertainty	Contribution to relative uncertainty in ν_c
$\nu_+ = 28\,972\,580.313(10)$	$3.5 \cdot 10^{-10}$	$3.4 \cdot 10^{-10}$
$\nu_z = 785\,090.13(17)$	$2.2 \cdot 10^{-7}$	$1.2 \cdot 10^{-10}$
$\nu_- = 10640.2(0.4)$	$3.8 \cdot 10^{-5}$	$5.1 \cdot 10^{-12}$
$\nu_c = 28\,983\,217.380(11)$	$3.6 \cdot 10^{-12}$	

Table A.1: The three eigenfrequencies of a cloud of 25 protons. The relative uncertainty of each mode is given by the second column. The last column lists the contribution to the relative uncertainty of the free cyclotron frequency.

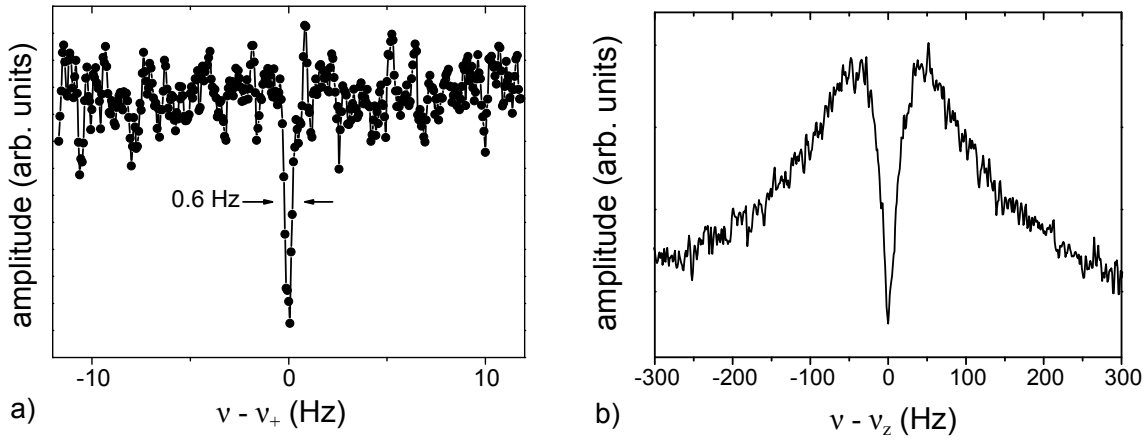

Figure A.1: a) Cyclotron noise dip of $N \approx 25$ protons. The quality factor was only slightly increased to $Q \approx 5000$ - thus keeping the temperature of the modified cyclotron mode lower than for the case of the sideband coupling technique. The modified cyclotron frequency was determined by a fit to the data to $\nu_+ = 28\,972\,580.313(10)\,\mathrm{Hz}$. b) A simultaneous measurement of the axial frequency with a corresponding detection system yields an axial frequency of $\nu_z = 785\,090.13(17)\,\mathrm{Hz}$.

netron frequency was determined in a separate measurement. With this method, the free cyclotron frequency was determined with a relative uncertainty of $\Delta\nu_c/\nu_c = 3.6 \cdot 10^{-10}$. Further reduction of the losses in the LC-circuit is feasible which would provide quality factors of several thousands without feedback [84]. Thus, the cyclotron dip allows for a continuous monitoring of the free cyclotron frequency at very low temperatures. This is an important application for future mass experiments. In contemporary mass measurements, two ions are alternately confined in the same trap. The time which is required to exchange the ions is a dominant limitation of these experiments due to the limited temporal stability of the magnetic field [81]. Simultaneous measurements of two ions in one trap have already been demonstrated but are rather sophisticated [85, 86]. Tracing the magnetic field strength while exchanging the ions as proposed in [87] requires an easy and direct way to access ν_c, which could be realized with the cyclotron noise-dip as presented.

Bibliography

[1] W. N. Cottingham and D. A. Greenwood. *The Weinberg-Salam electroweak theory for leptons.* Cambridge University Press (2007).

[2] S. Glashow. *Towards a unified theory: Threads in a tapestry.* Reviews of Modern Physics **52**, 539–543 (1980).

[3] R. S. Van Dyck Jr, P. B. Schwinberg, and H. G. Dehmelt. *New high-precision comparison of electron and positron g factors.* Phys. Rev. Lett. **59**, 26–29 (1987).

[4] R. S. Van Dyck Jr, P. B. Schwinberg, and H. G. Dehmelt. *Electron magnetic moment from geonium spectra: Early experiments and background concepts.* Phys. Rev. D **34**, 722 (1986).

[5] K. Blaum, Y. N. Novikov, and G. Werth. *Penning traps as a versatile tool for precise experiments in fundamental physics.* Contemporary Physics **51**, 149–175 (2010).

[6] D. Hanneke, S. Fogwell, and G. Gabrielse. *New Measurement of the Electron Magnetic Moment and the Fine Structure Constant.* Phys. Rev. Lett. **100**, 120801 (2008).

[7] D. Hanneke, S. Fogwell, and G. Gabrielse. *Cavity control of a single-electron quantum cyclotron: Measuring the electron magnetic moment.* Phys. Rev. A **83**, 052122 (2011).

[8] T. Aoyama, M. Hayakawa, T. Kinoshita, and M. Nio. *Tenth-Order QED Contribution to the Electron $g-2$ and an Improved Value of the Fine Structure Constant.* Phys. Rev. Lett. **109**, 111807 (2012).

[9] H. Häffner *et al. High-accuracy measurement of the magnetic moment anomaly of the electron bound in hydrogenlike carbon.* Phys. Rev. Lett. **85**, 5308–5311 (2000).

[10] J. Verdú *et al. Electronic g factor of hydrogenlike oxygen* $^{16}O^{7+}$. Phys. Rev. Lett. **92**, 93002 (2004).

[11] S. Sturm *et al. g Factor of Hydrogenlike* $^{28}Si^{13+}$. Phys. Rev. Lett. **107**, 23002 (2011).

[12] B. Schabinger *et al. Experimental g factor of hydrogenlike silicon-28.* The European Physical Journal D-Atomic, Molecular, Optical and Plasma Physics **66**, 1–10 (2012).

[13] R. Bluhm, V. Kosteleckỳ, and N. Russell. *CPT and Lorentz tests in Penning traps.* Phys. Rev. D **57**, 3932–3943 (1998).

[14] O. Greenberg. *CPT violation implies violation of Lorentz invariance.* Phys. Rev. Lett. **89**, 231602 (2002).

[15] O. Bertolami, D. Colladay, V. Kosteleckỳ, and R. Potting. *CPT violation and baryogenesis.* Phys. Lett. B **395**, 178–183 (1997).

[16] R. Frisch and O. Stern. *Über die magnetische Ablenkung von Wasserstoffmolekülen und das magnetische Moment des Protons. I.* Zeitschrift für Physik A Hadrons and Nuclei **85**, 4–16 (1933).

[17] I. Estermann and O. Stern. *Über die magnetische Ablenkung von Wasserstoffmolekülen und das magnetische Moment des Protons. II.* Zeitschrift für Physik A Hadrons and Nuclei **85**, 17–24 (1933).

[18] P. Dirac. *The quantum theory of the electron.* Proceedings of the Royal Society of London. Series A **117**, 610–624 (1928).

[19] I. I. Rabi, J. M. B. Kellogg, and J. R. Zacharias. *The Magnetic Moment of the Proton.* Phys. Rev. **46**, 157–163 (1934).

[20] F. Bloch, W. Hansen, and M. Packard. *Nuclear induction.* Phys. Rev. **70**, 460–474 (1946).

[21] H. Sommer, H. A. Thomas, and J. A. Hipple. *The Measurement of $\frac{e}{M}$ by Cyclotron Resonance.* Phys. Rev. **82**, 697–702 (1951).

[22] D. J. Collington, A. N. Dellis, J. H. Sanders, and K. C. Turberfield. *Magnetic Moment of the Proton.* Phys. Rev. **99**, 1622–1623 (1955).

[23] P. Winkler, D. Kleppner, T. Myint, and F. Walther. *Magnetic Moment of the Proton in Bohr Magnetons.* Phys. Rev. A **5**, 83–114 (1972).

[24] S. Karshenboim and V. Ivanov. *The* g *factor of the proton.* Phys. Lett. B **566**, 27–34 (2003).

[25] T. Beier *et al. New determination of the electron's mass.* Phys. Rev. Lett. **88**, 11603 (2001).

[26] C. C. Rodegheri *et al. Developments for the direct determination of the g-factor of a single proton in a Penning trap.* Hyp. Int. **194**, 93–98 (2009).

[27] S. Ulmer *et al. Direct Measurement of the Free Cyclotron Frequency of a Single Particle in a Penning Trap.* Phys. Rev. Lett. **107**, 103002 (2011).

[28] A. Mooser *et al. Towards a direct measurement of the g-factor of a single isolated proton.* Can. Journ. Phys. **89**, 165–168 (2011).

[29] G. Gabrielse *et al. First Capture of Antiprotons in a Penning Trap: A Kiloelectronvolt Source.* Phys. Rev. Lett. **57**, 2504–2507 (1986).

[30] G. Gabrielse *et al. Thousandfold improvement in the measured antiproton mass.* Phys. Rev. Lett. **65**, 1317–1320 (1990).

[31] J. DiSciacca and G. Gabrielse. *Direct measurement of the proton magnetic moment.* Phys. Rev. Lett. **108**, 153001 (2012).

[32] N. Guise, J. DiSciacca, and G. Gabrielse. *Self-Excitation and Feedback Cooling of an Isolated Proton.* Phys. Rev. Lett. **104**, 143001 (2010).

[33] H. Dehmelt. *Continuous Stern-Gerlach effect: Principle and idealized apparatus.* Proceedings of the National Academy of Sciences **83**, 2291–2294 (1986).

[34] A. Kreissl *et al. Remeasurement of the magnetic moment of the antiproton.* Zeitschrift für Physik C Particles and Fields **37**, 557–561 (1988).

[35] T. Pask *et al. Antiproton magnetic moment determined from the HFS of* $\bar{p}He^+$. Phys. Lett. B **678**, 55–59 (2009).

[36] S. Ulmer *et al. Scientific committee paper: Direct High-Precision Measurement of the g-Factor of a Single Antiproton Stored in a Cryogenic Penning Trap.* Tech. Rep. CERN-SPSC-2012-019. SPSC-I-241, CERN, Geneva (2012).

[37] J. R. Pierce. *Theory and design of electron beams.* van Nostrand Co., New York (1949).

[38] H. Dehmelt. *Radiofrequency Spectroscopy of Stored Ions I: Storage.* Advances in Atomic and Molecular Physics **3**, 53–72 (1967).

[39] L. S. Brown and G. Gabrielse. *Geonium theory: Physics of a single electron or ion in a Penning trap.* Rev. Mod. Phys. **58**, 233–311 (1986).

[40] K. Blaum. *High-accuracy mass spectrometry with stored ions.* Phys. Rep. **425**(1), 1–78 (2006).

[41] L. S. Brown and G. Gabrielse. *Precision spectroscopy of a charged particle in an imperfect Penning trap.* Phys. Rev. A **25**, 2423 (1982).

[42] M. Kretzschmar. *Single particle motion in a Penning trap: description in the classical canonical formalism.* Physica Scripta **46**, 544 (1992).

[43] L. D. Landau and E. M. Lifshitz. *Mechanics.* Pergamon Press, Oxford (1965).

[44] G. Gabrielse, L. Haarsma, and S. Rolston. *Open-endcap Penning traps for high precision experiments.* International Journal of Mass Spectrometry and Ion Processes **88**, 319–332 (1989).

[45] S. Ulmer. *First observation of spin flips with a single proton stored in a cryogenic Penning trap.* Ph.D. thesis, Ruprecht Karls Universität, Heidelberg (2011).

[46] C. C. Rodegheri. *to be submitted.* Ph.D. thesis, Johannes Gutenberg Universität, Mainz (2012).

[47] C. C. Rodegheri *et al. An experiment for the direct determination of the g-factor of a single proton in a Penning trap.* New Journ. Phys. **14**, 063011 (2012).

[48] L. S. Brown. *Geonium lineshape.* Annals of Physics **159**, 62–98 (1985).

[49] I. Rabi, S. Millman, P. Kusch, and J. Zacharias. *The molecular beam resonance method for measuring nuclear magnetic moments.* Phys. Rev **53**, 318 (1938).

[50] H. Häffner *et al. Double Penning trap technique for precise g factor determinations in highly charged ions.* The European Physical Journal D-Atomic, Molecular, Optical and Plasma Physics **22**, 163–182 (2003).

[51] N. Hermanspahn *et al. Observation of the continuous Stern-Gerlach effect on an electron bound in an atomic ion.* Phys. Rev. Lett. **84**, 427–430 (2000).

[52] S. Ulmer *et al. Observation of Spin Flips with a Single Trapped Proton.* Phys. Rev. Lett. **106**, 253001 (2011).

[53] D. Wineland and H. Dehmelt. *Principles of the stored ion calorimeter.* Journal of Applied Physics **46**, 919 (1975).

[54] H. Dehmelt and F. Walls. *" Bolometric" Technique for the rf Spectroscopy of Stored Ions.* Phys. Rev. Lett. **21**, 127–131 (1968).

[55] S. Ulmer *et al. The quality factor of a superconducting rf resonator in a magnetic field.* Rev. Sci. Instrum. **80**, 123302 (2009).

[56] H. Kracke. *Entwicklung der kryogenen Nachweis-Elektronik zur Bestimmung der axialen Frequenz des Protons in einer Penning-Falle.* Diploma thesis, Johannes-Gutenberg Universität, Mainz (2007).

[57] A. Mooser. *to be submitted.* Ph.D. thesis, Johannes-Gutenberg Universität, Mainz (2013).

[58] S. Sturm. *The g-factor of the electron bound in $^{28}Si^{13+}$: The most stringent test of bound-state quantum electrodynamics.* Ph.D. thesis, Johannes-Gutenberg Universität, Mainz (2012).

[59] J. Johnson. *Thermal agitation of electricity in conductors.* Phys. Rev. **32**, 97–109 (1928).

[60] X. Feng *et al. Tank circuit model applied to particles in a Penning trap.* Journal of Applied Physics **79**, 8 (1996).

[61] E. Cornell, R. Weisskoff, K. Boyce, and D. Pritchard. *Mode coupling in a Penning trap: π pulses and a classical avoided crossing.* Phys. Rev. A **41**, 312–315 (1990).

[62] C. Kittel. *Elementary statistical physics.* Wiley, New York (1958).

[63] H. Dehmelt, W. Nagourney, and J. Sandberg. *Self-excited mono-ion oscillator.* Proceedings of the National Academy of Sciences **83**, 5761–5763 (1986).

[64] B. R. D'Urso, B. Odom, and G. Gabrielse. *Feedback cooling of a one-electron oscillator.* Phys. Rev. Lett. **90**, 43001 (2003).

[65] B. R. D'Urso. *Cooling and self-excitation of a one-electron oscillator.* Ph.D. thesis, Harvard University (2003).

[66] S. Kreim. *Direct observation of a single proton in a Penning trap.* Ph.D. thesis, Johannes-Gutenberg Universität, Mainz (2009).

[67] S. Ulmer. *Entwicklung des experimentellen Aufbaus zur Messung des g-Faktors des Protons in einer Penning-Falle.* Diploma thesis, Johannes-Gutenberg Universität, Mainz (2006).

[68] A. Mooser. *Untersuchung des Magnetfelds zur Spinflipanregung eines Protons in einer Penningfalle.* Diploma thesis, Johannes-Gutenberg Universität, Mainz (2009).

[69] U. Tietze, C. Schenk, and E. Gramm. *Halbleiter-Schaltungstechnik.* Springer, Berlin (2002).

[70] Fluke. *8508A Reference Multimeter Extended Specifications.* datasheet (2002).

[71] S. Rainville. *A two-ion balance for high precision mass spectrometry.* Ph.D. thesis, Massachusetts Institute of Technology (2003).

[72] C. Mrozik. *Weiterentwicklung und Verbesserung des experimentellen Aufbaus zur Messung des magnetischen Moments des Protons.* Diploma thesis, Johannes-Gutenberg Universität, Mainz (2009).

[73] S. Guan. *General phase modulation method for stored waveform inverse Fourier transform excitation for Fourier transform ion cyclotron resonance mass spectrometry.* The Journal of Chemical Physics **91**, 775 (1989).

[74] E. Cornell, K. Boyce, D. Fygenson, and D. Pritchard. *Two ions in a Penning trap: Implications for precision mass spectroscopy.* Phys. Rev. A **45**(5), 3049–3059 (1992).

[75] U. Fischer *et al. Tabellenbuch Metall*, vol. 41. Europa-Lehrmittel (2002).

[76] H. Kracke *et al. Single ion cyclotron frequency measurement at thermal equilibrium with the detection system.* to be submitted (2013).

[77] R. Schiffel and A. Koehler. *Werkbuch Hochfrequenz-Technik.* Franzis, Poing (2003).

[78] J. B. Camp, T. W. Darling, and R. E. Brown. *Macroscopic variations of surface potentials of conductors.* Journal of Applied Physics **69**, 7126–7129 (1991).

[79] J. Tan. *Cooperative behavior in cavity-cooled, parametrically-pumped electron oscillators.* Ph.D. thesis, Harvard University (1992).

[80] G. Gabrielse and J. Tan. *Self-shielding superconducting solenoid systems.* J. Appl. Phys **63** (1988).

[81] R. S. van Dyck, D. L. Farnham, S. L. Zafonte, and P. B. Schwinberg. *Ultrastable superconducting magnet system for a penning trap mass spectrometer.* Rev. Sci. Instrum. **70**, 1665–1671 (1999).

[82] G. Bollen and S. Schwarz. *Penning trap mass measurements on rare isotopes - status and new developments.* Journal of Physics B: Atomic, Molecular and Optical Physics **36**, 941 (2003).

[83] A. Wagner. *to be submitted.* Ph.D. thesis, Ruprecht Karls Universität, Heidelberg (2013).

[84] C. Roux. *High-Resolution Mass Spectrometry: The Trap Design and Detection System of Pentatrap and New Q-Values for Neutrino Studies.* Ph.D. thesis, Ruprecht Karls Universität, Heidelberg (2012).

[85] S. Rainville, J. Thompson, and D. Pritchard. *An ion balance for ultra-high-precision atomic mass measurements.* Science **303**, 334–338 (2004).

[86] G. Gabrielse *et al. Precision Mass Spectroscopy of the Antiproton and Proton Using Simultaneously Trapped Particles.* Physical Review Letters **82**, 3198–3201 (1999).

[87] J. Repp *et al. PENTATRAP: a novel cryogenic multi-Penning-trap experiment for high-precision mass measurements on highly charged ions.* Applied Physics B: Lasers and Optics 1–14 (2012).